Journal of Materials Chemistry A

REVIEW

View Article Online
View Journal | View Issue

Check for updates

Cite this: J. Mater. Chem. A, 2025, 13, 30708

Recent advances in tin halide perovskite solar cells: a critical review

Boya Zhang,†[a] Zitian Zeng,†[a] He Dong,*[a] Weiyin Gao*[b] and Chenxin Ran *[acd]

Tin (Sn) halide-based perovskites are rising as competitive candidates for eco-friendly perovskite solar cells (PSCs) that have garnered immense attention. In particular, the power conversion efficiency (PCE) of the Sn-based perovskite solar cells (TPSCs) has exceeded 17%, ranking above all the other lead-free perovskite photovoltaics. Nevertheless, the problems of intrinsic instability and extremely fast crystallization of TPSCs place restrictions on both the device performance and stability, hampering their commercial applications. Fortunately, valid strategies have been developed and extensively studied over the past few years, and the fundamental problems of Sn-based perovskites have been effectively addressed, taking a big step forward in the field of TPSCs. In this review, initially, an overview is given on the unique properties of Sn-based perovskite materials, encompassing their crystallographic structures, optoelectronic characteristics, and chemical degradation pathways. Furthermore, the state-of-the-art strategies, including structural engineering, crystallization regulation and interface engineering, toward high-performance TPSCs are comprehensively reviewed. Finally, we present future challenges faced by Sn-based perovskites and provide crucial perspectives for further realizing efficient and stable TPSCs, thereby laying the critical foundation for future practical applications of Sn-based perovskites not only in PSCs but also in many other thin-film optoelectronic devices.

Received 5th June 2025
Accepted 30th July 2025

DOI: 10.1039/d5ta04568a

rsc.li/materials-a

Published on 01 August 2025. Downloaded on 1/24/2026 5:38:31 AM.

1. Introduction

With the growing demand for clean and renewable energy sources, photovoltaic technology has attracted considerable attention in recent years. Since their inception in 2009, PSCs have achieved remarkable advancements, boosting a remarkable certified PCE of 27% in 2025.[1] This outstanding accomplishment is attributed to the intriguing optoelectronic properties displayed by organic–inorganic hybrid perovskite materials, which include facile solution-processability, tunable optical band gap and exceptional absorption coefficient, which

[a]Frontiers Science Center for Flexible Electronics, Xi'an Institute of Flexible Electronics (IFE), Northwestern Polytechnical University, Xi'an 710072, P. R. China. E-mail: iamhdong@nwpu.edu.cn; iamcxran@nwpu.edu.cn

[b]College of New Energy, Xi'an Shiyou University, Xi'an 710065, China. E-mail: iamwygao@xsyu.edu.cn

[c]Research & Development Institute of Northwestern Polytechnical University in Shenzhen, Shenzhen 518063, China

[d]Chongqing Innovation Center, Northwestern Polytechnical University, Chongqing 401135, China

† Equally contributed.

Boya Zhang

Boya Zhang is currently a third-year undergraduate student in the Queen Mary University of London Engineering School at Northwestern Polytechnical University. His research interests focus on tin-based perovskite solar cells.

Zitian Zeng

Zitian Zeng is currently a third-year undergraduate student in the Queen Mary University of London Engineering School at Northwestern Polytechnical University. Her research interests focus on tin-based perovskite solar cells.

This journal is © The Royal Society of Chemistry 2025

Published on 01 August 2025. Downloaded on 1/24/2026 5:38:31 AM.

collectively position them as an ideal candidate for cost-effective solar energy conversion.[2–5] Organic–inorganic lead (Pb) halide perovskites represent the most extensively studied class of perovskite materials. Over the past decades, multi-faceted strategies such as dimensional engineering and interface optimization have enabled significant advancements in their efficiencies.[6,7] Notably, Pb-based perovskites have recently emerged as a pivotal platform for harvesting ambient light energy,[8,9] showcasing substantial promise as a dependable energy source for low-power electronic devices. However, the inclusion of the toxic Pb element shadows the application of PSCs due to environmental concerns.[10] Over the past decades, tremendous efforts have been made to investigate environmentally friendly metal elements as substitutes for Pb, including tin (Sn), germanium (Ge), copper (Cu), antimony (Sb), and bismuth (Bi).[10–14] Among these, Sn-based perovskites are regarded as one of the most promising alternatives owing to their similar optoelectronic properties compared with their Pb counterparts.[15] By leveraging their cost-effectiveness, lead-free composition, and emerging performance capabilities, such as tunable bandgaps and high carrier mobilities, TPSCs exhibit considerable promise for sustainable photovoltaic applications, particularly as environmental concerns and material toxicity regulations are increasingly constraining lead-based technologies.[16] Recently, the PCE of TPSCs has been improved up to 17%, which represents the peak performance among all types of Pb-free PSCs, making it competitive in the field of thin-film photovoltaic technology.[17]

Interest in Sn-based perovskites dates back to 2014, when Kanatzidis and co-workers reported the first example of $MASnI_{3-x}Br_x$ and $MASnI_3$-based PSCs with PCEs of 5.7% and 6.4%,[18,19] respectively. Later, the progress was significantly propelled by the introduction of an inverted device architecture, which achieved a PCE of 6.22% in 2016.[20] However, the initial PCE of TPSCs was substantially lower than that of lead-based perovskite solar cells (LPSCs) during the same period, which could not meet the requirements for commercialization. The crucial challenge toward high-performance TPSCs is the intrinsic Sn^{2+} instability and high Sn^{2+} Lewis acidity of Sn-based perovskites.[21] The easily oxidized Sn^{2+} is a primary cause of instability in TPSCs, and it can induce self-doping effect (p-type doping concentrations reaching 10^{17}–10^{19} cm^{-3}), leading to the formation of deep-level defects and exacerbating non-radiative recombination, which ultimately results in a loss of open-circuit voltage (generally in the range of 0.4–0.6 V).[22] Moreover, the oxidation product Sn^{4+} can react with solvents (such as DMSO) or environmental H_2O/O_2, accelerating the degradation of the material. In addition, the high Lewis acidity characteristic of Sn^{2+} leads to an extremely speedy coordination interaction of SnI_2 with organic cations such as MA^+ and FA^+ and halides (I^-). It makes the crystallization process difficult to control.[23] This rapid crystallization process tends to generate thin-film defects such as pinholes, cracks, and impurities, which also induce severe carrier recombination that exerts a detrimental effect on the photovoltaic performance of TPSCs.[24] Aiming at solving these fundamental problems, researchers shifted their focus to addressing the oxidation issue of Sn-based perovskites from 2016 to 2018. Strategies during this period included additive engineering (*e.g.*, SnF_2) and solvent engineering (*e.g.*, DMSO

He Dong

He Dong received her MS degree in Chemistry Technology from China University of Mining & Technology, Beijing and a PhD in Chemistry from Northwestern Polytechnical University in 2023. Now she works as a Postdoctoral Fellow at this University. She is interested in the development of lead-free tin-based perovskite materials and their application in photoelectric devices.

Weiyin Gao

Weiyin Gao obtained her PhD in Electronic Science &Technology from Xi'an Jiaotong University in 2017. From 2014 to 2015, she was working as a visiting scholar at Case Western Reserve University. She worked as a Postdoc Fellow at Xi'an Jiaotong University from 2017 to 2019 and then in the Institution of Flexible Electronics (IFE) at Northwestern Polytechnical University from 2019 to 2023. Now she works as an Associate Professor at Xi'an Shiyou University. Her research interests mainly include crystallization regulation of Sn-based perovskites and their application in thin-film optoelectronic devices.

Chenxin Ran

Chenxin Ran received his PhD degree in Electronic Science and Technology from Xi'an Jiaotong University in 2016 with Prof. Minqiang Wang. He worked as a Visiting Scholar from 2014 to 2015 with Prof. Liming Dai at Case Western Reserve University and as a Lecturer at Xi'an Jiaotong University from 2016 to 2019. Now he works as an Associate Professor at Northwestern Polytechnical University. His research interests include the photo-physics of Pb-based/Pb-free perovskite materials and their optoelectronic applications.

Published on 01 August 2025. Downloaded on 1/24/2026 5:38:31 AM.

and anti-solvent).[25–28] From 2018 to 2021, researchers further explored the crucial role of crystal structure of Sn-based perovskites in film excellence and the merit of TPSCs, as well as discovered that introducing large-volume cations at the A-site could construct structures of Sn-based perovskites in low dimensions, thereby enhancing the PCE and stability of TPSCs.[29–31] After 2021, various strategies focused on the regulation of crystallization and interfacial defects of Sn-based perovskite films.[32–39] For instance, Chen and his colleagues found that the addition of pyridine fullerene in TPSCs achieved a PCE of 16.05%, while also demonstrating excellent stability (maintaining 99% of the starting PCE following 600 hours of maximum power point tracking under one sun condition).[17] This group further enhanced the performance of pyridine fullerene-based TPSCs with a PCE of 17.13%, which is currently the highest PCE for TPSCs, while also demonstrating excellent stability (stable performance under continuous one-sun exposure in nitrogen for more than 1500 hours without encapsulation).[40]

Fig. 1 shows a brief summary of the key strategies for film quality enhancement and device performance improvement in TPSCs. Structural engineering improves the performance of TPSCs by regulating the composition of the precursors and dimensionality of the crystal structure. For example, the introduction of B-site cations (such as Ge^{2+}) can fill Sn vacancies and suppress the generation of vacancy defects resulting from the Sn^{2+}'s oxidation.[20] Meanwhile, the regulation of X-site anions, such as adjusting the ratio of I^-/Br^-, can balance the crystallization rate and film quality.[41] Dimensionality engineering primarily originates from the regulation of A-site cations, which not only optimizes the structure of the perovskite but also induces the formation of low-dimensional structures, thereby regulating crystallization orientation and forming hydrophobic layers.[42] Moreover, during the annealing process of the film, crystallization engineering employs strategies such as solvent engineering and the introduction of additives (*e.g.*, coordinating ions) to control the kinetics of grain growth, performing an essential function in swift nucleation and delayed crystallization.[20] Moreover, in the device fabrication process of TPSCs, interfacial modification materials are introduced between the perovskite film and the charge-transport layer (for holes or electrons) to enhance the physical contact and energy-level alignment at the interfaces.[43] This approach serves a vital function in diminishing non-radiative recombination, suppressing ion migration, as well as enhancing carrier transport PCE.[44] Considering the inspiring progress made in the field recently, it is of great significance to provide a timely and comprehensive review for the community at this point.[45]

In this review, we meticulously curate and summarize the current research status of TPSCs, while casting a forward-looking gaze on their potential for performance enhancement. Initially, we delve into the fundamental characteristics of Sn-based perovskites from a structural perspective, elucidating their intricate influences on PSC performance. Then, the state-of-the-art strategies toward high-performance TPSCs are highlighted, including structural engineering, crystallization regulation and interface engineering. Finally, we present future challenges facing Sn-based perovskites and provide crucial perspectives for efficient and stable TPSCs, which will offer pivotal insights into the advancement of high-performance TPSCs but will also be instrumental in fostering research on stacked solar cells based on Pb–Sn mixed perovskites.

2. Fundamentals of Sn-based perovskites

2.1 Crystalline structure

Perovskite materials typically possess an ABX_3-type crystal structure (Fig. 2a), where the A-site is taken up by a univalent organic cation (for example, FA^+, MA^+, and Cs^+), the B-site by a bivalent cation (Sn^{2+} and Pb^{2+}), and the X-site by a halide anion (*e.g.*, I^-, Br^-, and Cl^-).[46] This structure features a three-

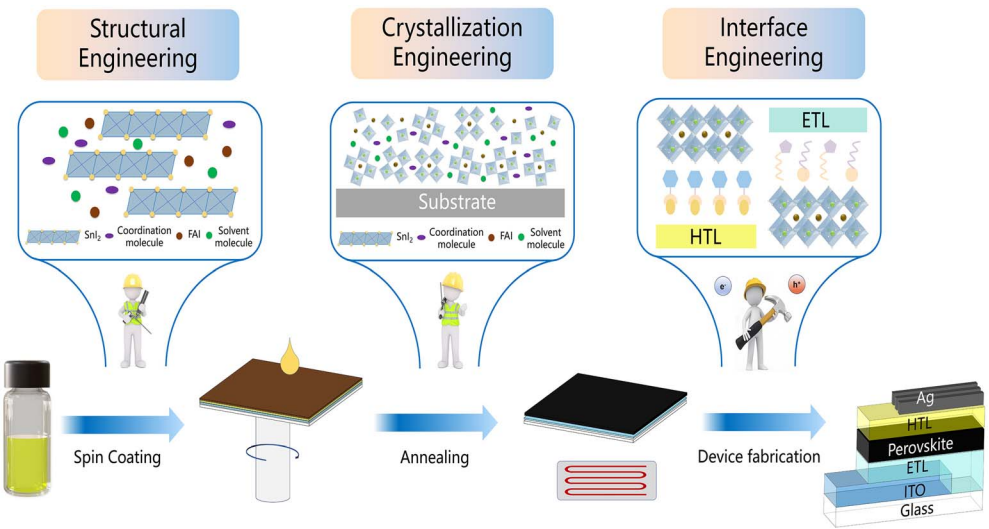

Fig. 1 Schematic of the key strategies for film quality enhancement and device performance improvement in TPSCs.

 This journal is © The Royal Society of Chemistry 2025

Published on 01 August 2025. Downloaded on 1/24/2026 5:38:31 AM.

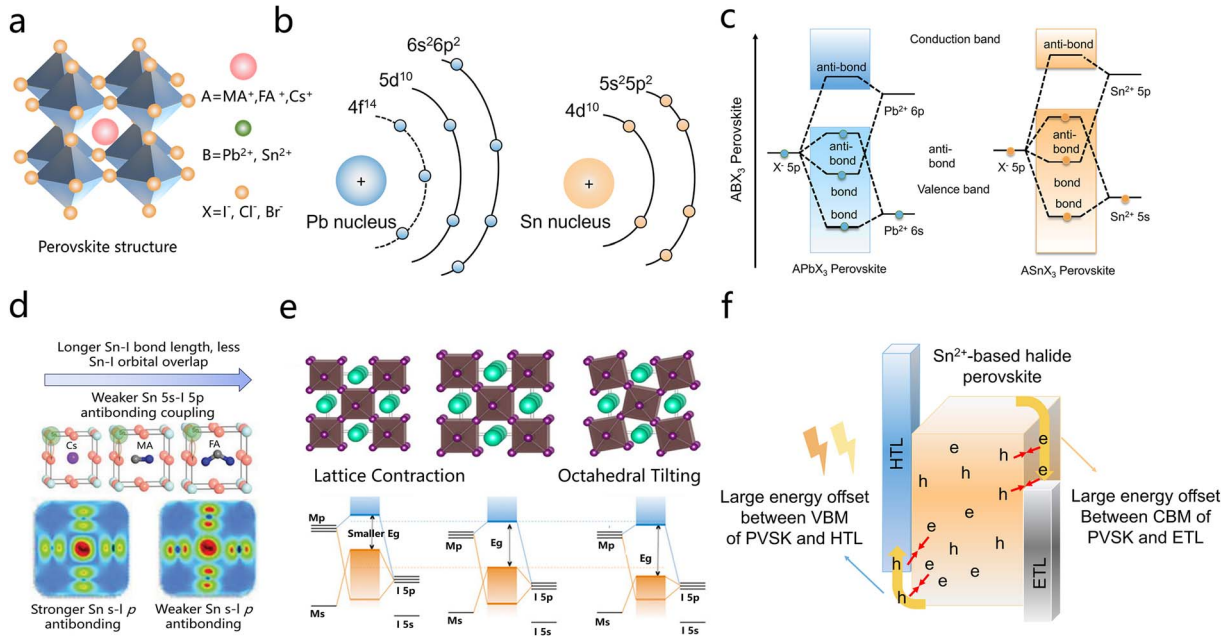

Fig. 2 (a) Diagram of the perovskite structure. (b) Schematic of the lanthanide contraction of Sn and Pb atoms.[50] Copyright 2021, the American Chemical Society. (c) Schematic energy level diagram of $APbX_3$ and $ASnX_3$ perovskites.[50] Copyright 2021, the American Chemical Society. (d) Top: schematic of the influence of A-site cation-affected bond lengths on Sn 5s–I 5p antibonding coupling, bottom left: modulation of the partial charge density near the VBM energy level of $MASnI_3$, bottom right: modulation of the partial charge density near the VBM energy level of $FASnI_3$.[51] Copyright 2017, the Royal Society of Chemistry. (e) Schematic of lattice contraction (left), cubic (center), and tilted lattice (right), with a schematic at the bottom showing the effect of lattice distortion on the energy level alignment of the band gap.[52] Copyright 2017, the American Chemical Society. (f) Working mechanism of PSCs.

dimensional network of corner-sharing $[SnX_6]^{4-}$ octahedra, along with the larger A-site cations residing in the cuboctahedral voids to stabilize the lattice framework.[47] The optical and electrical properties of perovskite materials are greatly affected by the composition of A-site cations as well as X-site anions. Furthermore, the Goldschmidt tolerance factor and octahedral tilting mechanisms critically govern lattice stability and symmetry, leading to the formation of cubic ($Pm\bar{3}m$), tetragonal ($I4/mcm$), or orthorhombic ($Pnma$) phases under different temperature and composition conditions.[48] Cations of the A-site cation profoundly modulate phase stability as well as transition pathways in Sn-based perovskites. For instance, formamidinium (FA^+), with its large ionic radius, suppresses octahedral tilting in $FASnI_3$, stabilizing a quasi-cubic phase under indoor temperature and more effectively reserving the photoactive black phase compared to its lead counterpart. In contrast, methylammonium (MA^+) in $MASnI_3$ induces a tetragonal-to-orthorhombic transition below 200 K, introducing anisotropic strain and temperature-dependent bandgap widening.[49] $CsSnI_3$, containing the smaller Cs^+ ion, demonstrates complex phase coexistence: a black orthorhombic (B-γ) phase and a yellow non-perovskite (Y) phase persist under indoor temperature, with a cubic-to-orthorhombic transition near 300 K correlating to abrupt increases in carrier effective mass and defect density.[41] In addition, the incorporation of X-anions (*e.g.*, Br^- and Cl^-) can effectively tune the bandgap of Sn-based perovskites.[41] These cation/anion-dependent phase dynamics critically affect optoelectronic properties, for example, carrier mobility and absorption profiles, highlighting the imperative of strategic structural engineering to suppress detrimental phase transitions and optimize device performance.

2.2 Optoelectronic properties

Sn-based perovskites exhibit unique electronic structures characterized by Sn^{2+} $5s^2$ orbital contributions, resulting in a narrower bandgap (1.2–1.4 eV) compared to Pb-based analogues (Fig. 2b). The valence band maximum (VBM) comes from hybridization between Sn 5s and I 5p orbitals, and the conduction band minimum (CBM) originates from Sn 5p–I 5p anti-bonding states. Due to the higher energy levels of Sn-5s and Sn-5p atomic orbitals relative to Pb-6s and Pb-6p orbitals, both the CBM and VBM in Sn-based perovskites are positioned at elevated energies. The higher energy level of Sn-5s compared to that of Pb-6s makes the Sn–I bonds easy to break, leading to a high density of Sn vacancy defects. Furthermore, the inherently weak Sn–I bond facilitates reactions with H_2O and O_2. Notably, the shorter bond length in $MASnI_3$ (relative to $FASnI_3$) enhances antibonding coupling, thereby elevating the VBM to a higher energy level. This effect is primarily attributed to the smaller size of the MA molecule compared to FA. Consequently, under equivalent growth conditions, V_{Sn} defects exhibit lower formation energies in $MASnI_3$ than in $FASnI_3$.[51,52]

As discussed above, the VBM and CBM of Sn perovskites are mainly composed of Sn 5s and 5p orbitals hybridized with I 5p orbitals. Consequently, the crystal structure directly modulates

Published on 01 August 2025. Downloaded on 1/24/2026 5:38:31 AM.

their optical properties. As demonstrated in Fig. 2d, isotropic lattice contraction correlates with a reduced band gap, illustrating that structural modifications enhancing metal-halide orbital overlap narrow the band gap, while those diminishing such overlap widen it. For instance, by replacing MA^+ with FA^+ in these compositions, the bandgap can be turned from 1.25 eV to 1.41 eV, as larger A-site ions can introduce structural distortions that diminish Sn–I orbital overlap. Conversely, expanding the X-site anion from I^- to Br^- reduces the band gap due to altered orbital energy alignment. Additionally, the choice of divalent metal(II) significantly modulates spin–orbit coupling strength, directly impacting the bandgap magnitude and potentially splitting degenerate bands. This is exemplified by the distinct electronic structures of pure Pb and Sn perovskites: in Sn–Pb mixed systems, the VBM originates from hybridized I 5p and metal(II) 5s states, while the CBM is dominated almost exclusively by metal(II) 5p states. A critical advantage of Sn–Pb perovskites lies in the bowing effect, which enables achieving remarkably narrow bandgaps (down to ~1.2 eV)—far below those of pure compounds. This property not only facilitates approaching the Shockley–Queisser limit in single-junction solar cells but also makes these materials ideal for fabricating bottom sub-cells in all-perovskite tandem devices.

These property-tunable band gaps, high carrier mobility, and defect tolerance synergistically enable efficient tin-based perovskite solar cell (TPSC) operation by balancing light absorption, charge transport, and structural stability (Fig. 2f). The optimal bandgap facilitates broad spectral absorption spanning visible to near-infrared wavelengths, while high carrier mobility ensures rapid charge extraction, minimizing recombination losses. However, intrinsic Sn^{2+} oxidation and illumination-induced phase instability remain critical challenges, necessitating strategies such as encapsulation or reducing agent integration to mitigate degradation.[53] Advanced approaches including mixed A-site cation engineering and interfacial passivation suppress non-radiative recombination losses, thereby achieving the PCE exceeding 15%.

2.3 Oxidation and degradation pathways

The preparation of TPSCs involves three sequential stages, namely precursor preparation, film fabrication, and device storage and operation. Each is susceptible to Sn^{2+} oxidative degradation (Fig. 3a and b). (I) Precursor preparation: Sn^{2+} oxidation to Sn^{4+} occurs *via* redox reactions with oxygen-containing solvents (*e.g.*, dimethyl sulfoxide, DMSO, forming Sn^{4+} and dimethyl sulfide) and dissolved O_2, particularly under alkaline conditions that lower the reduction potential for Sn^{4+} conversion, promoting the $[Sn(OH)_6]^{2-}$ formation.[54,55] (II) Film fabrication: trace O_2 and moisture in gloveboxes induce Sn perovskite oxidation, generating SnI_4 and I_2, which cyclically exacerbate Sn^{2+} oxidation.[56] Lattice instability from low/high Sn^{2+} concentrations reduces Sn^{4+} formation energy, accelerating Sn vacancy (V_{Sn}) formation and subsequent Sn^{2+} loss.[51,57,58] (III) Device storage and operation: light exposure generates photoexcited electrons that convert O_2 to superoxide (O_2^-), accelerating Sn^{2+} oxidation more severely than dark conditions.[59,60] UV-treated electron transport layers (ETLs, *e.g.*, TiO_2, ZnO) produce electron–hole pairs, with holes reacting with adsorbed O_2 to induce Sn^{2+} oxidation, while acidic/oxidizing hole-transport layers (HTLs, *e.g.*, PEDOT:PSS) further degrade TPSCs.[61,62]

2.4 Deposition methods

2.4.1 Synthetic approaches for perovskite films. The fabrication of high-quality Sn perovskite films is crucial for realizing the advantages of TPSCs, such as high carrier mobility and an adjustable bandgap. Films with fewer pinholes and grain boundary defects can reduce non-radiative recombination and enhance charge transport and collection, thereby improving the open-circuit voltage. Moreover, developing preparation methods for high-quality Sn perovskite films is vital for the commercialization of TPSCs. However, challenges such as Sn-based perovskites' oxidization, rapid and uncontrollable crystallization, and high defect state density pose significant hurdles in film preparation. The main preparation methods for Sn-based perovskite films are solution processing (primarily spin-coating), thermal co-evaporation, and vapor-assisted solution processes (VASP).[64]

2.4.1.1 Solution method. The solution process is widely used in preparing Sn halide-based perovskite materials and devices. It is a cost-effective, easily processable, and tunable technique that can produce highly functional layers in devices. Solvent engineering and adjusting the annealing temperature are key aspects of solution-processed tin perovskite film fabrication. Common solution-based methods include spin-coating, blade-coating, slot-die coating, spray-coating, inkjet printing, and drop-casting, with spin-coating being the most prevalent in the lab.[65] Spin-coating involves dropping the perovskite precursor solution onto a rapidly spinning substrate. The centrifugal force spreads the solution uniformly, and annealing rapidly dries it into a thin film. It can be divided into one-step method and two-step method. The one-step method involves pre-mixing Sn-perovskite precursors (*e.g.*, SnI_3 and MAI) in a solvent; after spin-coating, the solution crystallizes directly into the perovskite phase. Jiang *et al.* used anti-solvents such as 1,2-dichlorobenzene (DCB) to optimize the duration of nucleation and crystal growth stages. Adding the anti-solvent 10 s into spinning reduced compressive strain, suppressed non-radiative recombination, and produced high-quality films. This achieved a high efficiency of 14.85% and good stability (maintaining 96% of initial efficiency after 190 hours of continuous MPP tracking).[66] Chan *et al.* combined the one-step method with annealing. After spin-coating, they added the ligand iso-butylammonium iodide (iso-BAI) and spin-annealed (80 °C, 10 minutes), inducing recrystallization and improving film morphology to reach 14.2% efficiency.[67] Although the one-step method is rapid and simple, its crystallization is difficult to control, which often requires anti-solvents for regulation. To address this, the two-step spin-coating method was developed. It involves spin-coating a SnI_2 layer followed by an organic salt solution (*e.g.*, MAI), with the perovskite film forming *via* solid-state diffusion (Fig. 4a). Shih *et al.* used this method and replaced traditional

 This journal is © The Royal Society of Chemistry 2025

Published on 01 August 2025. Downloaded on 1/24/2026 5:38:31 AM.

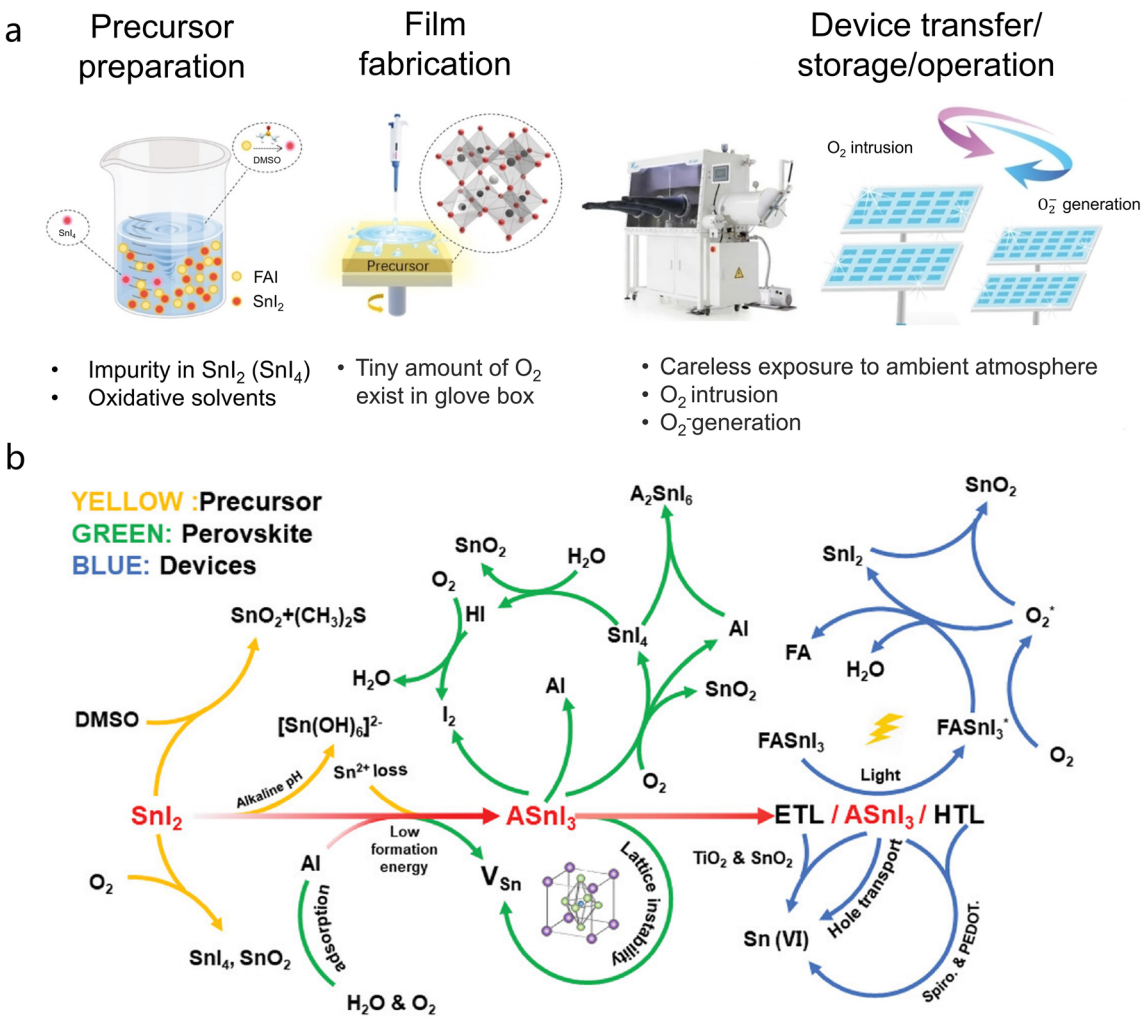

Fig. 3 (a) Oxidative factors for the fabrication of Sn-based perovskite devices.[21] Copyright 2023, Wiley-VCH GmbH. (b) Oxidation principles for the fabrication of Sn-based perovskite devices.[63] Copyright 2023, Wiley-VCH GmbH.

anti-solvents with a solvent-additive system (isopropyl alcohol, hexafluoroisopropanol, and chlorobenzene), reducing film damage and achieving 8.7% device efficiency.[68] Kuan *et al.* prepared Sn-perovskite films on PEAI-modified PTAA surfaces *via* two-step spin-coating. The ammonium cations in PEAI interacted with SnI_2 and FAI_2 precursors, decreasing pinholes and defects. This resulted in high-quality films and 8.3% device efficiency.[69]

2.4.1.2 Thermal co-evaporation. Thermal co-evaporation, a physical vapor deposition technique, involves the synchronous or sequential evaporation of multiple precursor materials in a vacuum or inert gas environment. These materials deposit and react on the substrate surface to form perovskite thin films (Fig. 4b). The enclosed environment of this process effectively isolates the material from oxygen and moisture, significantly suppressing the oxidation of Sn^{2+} in Sn-based perovskites. This results in highly uniform and fully covered films. Yu *et al.* pioneered the synthesis of high-quality $MASnI_3$ films at room temperature using thermal evaporation. The deposited $MASnI_3$ films, without post-deposition annealing, exhibited high crystallinity, smooth surfaces, wide coverage, and strong preferential crystallization along the ⟨100⟩ direction, achieving an efficiency of 1.7%.[70] However, Sn-based perovskite films, being multi-component, have constituents with varying densities, melting points, and reaction rates. This necessitates evaluating the adaptability of Sn-based perovskite films to the thermal co-evaporation method. Sequential thermal evaporation emerges as the most effective approach as it creates ultrathin layers of raw materials, enabling effective reactions among the chemical components. Moghe *et al.* deposited $CsSnBr_3$ films using sequential co-evaporation of CsBr and $SnBr_2$ in a ratio of 1/1 in a nitrogen atmosphere. Testing unencapsulated TPSCs revealed enhanced stability, with the devices retaining over 80% of their initial efficiency for 50 minutes in air.[71]

2.4.1.3 Vapor-assisted solution process. The VASP is a two-step method for preparing perovskite films. First, a precursor film (*e.g.*, SnI_2) is deposited, followed by vapor-assisted transformation (*e.g.*, CsI) (Fig. 4c). VASP forms perovskite structures *via* solid–gas reactions between organic amine salt vapors and solid-state lead halide films, avoiding solvent residue and rapid

Published on 01 August 2025. Downloaded on 1/24/2026 5:38:31 AM.

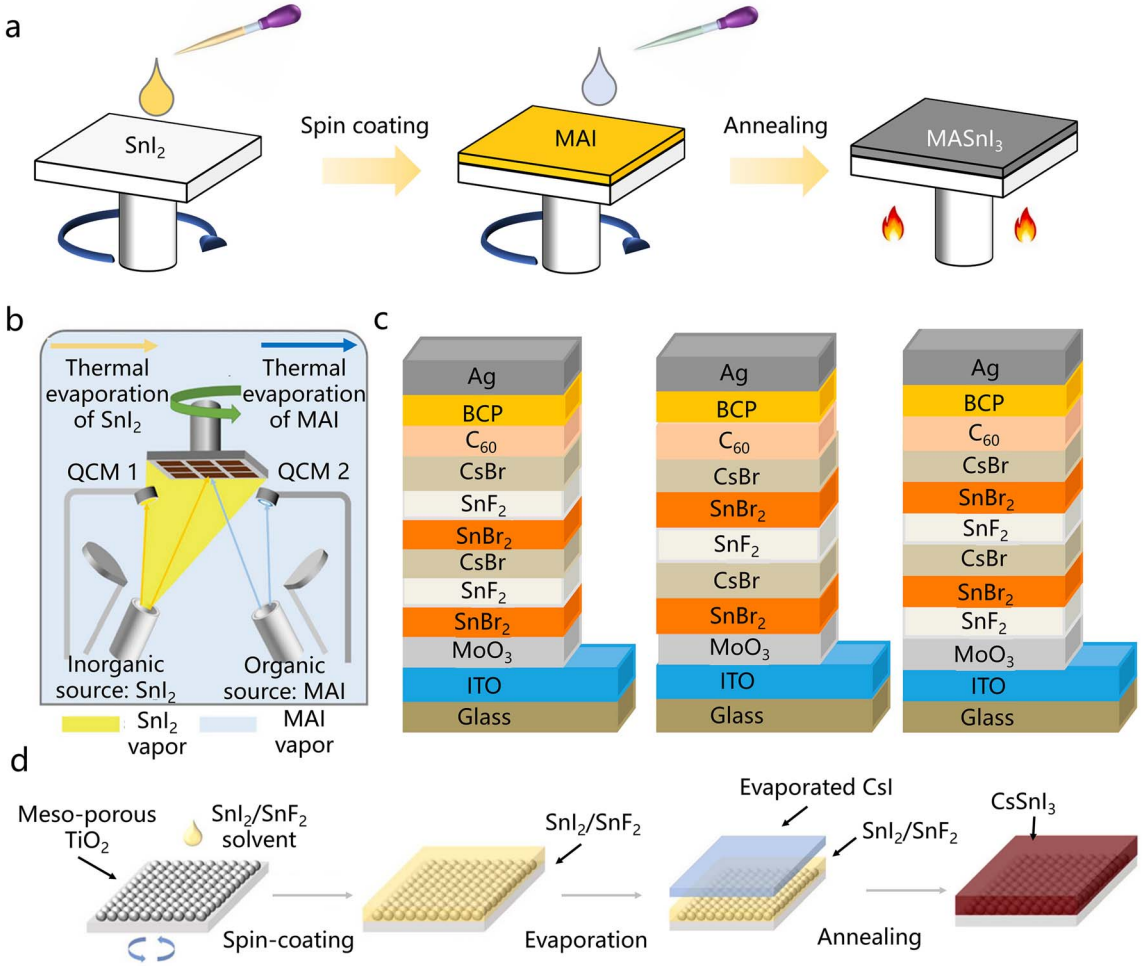

Fig. 4 (a) Procedure of the spin-coating method (using the two-step method as an example). (b) Procedure of the thermal co-evaporation method.[70] Copyright 2023, the American Chemical Society. (c) Example of the sequential co-evaporation method.[71] Copyright 2023, Wiley-VCH GmbH. (d) Procedure of the VASP method.[74] Copyright 2023, Wiley-VCH GmbH.

crystallization issues common in traditional solution-based methods. By combining solution processing with gas phase deposition, VASP is suitable for generating large perovskite grains, which can reduce trap density, leakage paths, and non-radiative recombination. Wang *et al.* presented a VASP strategy where solid-state SnF_2 reacts with gaseous MAI through ion exchange or insertion to form $MASnI_3$ films. This approach enables controlled nucleation and crystallization of $MASnI_3$, yielding highly uniform, pinhole-free films. The residual SnF_2 also suppresses oxidation in $MASnI_3$ films, boosting the TPSC efficiency to 7.78%.[72] Yokoyama *et al.* improved the VASP method by introducing the low-temperature vapor-assisted solution process (LT-VASP). They inserted glass spacers between the substrate and the sample in a Petri dish to better control substrate temperature during VASP by adjusting the spacer quantity. This enhancement led to TPSCs achieving 1.86% efficiency and improved air stability.[73]

2.4.2 Synthetic approaches for other functional layers. Enhancing the fabrication methods of functional layers (ETLs and HTLs) can optimize energy level alignment and mitigate interfacial energy losses. Some ETLs/HTLs also block water and oxygen permeation, thereby improving TPSCs' stability. However, issues such as low carrier mobility, energy level mismatches, and chemical instability still plague functional layers. Consequently, the subsequent discussion will focus on the fabrication methods of HTLs and ETLs in TPSCs.

2.4.2.1 HTL. The deposition of HTLs primarily employs spin-coating and dip-coating techniques. Zhang *et al.* spin-coated SAMs, specifically [2-(3,6-dimethoxy-9*H*-carbazol-9-yl) ethyl]phosphonic acid (MeO-2PACz) and [4-(3,6-dimethyl-9*H*-carbazol-9-yl)butyl]phosphonic acid (Me-4PACz), onto PEDOT:PSS to form a buffer layer. This process enhanced the carrier mobility of the SAM-HTL. The procedure involved initially spin-coating SAM onto the substrate, followed by an ethanol rinse, and subsequent spin-coating of PEDOT:PSS and perovskite films (Fig. 5a). The device efficiency improved from 5.7% to 7.3%.[75] Additionally, Song *et al.* utilized dip-coating to fabricate SAM-HTL layers (Fig. 5b). Dip-coating offers better compatibility and reduces pinholes and defects compared to spin-coating. In their study, MeO-2PACz and 6PA were introduced in equal proportions, and the SAM coating on the HTL alleviated the separation between the tin perovskite film and

 This journal is © The Royal Society of Chemistry 2025

Published on 01 August 2025. Downloaded on 1/24/2026 5:38:31 AM.

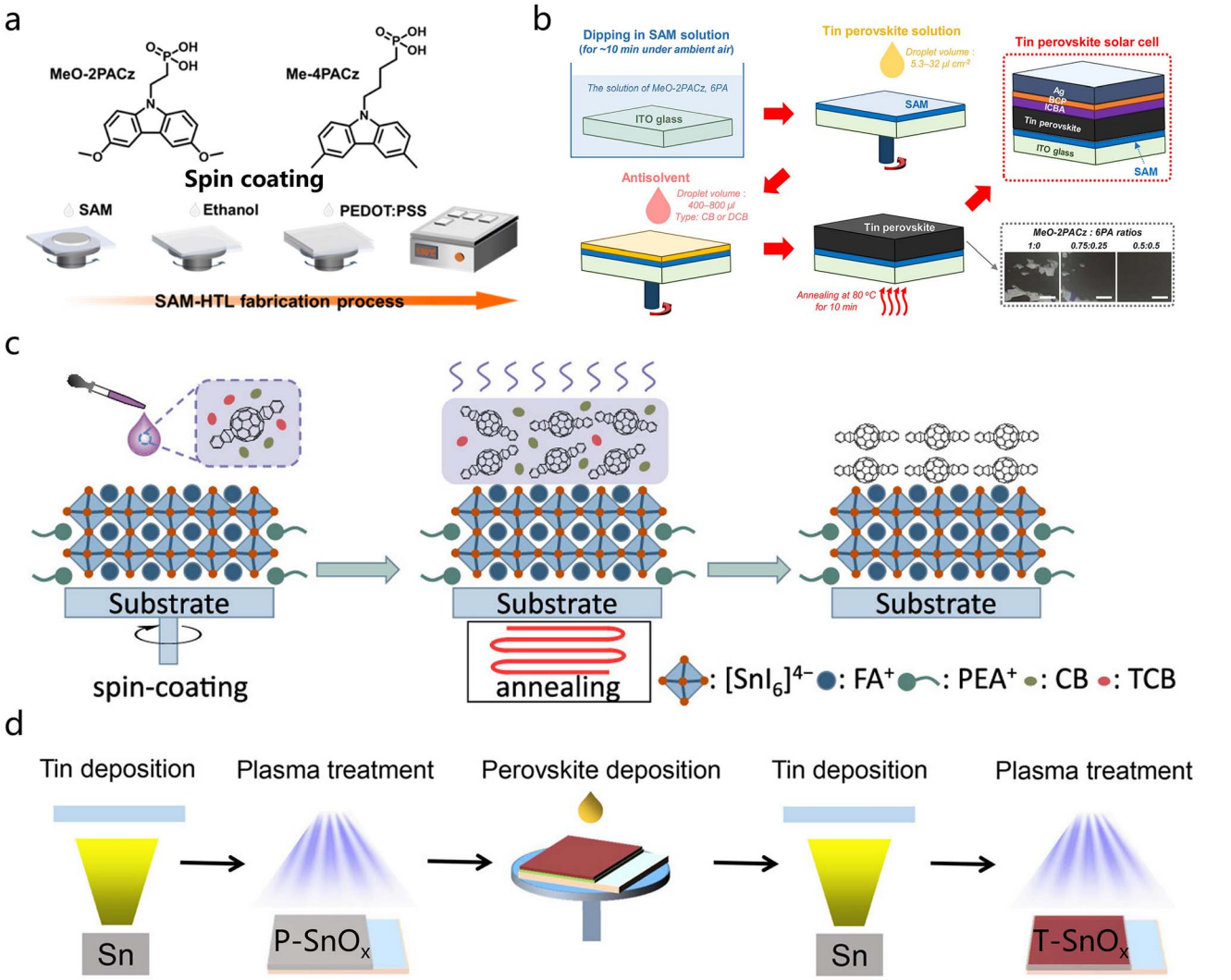

Fig. 5 (a) Schematic of the SAM/HTL fabrication by the spin-coating method.[75] Copyright 2021, the American Chemical Society. (b) Schematic of the procedures for creating SAMs with distinct MeO-2PACz : 6PA molar ratios on glass substrates coated with ITO, followed by the formation of tin perovskite films on top of these SAM-based HTLs utilizing an antisolvent-assisted dipping technique.[76] Copyright 2022, the American Chemical Society. (c) Schematic of the ICBA film fabrication by spin-coating.[36] Copyright 2023, the American Chemical Society. (d) Schematic of the fabrication procedure of P-SnO_x or T-SnO_x by a plasma-assisted method.[77] Copyright 2022, Springer Nature.

functional layers. They also employed a sticky silicon substrate to grow high-quality SAM-HTLs. The final device efficiency reached 9.4%.[76]

2.4.2.2 ETL. Deposition methods for ETLs mainly include spin-coating and plasma-assisted techniques, among others. Liu *et al.* prepared ICBA as an HTL material *via* spin-coating and investigated optimal fabrication conditions. They used a mixed solvent of chlorobenzene and 1,2,4-trichlorobenzene (CB : TCB = 10 : 1) and increased the annealing temperature of ICBA films from 70 °C to 100 °C (Fig. 5c). These optimal conditions significantly reduced energy disorder within the ICBA films, elevating the open-circuit voltage to 1.01 V and achieving an efficiency of 11.57%.[36] In another study, Wang *et al.* employed plasma-assisted methods to fabricate both HTL and ETL layers, where P-SnO_x served as the HTL and T-SnO_x as the ETL, with a Sn-to-O ratio of 1 : 1.77. T-SnO_x, a variant of SnO_x with distinct stoichiometry, functioned as an *in situ* modifier and protective layer for the perovskite layer (Fig. 5d). It reduced Sn^{4+} to Sn^{2+} and decreased defect density. The plasma-assisted method, known for its simplicity and speed, enabled TPSCs to reach an efficiency of 13.82%.[77]

3. Advanced strategies for efficient TPSCs

3.1 Structural engineering

3.1.1 Compositional engineering

3.1.1.1 A-site cation. The A-site cation performs a vital function in the perovskite structure of ABX_3. An ideal three-dimensional perovskite structure can be regarded as a framework composed of [SnX_6] octahedra connected *via* corner-sharing in a three-dimensional space, with the A-site cation

Published on 01 August 2025. Downloaded on 1/24/2026 5:38:31 AM.

filling the 12-fold coordinated interstitial sites between the octahedra. Therefore, the selection of appropriate A-site cations is of great significance for constructing stable perovskite structures. To date, methylammonium (MA^+), formamidinium (FA^+), and cesium (Cs^+) have been considered as the three relatively suitable A-site cations.[78] In $FA_{1-x}Cs_xSnI_3$, the material's bandgap gradually decreases with the increase in Cs^+ content (Fig. 6a). This is mainly due to the absence of octahedral tilting during the substitution process, along with lattice contraction, leading to enhanced overlap between orbitals.[52] Meanwhile, the doping of Cs^+ can enhance the $FASnI_3$ perovskite structure's stability (Fig. 6b and c).[79] Research has found

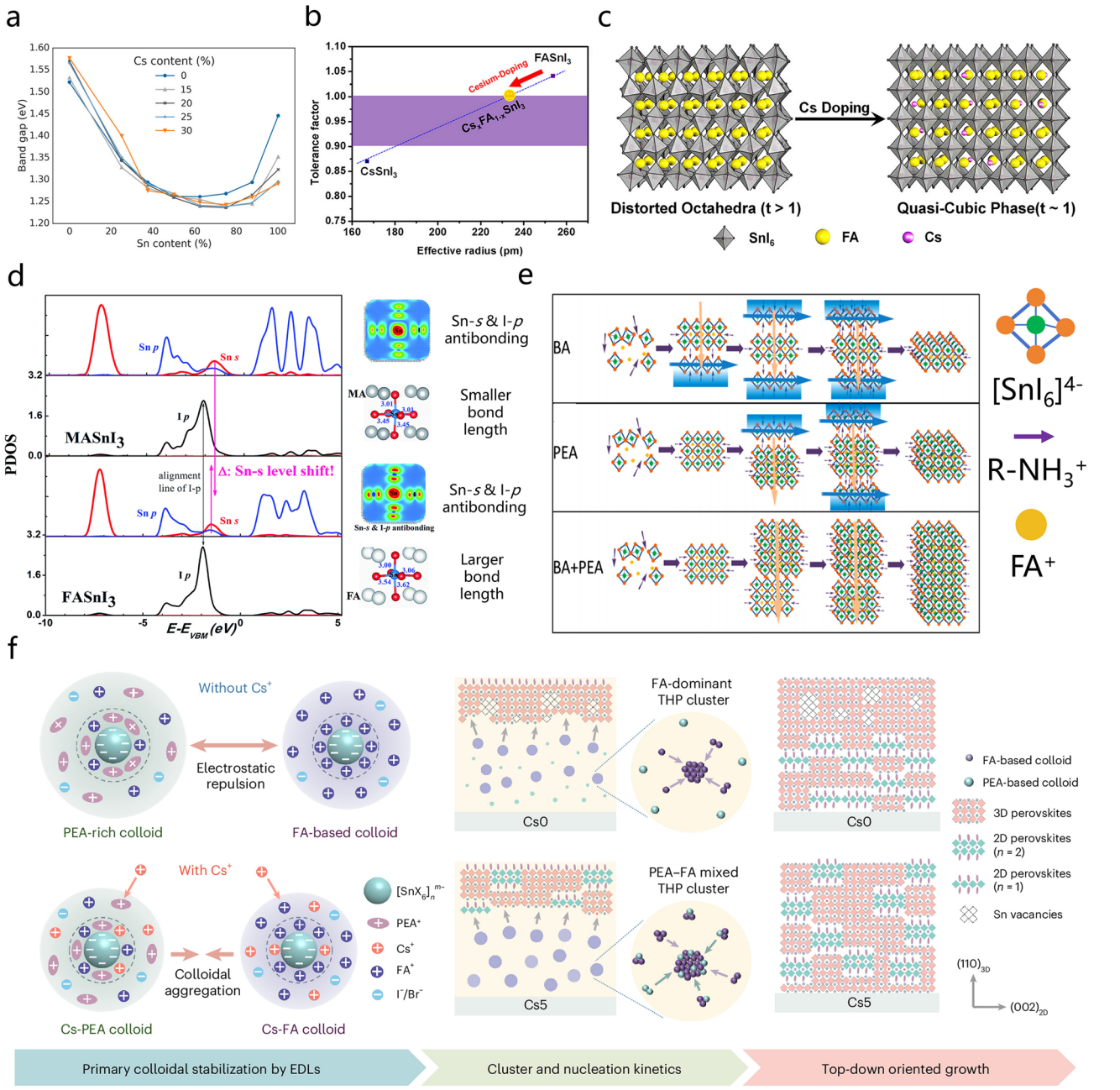

Fig. 6 (a) Variation in the perovskite bandgap with increasing Sn content for different Cs doping levels.[52] Copyright 2017, the American Chemical Society. (b) Correlation between the tolerance factor and the effective radius of Cs/FA cations in $Cs_xFA_{1-x}SnI_3$ perovskites.[79] Copyright 2018, the American Chemical Society. (c) Schematic of the structure transition when $FASnI_3$ is doped with an appropriate content of Cs.[79] Copyright 2018, the American Chemical Society. (d) Electron density clouds between the I 5p and Sn 5s orbitals in $MASnI_3$ and $FASnI_3$ perovskites.[80] Copyright 2017, the Royal Society of Chemistry. (e) Schematic of the crystal growth processes of 2D RP Sn perovskites based on BA, PEA, and BA + PEA.[87] Copyright 2017, the American Chemical Society. (f) Schematic of the colloidal stabilization mechanisms of PEA-rich colloids and FA-based colloids, the formation of clusters and nucleation kinetics, and the growth processes of 2D–3D TPSC with and without Cs^+ doping.[40] Copyright 2025, Springer Nature.

 This journal is © The Royal Society of Chemistry 2025

Published on 01 August 2025. Downloaded on 1/24/2026 5:38:31 AM.

that the larger-size ionic radius of FA^+ impairs the anti-bonding coupling interaction between I 5p and Sn 5s (Fig. 6d). Under the same growth conditions, the energy required to form Sn vacancies in $FASnI_3$ is greater than that in $MASnI_3$, resulting in a more stable perovskite structure, which is currently a promising perovskite material system.[80] Moreover, the A-site cation affects the optical bandgap of perovskites. Although the A-site ion does not directly influence the band edge of perovskites, it can indirectly modulate the bandgap by affecting the structure of the octahedra. For instance, the bandgap of $FASnI_3$ is 1.41 eV. It is notably greater than that of $MASnI_3$ (1.20 eV).[81] In recent years, the development of new A-site cations has been an important part of compositional engineering. Jokar *et al.* mixed guanidinium (GA) with FA and designed a "hollow" perovskite using ethylenediamine dihydroiodide ($EDAI_2$).[82] It was found that GA^+ can lower the VBM and inhibit the oxidation of perovskites in humid environments. A perovskite solar cell based on $GA_{0.2}FA_{0.78}EDA_{0.01}SnI_3$ achieved a photoelectric PCE of 9.6%. Additionally, ethylenediamine (en) was used to prepare a novel Sn perovskite with a hollow structure.[83] The larger size and doubly charged en weakens the overlap between Sn–I orbitals in the perovskite lattice. While creating a hollow structure, it can retain the three-dimensional perovskite structure. The bandgap of $FASnI_3$ perovskite can be enhanced from 1.3 eV to approximately 1.9 eV with the increase in content. The chemical formula of the organic cation guanidinium (GA^+) is $C(NH_2)_3^+$, which has attracted the attention of researchers due to its dipole moment being approximately zero.[84]

When larger organic amine cations (such as phenethylammonium (PEA^+) and butylammonium (BA^+)) are used to replace FA^+, the perovskite crystal structure will transform from three-dimensional to two-dimensional layered structures. Two-dimensional halide perovskites can be regarded as derivatives of three-dimensional perovskites obtained by slicing along specific crystal planes, possessing more controllable lattice structures and diverse optoelectronic properties. Due to its larger size, PEA doped in perovskite films can disrupt the octahedral structure, thereby forming two-dimensional perovskites. This helps to suppress the formation of Sn vacancies, thereby reducing the carrier density and achieving high crystallinity and superior crystal orientation.[85] Meanwhile, Liao *et al.* doped 20% PEA into perovskites, enhancing the stability of the films and devices. This is because PEA orients the crystallization along the vertical direction, preventing the ingress of moisture.[86] Moreover, larger organic amine cations can modulate the optoelectronic properties of Sn perovskites. For a hydrophobic cation, butylammonium (BA^+) can optimize the growth direction of perovskite films, thereby obtaining a favorable charge transport direction and improving the optoelectronic properties of perovskites.[87] Moreover, the combined effect of BA^+ and PEA^+ can effectively inhibit the formation of intermediate phases during the crystallization of Sn perovskites, resulting in uniform and orderly nucleation. This leads to significant improvements in film morphology and crystal orientation, substantial suppression of trap recombination, and an achieved photoelectric PCE of 8.82% (Fig. 6e).[87] Research has shown that the synergistic effect of BA^+ and EDA^{2+} can not only alter the crystal growth direction and improve grain connectivity but also reduce pinholes on perovskite films, preventing the ingress of water and air, improving the crystal structure's stability, and thus, increasing the photovoltaic performance of Sn-PSC.[88] In addition to the aforementioned studies, Du *et al.* designed 3AMPY (3-(aminomethyl)pyridinium) to fill the A-site. The intense coordination interaction between $3AMPY^{2+}$ and the 3D perovskite components, as well as the nucleation sites introduced by $3AMPYSnI_4$ crystals, not only reduces the low-*n*-value 2D phases and increases the 3D perovskite phase, but also inhibits the oxidation of Sn^{2+} and self-p-doping in Sn perovskites. This results in lower trap density and non-radiative recombination loss, faster carrier extraction and transfer, and enhanced stability for 2D–3D TPSCs. Consequently, the PCE of the optimized devices increased from an initial 10.91% to 13.28%, and they retained 96.0% of their original performance for over 3000 hours in a N_2 atmosphere.[89] However, the high aggregation barrier precludes the formation of stable clusters by 2D perovskite colloids, thereby rendering the nucleation rate of 2D Sn perovskites slower than that of their 3D counterparts. This disparate nucleation kinetics can lead to suboptimal 2D–3D phase separation, which, in turn, adversely affects the photovoltaic performance and device durability. The incorporation of large cations in combination with a small amount of cations can ameliorate this issue. In the most recent studies, Cs^+ has been introduced to partially substitute the bulk organic cations within the electric double layer of 2D Sn perovskite colloids, thereby decreasing the scale of the colloids and lowering their assembling barriers. The diminished electrostatic repulsion facilitates the aggregation of 2D and 3D THP colloids in the precursor solution, aligning their nucleation kinetics, and thus, yielding 2D–3D heterostructured Sn perovskite films with uniform microstructures and significantly reduced trap states. As a result, an impressive PCE of 17.13% was achieved. Moreover, the device demonstrated excellent stability, it operated stably for over 1500 hours within continuous one sun exposure under nitrogen-unencapsulated condition (Fig. 6f).[40]

3.1.1.2 B-site cation. Perovskites' conduction band (CB) is primarily composed of the p orbitals of the B-site cations. The valence band (VB) consists of the p orbitals of the X site anions as well as the s orbitals of the B site cations. Therefore, the composition of the B-site cations significantly influences the band structure, thin-film morphology, and photovoltaic performance of perovskites. Moreover, the appropriate choice of B-site cations can enhance perovskite structure's stability.[90]

The Ge^{2+} ion, as a member of group IVA, has an electronic configuration and energy level structure that endows Ge-doped perovskite materials with a relatively narrow bandgap range, thereby providing excellent optoelectronic properties. Sn–Ge compounds with narrower bandgaps have a broader light absorption range and can absorb light with longer wavelengths due to their wider absorption spectrum (Fig. 7a). Ju *et al.* predicted through first-principles calculations that many mixed Sn–Ge perovskites possess direct bandgaps, with nine Sn–Ge-based materials exhibiting bandgaps within the optimal range (0.9–1.6 eV) (Fig. 7b).[91] Meanwhile, Cheng *et al.* demonstrated

Published on 01 August 2025. Downloaded on 1/24/2026 5:38:31 AM.

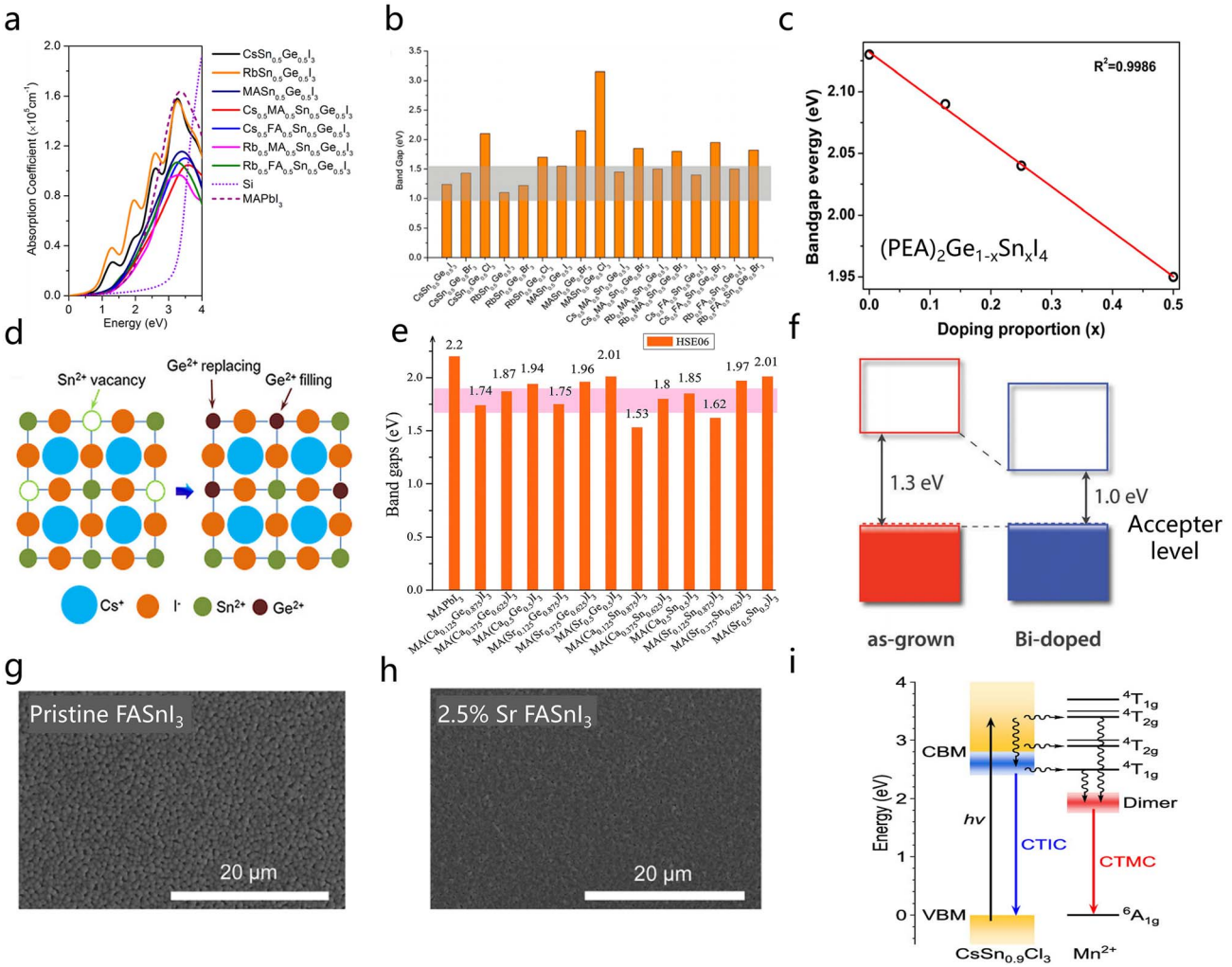

Fig. 7 (a) Calculated optical absorption spectra of several predicted materials (based on the PBE0 functional) compared with the computed spectrum of prototypical Si.[91] Copyright 2017, the American Chemical Society. (b) Electronic band gaps of perovskites with favorable Goldschmidt tolerance factors. The optimal bandgap range for solar cell materials is highlighted by the light gray horizontal bar.[91] Copyright 2017, the American Chemical Society. (c) Variation in the bandgap as a function of x.[92] Copyright 2018, the American Chemical Society. (d) Schematic of the effects of Ge filling of Sn vacancies and substitution of Sn atoms by Ge atoms in the nanocrystalline structure.[93] Copyright 2020, Wiley-VCH GmbH. (e) Bandgap values calculated using the HSE06 functional. The light pink horizontally shaded area represents the ideal bandgap range (1.7–1.9 eV) for the top cell in a tandem structure.[94] Copyright 2018, the Royal Society of Chemistry. (f) Band diagrams of Bi-doped and undoped $FASnI_3$ perovskites.[95] Copyright 2017, the Royal Society of Chemistry. (g) 0% Sr and (h) 2.5% Sr of $FASnI_3$.[96] Copyright 2019, the American Institute of Physics. (i) Proposed energy level diagrams for the PL of $CsSn_{0.9}Mn_{0.1}Cl_3$.[97] Copyright 2019, the American Chemical Society.

that the bandgap of the lead-free two-dimensional blended Ge–Sn halide perovskite $(PEA)_2Ge_{1-x}Sn_xI_4$ decreases proportionally with the increase in Sn concentration. Among these, $(PEA)_2Ge_{0.5}Sn_{0.5}I_4$ has the least bandgap, which is 1.95 eV (Fig. 7c).[92] In addition to its impact on the bandgap, the Ge atom effectively protects the internal Sn atoms from oxidation by substituting Sn atoms and filling the bandgap (Fig. 7d).[93]

Besides Ge, doping with other elements can also improve the bandgap and structure of TPSCs. For instance, due to the smaller ionic radii of Sr (118 pm) and Ca (100 pm), SnSr and SnCa PSCs exhibit higher tolerance factors (t) and smaller mobilities (μ), which help to tune the bandgap of TPSCs to an appropriate range (Fig. 7e).[94] Doping with Bi can enhance the conductivity of Sn-based perovskite materials. This is because Bi doping can reduce the bandgap of perovskites (0.8–1.3 eV), thereby increasing the carrier density and affecting conductivity (Fig. 7f).[95] Hasegawa *et al.* pointed out that the empty 6p orbital of Bi^{3+} has a lower energy level than the empty 5p orbital of Sn^{2+}. Therefore, the lower edge of the conduction band shifts downward with the increase in Bi content, leading to a smaller bandgap. In addition, doping with elements such as Sr and Sb at the B-site can also improve the thin-film structure and Sn-based perovskite materials' stability.[95] Adjokatse *et al.* noted that Sr can enhance the morphology of perovskite films, passivate surface defects, and reduce pinholes in the films, thus raising PSCs' structural stability (Fig. 7g and h).[96] Moreover, In and Mn have been used to dope the B-site in TPSCs. In $CsSn_{0.9}In_{0.067}Cl_3$, the closed-shell In^{3+} generates B-site

 This journal is © The Royal Society of Chemistry 2025

Published on 01 August 2025. Downloaded on 1/24/2026 5:38:31 AM.

vacancies (In^{3+}–Cl^-), which accelerates carrier recombination while minimizing energy loss. In $CsSn_{0.9}Mn_{0.1}Cl_3$, the half-filled d^5 structure of Mn^{2+} introduces energy levels in the middle of the bandgap. Although the contribution of these levels to strong interband absorption is negligible, the introduction of Mn^{2+} promotes carrier mobility (Fig. 7i).[97]

3.1.1.3 X-site anion. In the perovskite octahedral structure, the X-site anions are located at the six face-centered positions of the octahedron, connected to the B-site cations *via* coordination bonds, forming a stable octahedral structure. The X-site anions are primarily halogens (such as Cl^-, Br^-, and I^-). The type and proportion of X-site anions significantly influence the properties of perovskite materials, including the band structure, thin-film morphology, and crystallization. Therefore, the selection and regulation of X-site anions are crucial in the manufacturing process of TPSCs.[98]

The incorporation of Cl^- ions can also affect the thin-film morphology of perovskites. Wang *et al.* pointed out that the initial mixing of Cl^- and I^- leads to the formation of novel nucleation sites, which facilitates perovskite crystals' growth and the uniformity of the thin film.[99] The addition of Cl^- alters the lattice constant, further influencing the structural shifts within the ammonium chains or the ordering–disordering transitions of the ammonium chains along their length in the phase transition procedure. This increases electrical conductivity and promotes charge transport (Fig. 8a).[99] Meanwhile, when trihalides (Cl^-, Br^-, and I^-) substitute for the X-site, the incorporation of Cl^- can increase the bandgap of perovskites, enhancing the Sn-based perovskites' stability.[100]

Moreover, the doping of Br^- can improve the bandgap and Sn-based perovskites' thin film. Sabba *et al.* indicated that the substitution of I^- with Br^- changes the crystal structure from tetragonal to cubic, thereby increasing the bandgap of perovskites. Although this reduces light absorption, it has a beneficial influence on the open circuit voltage (Fig. 8b and c).[41] Additionally, Br^- enhances the crystallinity of perovskite thin films and increases grain size, thereby reducing pinholes in the film. High-quality films can lower defect density, thereby suppressing

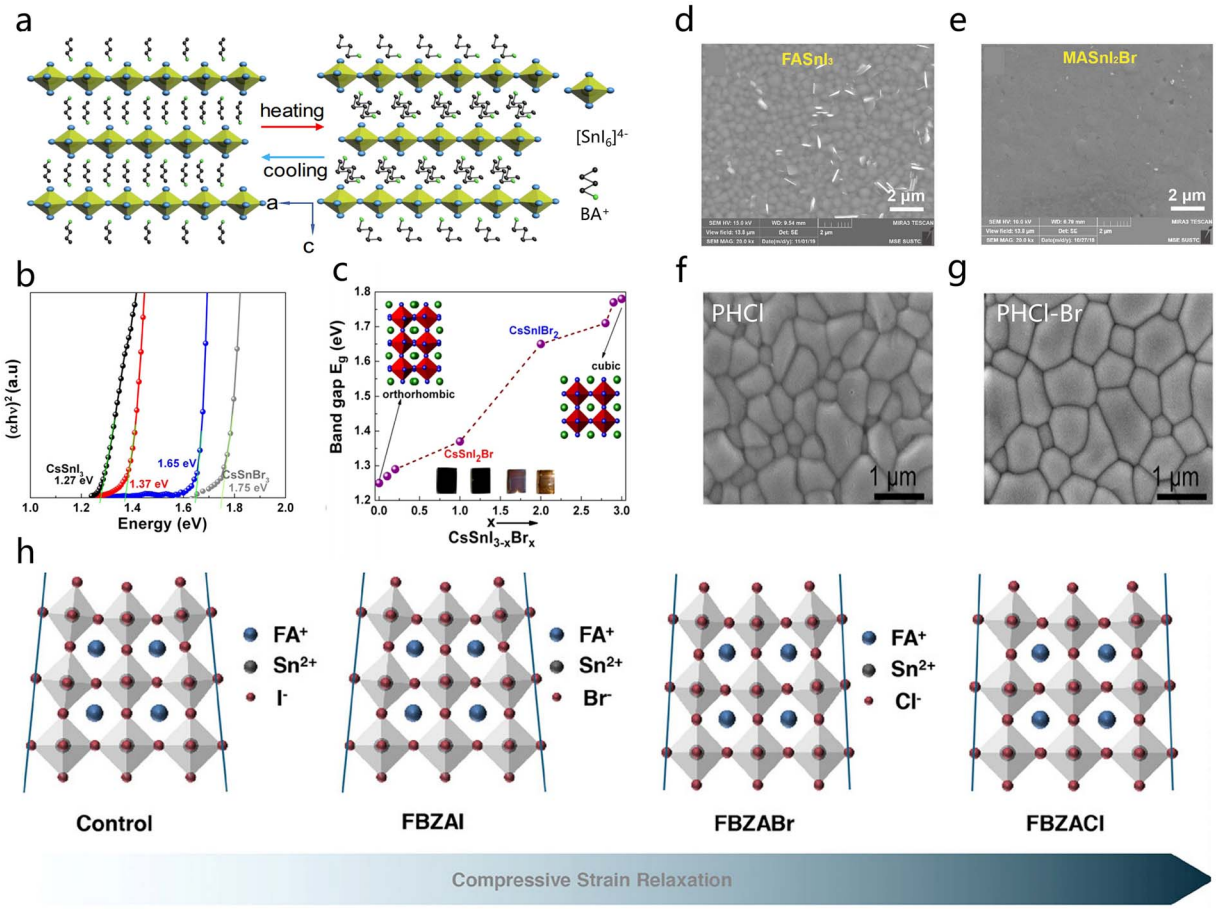

Fig. 8 (a) Effect of Cl^- induces a transition from an ordered to a disordered state in $(BA)_2SnI_{4-x}Cl_x$.[99] Copyright 2019, Wiley-VCH GmbH. (b) Absorption spectroscopy of the films which show a blue shift upon inclusion of Br^- in the crystal structure of $CsSnI_3$.[41] Copyright 2015, the American Chemical Society. (c) Variation in the bandgap of Sn perovskites with Br^- concentration. The inset shows photographs of the samples: $CsSnI_3$, $CsSnI_2Br$, $CsSnIBr_2$, and $CsSnBr_3$ from left to right.[41] Copyright 2015, the American Chemical Society. (d and e) Top-view SEM images of $FASnI_3$ and $MASnI_2Br$ perovskite thin films.[101] Copyright 2020, Wiley-VCH GmbH. (f and g) Top-view SEM images of PHClBr and PHCl.[101] Copyright 2020, Wiley-VCH GmbH. (h) Schematic of the residual strain variation in the control film and the FBZAX (I^-, Br^-, Cl^-) modified film.[32] Copyright 2020, Elsevier.

Published on 01 August 2025. Downloaded on 1/24/2026 5:38:31 AM.

non-radiative recombination and improving photovoltaic PCE (Fig. 8d and e).[101] At the same time, the introduction of Br^- can also regulate crystallization, promoting the formation of smaller grains, thereby improving crystal uniformity (Fig. 8f and g).[32] Furthermore, Br^- can modulate the energy levels of TPSCs, improving charge recombination and dielectric relaxation effects.[100] In addition to these common X-site anions, there are some rare X-site anions such as pseudohalides and super halogens, which also play important roles in suppressing non-radiative recombination in perovskites and reducing the defect density. For example, Gu *et al.* proposed an interhalogen compound, IBr, which can not only replenish the missing iodide ions but also exert the effects of Br^- ions. IBr inhibits film aging (with almost no change in color).[102] Recent studies have demonstrated that incorporating 4-fluorobenzylhalideammonium salts (FBZAX, where $X = I^-$, Br^-, and Cl^-) into perovskite precursors can effectively relieve internal dislocations in Sn-based perovskite films by modulating the strain within the films. This approach enhances carrier transport, reduces defect density, and prolongs carrier lifetime. These improvements have led to a PCE of 14.1% for TPSCs, with outstanding operational stability (no degradation within 150 hours) (Fig. 8h).[103]

3.1.2 Dimensional engineering

3.1.2.1 Three-dimensional structure. As previously discussed, small A-site cations perform a critical function in stabilizing the three-dimensional (3D) architecture of Sn-based perovskites. The prototypical ABX_3 structure—characterized by its corner-sharing octahedral framework—serves as the fundamental building block for these materials, with its structural integrity directly underpinning their favorable electronic transport PCE. Building on this foundation, the following discussion will contrast 'solid' and 'hollow' 3D perovskite variants, emphasizing their structural distinctions and associated property implications.[104]

Research on Sn-based perovskites reveals that the tetragonal (TETP) phase of $MASnBr_3$ exhibits parallel-aligned C–N bonds (Fig. 9a and b), optimizing lattice parameters compared to its

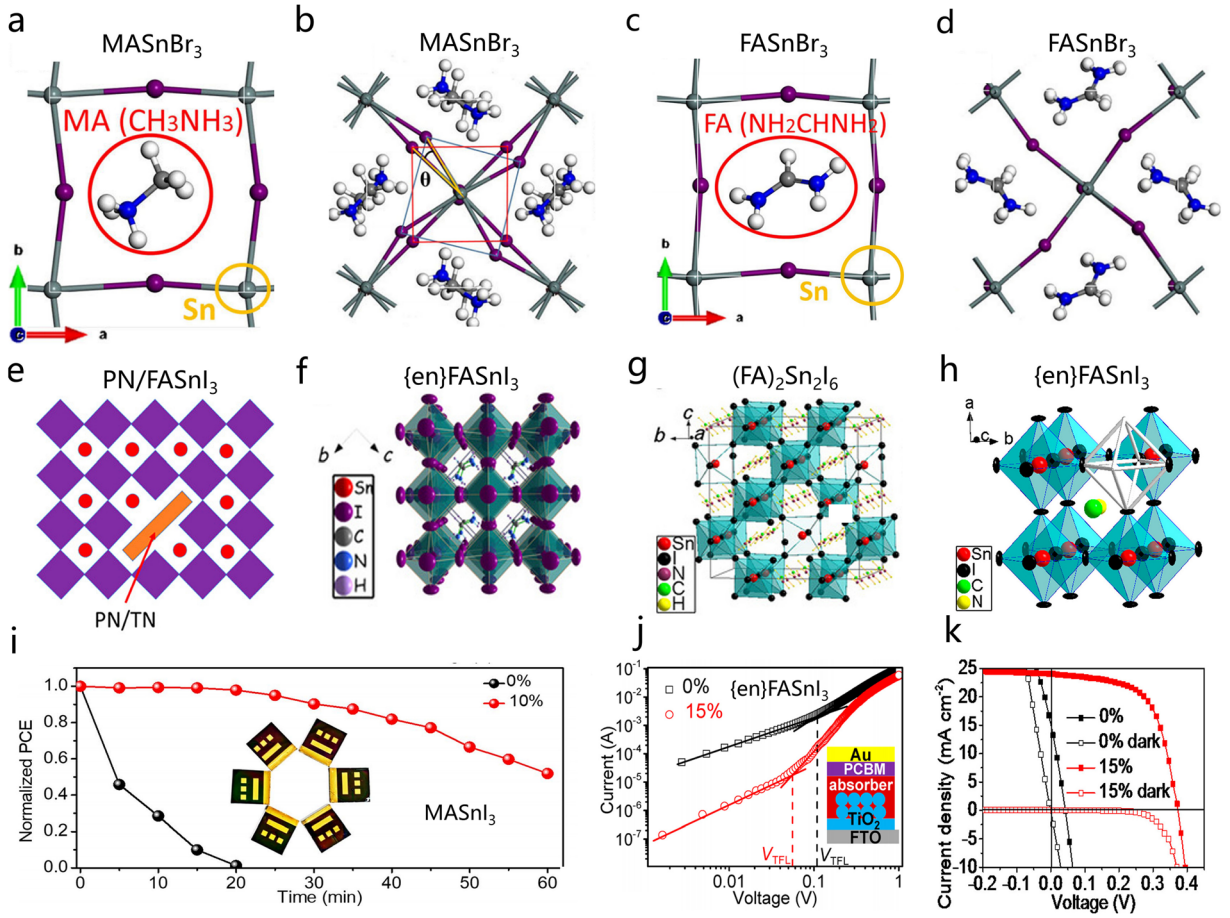

Fig. 9 (a) Cubic structure and (b) TETP structure of $MASnBr_3$. (c) Cubic structure and (d) tetragonal structure of $FASnBr_3$.[105] Copyright 2016, Springer Nature. (e) 3D hollow $FASnI_3$ with PN or TN.[106] Copyright 2018, the American Chemical Society. (f) Monomer battery and crystal structure of the $\{en\}FASnI_3$ perovskite absorber.[83] Copyright 2017, AAAS. (g) Schematic of the $2 \times 2 \times 2$ supermonomer of $(FA)_2Sn_2I_6$, depicting a hollow perovskite model with two Sn^{2+} vacancies $[(FA)_{16}Sn_{14}I_{44}]$.[83] Copyright 2017, AAAS. (h) Curve of SnI_2 vacancies in $\{en\}FASnI_3$ with increasing bandgap and decreasing bandwidth.[86] Copyright 2017, the American Chemical Society. (i) Unencapsulated $MASnI_3$ solar cells undergoing ageing tests in air under constant AM 1.5G light conditions.[83] Copyright 2017, AAAS. (j and k) Dark I–V curve of pure electronic devices and J–V curves of solar cells using $MASnI_3$ perovskite absorber under dark and AM 1.5G illumination.[86] Copyright 2017, the American Chemical Society.

 This journal is © The Royal Society of Chemistry 2025

Published on 01 August 2025. Downloaded on 1/24/2026 5:38:31 AM.

cubic counterpart. Similarly, the TETP phase of $FASnBr_3$ demonstrates a larger lattice parameter than the cubic phase, as reported in Fig. 9c and d).[105] Ferrara *et al.* demonstrated that substituting formamidinium (FA) for methylammonium (MA) in $SnBr_3$-based perovskites generates cubic-symmetric solid solutions, wherein increasing the FA content induces a linear reduction in the cubic lattice parameter a (from 1.9–2.4 eV) and corresponding bandgap narrowing.[80] Hollow perovskites—a subclass of hybrid 3D architectures—are engineered by incorporating larger diammonium cations at the A-site. Unlike conventional solid 3D perovskites, these structures retain the 3D connectivity while introducing BX_2 vacancies, which modulate the B–X orbital overlap and spin–orbit coupling to enhance the photovoltaic performance and stability. For instance, Ke *et al.* introduced propane diamine (PN) and triethylene diamine (TN) at the A-site, yielding hollow perovskites without dimensional collapse. This approach reduced the bandgap (Fig. 9e) and doubled PCE to 5.53%.[106] In parallel work, co-doping with ethylenediamine (en) and FA in Sn perovskites generated hollow structures with Schottky defects, widening the bandgap (Fig. 9f and g) but suppressing Sn^{2+} oxidation. This trade-off resulted in exceptional air stability, retaining 96% of the initial PCE over 1000 hours (Fig. 9i).[83] Further structural tailoring was achieved by integrating en and MA into the $MASnI_3$ lattice, forming hollow perovskites with single-chain en incorporation (Fig. 9h). The resulting reduction in electronic trap density and enhanced carrier mobility enabled a record PCE of 7.14% (Fig. 9j and k).[86]

3.1.2.2 Quasi-two-dimensional structures. It is well known that two-dimensional structures are formed by inserting large cations into the structural layers of three-dimensional perovskites, creating a layered structure. When organic amines are inserted into three-dimensional perovskites, as the quantity of inorganic perovskite layers, n, approaches infinity, the organic amine layers will be neglected, and the structure approaches that of three-dimensional perovskites; this structure is referred to as a "quasi-two-dimensional structure." Quasi-two-dimensional structures combine the advantages of both two-dimensional and three-dimensional structures, significantly enhancing the stability and photoelectric PCE of the device. Phenylethylamine (PEA) was the initial one to be utilised for the preparation of quasi-two-dimensional perovskites.[29] However, due to issues such as reduced light absorption range, *n*-butylamine (*n*-BA) has become the most commonly used organic amine.[87] In addition to the aforementioned monoamines, polyamine cation polymers (such as polyetherimide (PEI)) have also been employed as intercalants.[107] Quasi-two-dimensional structures can be broadly classified into DJ (Dion–Jacobson) phase, RP (Ruddlesden–Popper) phase, and ACI (Alternating Cation Interlayer) phase. Among these, the RP and DJ phases are commonly found in perovskites, while the ACI phase is not frequently observed in Sn-based perovskites. The following sections will introduce the RP and DJ phases in detail.[78]

In the RP phase, long-chain monovalent organic cations occupy the interlayer gaps, moving a half-octahedron between adjacent 2D perovskite slabs. The interlayer spacing is typically enlarged due to the bilayer configuration of paired monovalent cations. The RP phase demonstrates advantages in suppressing self-doping effects and ion migration, thereby enhancing the moisture and air stability of perovskite structures.[108] Xu *et al.* incorporated three bulky organic cations, namely, 5-ammoniumvaleric acid (AVA), phenylethylammonium (PEA), and butylammonium (BA) into $FASnI_3$ with NH_4Cl additive assistance, achieving highly vertically oriented RP-phase Sn perovskites that facilitated charge carrier transport. Notably, AVA's bifunctional carboxyl and amino groups effectively suppressed low-dimensional phases with small n-values, and a PCE of 8.71% was achieved under the condition of AVA incorporation (Fig. 10a–c).[109] Concurrently, Li *et al.* employed alkylammonium interval cations with different chain lengths (dodecylamine (DA), octylamine (OA), and butylamine (BA)) to synthesize RP-phase Sn-based perovskites. Their study revealed that longer alkyl chains induced disordered phase distribution and inferior orientation (Fig. 10d–f), with BA-based devices achieving a champion PCE of 4.04%.[81]

Different from the RP phase, the Dion–Jacobson (DJ)-phase perovskites exhibit non-shifted octahedral layers, creating well-aligned lamellar architectures. The monolayer arrangement of divalent organic cations in DJ phases enables a significantly reduced interlayer spacing compared to RP counterparts, effectively weakening quantum confinement. These characteristics confer enhanced structural stability and superior charge transport properties. Chen *et al.* synthesized (4AMP) $(FA)_{n-1}Sn_nI_{3n+1}$ DJ-phase Sn perovskites using 4-(aminomethyl)piperidinium (AMP) as organic spacers (Fig. 10g). Despite improved structural stability through strong hydrogen bonding between AMP and perovskite layers, the PCE remained at 4.22% (Fig. 10h).[110] Ju *et al.* subsequently enhanced this system by introducing π-conjugated diammonium cations (π-DAMs: 2,9-pentacenediyldimethanammonium (PMA), anthra[2,3-*b*:7,8-*b*′] bis(5-thiopheneylmethanammonium) (ATMA)), 2,6-anthracenediyldimethanammonium (AMA), 2,10-hexacenediyldimethanammonium (HMA), and 2,8-tetracenediyldimethanammonium (TMA). AMA-modified devices demonstrated optimal performance through type-II band alignment, leveraging π-DAMs' unique HOMO and LUMO electronic configurations to promote the segregation of electron–hole pairs and boost carrier mobility.[111] Further advancements by Li *et al.* employed 1,4-butanediamine (BEA) ligands to construct DJ-phase Sn perovskites. The compressed interlayer distance (Fig. 10i) and narrow quantum well potential distribution mitigated quantum confinement effects, suppressed Sn^{2+} oxidation, and improved carrier diffusion mobility, achieving a record PCE of 6.43%.[30]

3.1.2.3 Hybrid forms of 2D–3D structures. When the number of inorganic layers is $n > 5$ in quasi-two-dimensional perovskites, a 2D–3D hybrid heterojunction structure is formed.[112] This structure restricts the transmission of photons at the interface, thereby improving light absorption PCE and electron transport PCE. Hybrid heterojunctions are divided into planar heterojunctions and bulk heterojunctions.

For planar heterojunctions, Shao *et al.* added 8% PEA to a three-dimensional perovskite, forming a 2D–3D planar heterojunction with a PEA content much lower than

Published on 01 August 2025. Downloaded on 1/24/2026 5:38:31 AM.

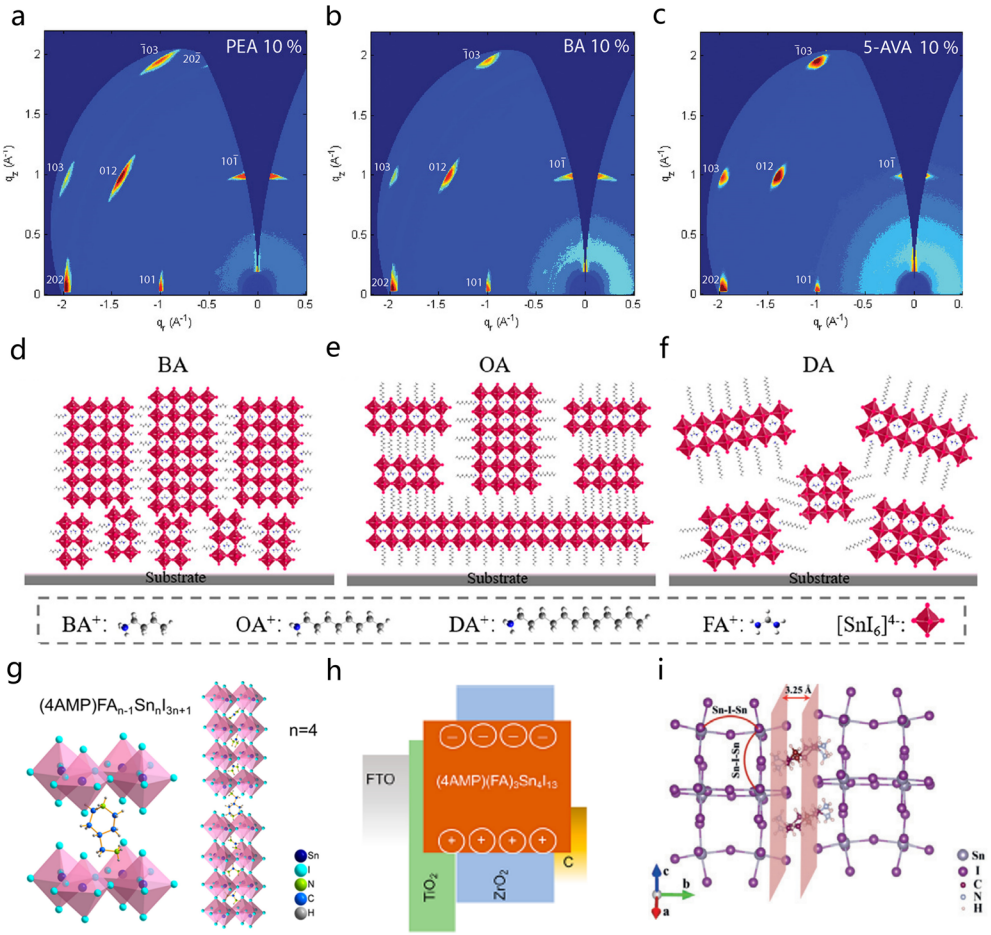

Fig. 10 GIWAXS of (a) $PEA_2FA_{n-1}Sn_nI_{3n+1}$ with 10% NH_4Cl addition, (b) $BA_2FA_{n-1}Sn_nI_{3n+1}$ with 10% NH_4Cl addition, and (c) $AVA_2FA_{n-1}Sn_nI_{3n+1}$ with 10% NH_4Cl addition.[109] Copyright 2019, Wiley-VCH GmbH. Schematic of the crystal orientation, size and phase distribution of two-dimensional perovskite thin films: (d) BA, (e) OA, and (f) DA.[81] Copyright 2020, the American Chemical Society. (g) Schematic of the crystal structure of DJ-phase Sn-based halide perovskites $(4AMP)(FA)_{n-1}Sn_nI_{3n+1}$ ($n = 4$).[110] Copyright 2019, the American Chemical Society. (h) Energy-level diagram of HTML-free PSC based on DJ Sn(II).[110] Copyright 2019, the American Chemical Society. (i) Illustration of the distance between the diffraction planes of $(BEA)FA_{n-1}Sn_nI_{3n+1}$.[30] Copyright 2020, Wiley-VCH GmbH.

conventional levels (Fig. 11a). However, the 2D–3D film (8%) exhibited Bragg spots located around the same ring, indicating that the film had a strong textured morphology, with grains having a preferred orientation relative to the substrate. The ordered expansion and arrangement of crystal planes enhanced the stability and completeness of the perovskite structure (Fig. 11b and c).[85] Liao *et al.* demonstrated that incorporating 20 mol% phenethylammonium (PEA) as a cationic surfactant facilitates the vertically aligned growth of low-dimensional $FASnI_3$ films on NiO substrates. This approach leverages thermodynamic favorability to enhance crystallographic orientation and interfacial compatibility, which helps to inhibit tin vacancies' formation, thereby reducing background carriers and further improving air stability (100 h without attenuation).[112] In addition, Shao *et al.* added another organic molecule, EA (ethamine), to the precursor, with the best results obtained at 8% EA, forming a planar heterojunction film with better crystallinity and stronger orientation.[31] Furthermore, Sandhu *et al.* combined the dimension-reducing effect of PEAI with the intergrain bridging function of $EDAI_2$ to formulate an optimal binary-additive ratio of 8 : 1 mol% ($PEAI : EDAI_2$). This strategy yields compact, pin-hole-free perovskite films featuring superior crystallinity and preferred orientation, an exceptionally low background carrier density, and markedly reduced trap-state density, thereby suppressing recombination losses. The reduced dimensionality together with the favorable layer stacking enhances interlayer coupling and facilitates efficient interfacial charge transfer. Consequently, the TPSCs deliver a promising PCE of 8.47% and exhibit outstanding stability (devices retain their performance for five days under ambient conditions without any additional encapsulation).[113]

A bulk heterojunction is formed through mixing donor/acceptor substances, with the resulting active layer positioned in the middle of two electrodes. Ran *et al.* evaporated PEAI molecules onto the top of an FAI film to form a PEAI/FAI mixture. After evaporating SnI_2, a new-type 2D–3D (PEA and FA) SnI_3 bulk heterojunction film can be achieved. Evaporation under vacuum conditions can effectively prevent the oxidation

 This journal is © The Royal Society of Chemistry 2025

Published on 01 August 2025. Downloaded on 1/24/2026 5:38:31 AM.

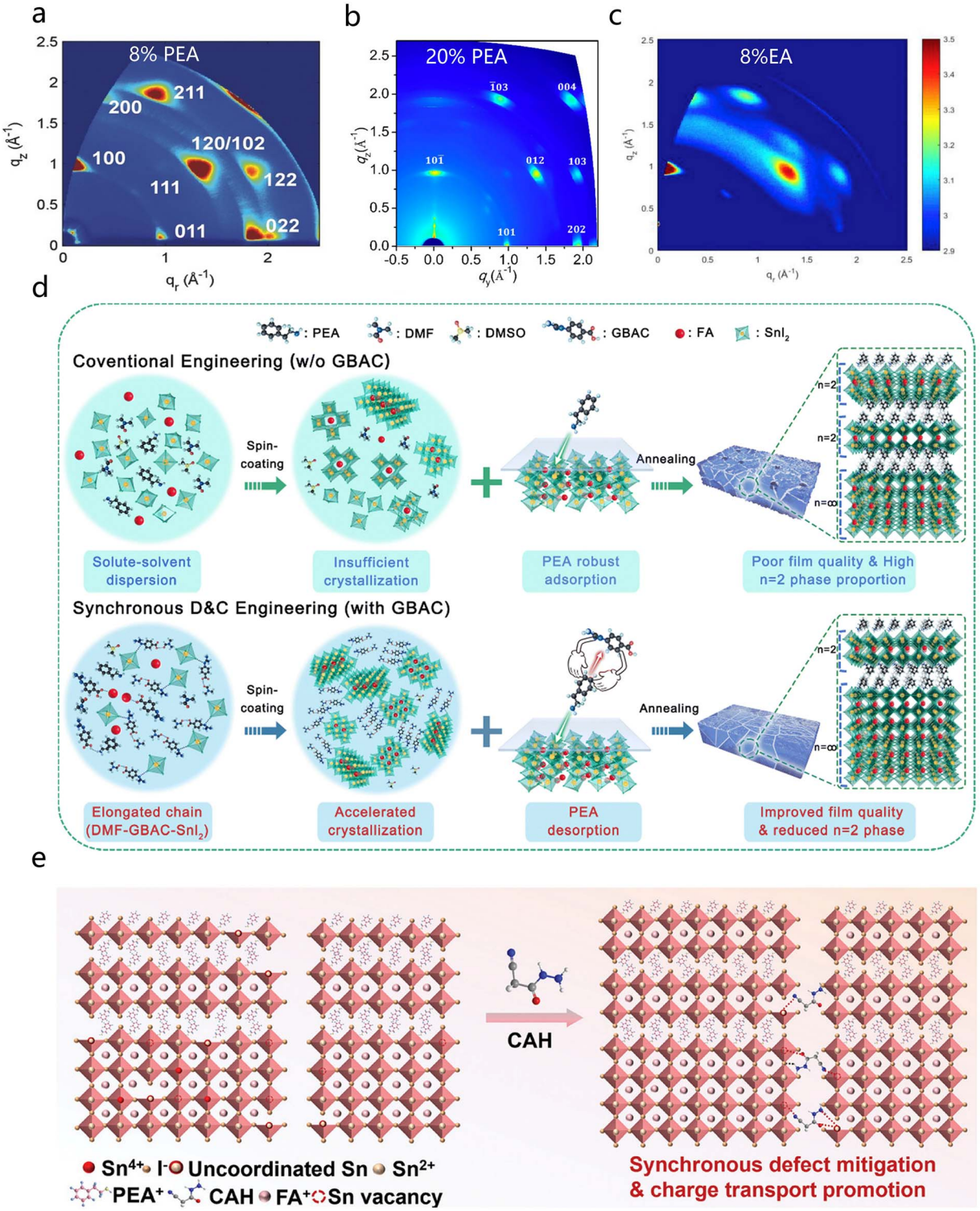

Fig. 11 GIWAXS of (a) 8% PEA, (b) 20% PEA, and (c) 8% EA.[85] Copyright 2017, Wiley-VCH GmbH. (d) Schematic of the action mechanism of GBAC.[115] Copyright 2025, the Royal Society of Chemistry. (e) Schematic of the interaction between CAH and Sn perovskite.[117] Copyright 2025, Wiley-VCH GmbH.

of Sn^{2+}, and hence, this thin-layer configuration can triumphantly boost the performance and stability of PSC devices, achieving a PCE of 6.98%.[114]

In addition, Jokar *et al.* added a trace amount of $EDAI_2$ (ethylenediamine diodide) to $FASnI_3$ in order to regulate the film morphology, forming a bulk heterojunction. This resulted

Published on 01 August 2025. Downloaded on 1/24/2026 5:38:31 AM.

in a tightly packed and homogeneous surface free of pinholes compared to the original $FASnI_3$, thereby passivating surface defects, suppressing Sn^{2+} oxidation, and improving PCE and stability. A fresh $FASnI_3$ device with 1% $EDAI_2$ exhibited a PCE of 6–7% on the initial day of fabrication, while the PCE continuously raised during storage for over 1400 h, reaching a PCE of 8.9%. Moreover, it maintained a PCE of 8.9% after 2000 h of storage.[88]

For TPSCs with 2D–3D heterostructures, the inherent poor carrier transport led by multiple quantum wells as well as the unstable crystal growth induced by incorporating organic interval cations have reduced device PCE. In recent studies, Kang *et al.* introduced 4-guanidinium benzoate hydrochloride (GBAC) between the A-site large cation PEA and the perovskite, triggering an unexpected desorption effect that promotes the $n = 2$ phase Sn perovskite transit to the $n = \infty$ phase Sn perovskite. Additionally, the introduction of GBAC can form extended organic–inorganic mixed chains, thereby improving the crystallization process of the film through boosting nucleation and growth rates. Based on these effects, TPSCs achieved a champion PCE of 15.02% and excellent long-term stability (maintaining 87% of the starting performance after 4000 hours of operation at the maximum power point) (Fig. 11d).[115] Furthermore, Feng *et al.* used 2-(thiophen-3-yl)ethan-1-aminium (3-TEA), which is a thiophene-based cation, as a spacer to generate a new 2D perovskite in TPSCs. Indicated by theoretical arithmetic, 3-TEA can achieve the densest crystal arrangement of $[SnI_6]^{4-}$, thereby obtaining the smallest hole effective mass as well as formation energy in the 2D phase. This effect greatly increases the device's PCE as well as stability through facilitating higher efficient carrier transfer within the 2D phase (PCE of 14.16%, retaining about 90% of the starting PCE for 2000 hours without encapsulation in a glove box).[116] In addition, it has been demonstrated that small molecules with multiple functional groups, such as cyanoacetohydrazide (CAH), can mitigate defects and enhance charge transport in 2D–3D TPSCs. The results indicated that the carbonyl, amine, and cyano groups in CAH produce a synergistic coordination effect by forming strong chemical bonds with Sn^{2+} ions, effectively regulating the crystallization process in perovskite layers. This results in a high-performance Sn perovskite film with enhanced crystallinity, decreased defect concentration, as well as modulated 2D–3D phase distribution (Fig. 11e).[117] The optimized 2D–3D TPSCs reached a PCE of 15.06%, which is one of the greatest PCEs for 2D–3D TPSCs. Moreover, the optimized devices exhibited excellent stability, retaining 95% of their starting performance after 2000 hours of storage in a nitrogen atmosphere.

All the key information on the structural engineering of Sn-based PSCs in this section is summarized in Table 1.

3.2 Crystallization regulation

3.2.1 Antisolvent. An antisolvent, relative to a specified solution system, refers to a solvent which is soluble in the solvent but is immiscible with the solute. Antisolvents typically possess properties such as low boiling point, non-polarity, and inability to dissolve perovskites. These properties enable the antisolvent to effectively mix with the primary solvent while reducing perovskite's solubility in the mixture, accelerating the triggered crystallization process's rate. Researchers have investigated the influence of temperature, co-solvents, and the properties of the antisolvent itself on antisolvent-mediated crystallization.[130]

The number of pinholes in perovskite thin layers varies at different temperatures. To study the influence of temperature on the antisolvent action, Liu *et al.* introduced a "hot antisolvent" by preheating the antisolvent during the spin-coating process to improve film coverage and eliminate the large pinholes observed when using antisolvents at room temperature (Fig. 12a and b). Liu *et al.* selected 65 °C as the optimal temperature for introducing a chlorobenzene (Ph-Cl) antisolvent, maximizing the nucleation rate, achieving near 100% film coverage, and fabricating TPSCs with PCEs exceeding 7%.[131] The primary solvent in the precursor solution is extracted by the antisolvent bath *via* a miscibility process, where the extraction rate is strongly dependent on the miscibility between the solvents, and co-solvents can promote this miscibility. To explore the impact of co-solvents on crystallization, Fujihara *et al.* combined different antisolvents (DMSO, toluene, and hexane as a good solvent, a miscible antisolvent, and an immiscible antisolvent, respectively) with the precursor solvent (Fig. 12c). Fujihara *et al.* obtained perovskite films with the fastest nucleation rate and highest coverage under moderate co-solvent mixture LT-Mix conditions, enhancing Sn perovskite solar cells' stability (solar cell lifetime exceeding 200 h below AM1.5, 100 mW cm^{-2} conditions).[24] Furthermore, the properties of the antisolvent itself (*e.g.*, boiling point) also affect crystallization. Liu *et al.* used dimethyl sulfoxide (DMSO) and *N*,*N*-dimethylformamide (DMF) as a blended solvent, along with Sn fluoride (SnF_2), in order to prepare the perovskite precursor. By comparing toluene (TL), chlorobenzene (CB), as well as diethyl ether (DE) as antisolvents, they researched the effect of the solvent's properties on crystallization. The boiling point of the antisolvent determines the crystal growth time. The higher the boiling point of the antisolvent, the longer the crystal growth duration in the thermal annealing procedure, the faster the nucleation rate, and the denser and more uniform the film. Comparing the three antisolvents, the $FA_{0.75}MA_{0.25}SnI_3$ film with DE droplets had many pinholes, smaller in size than those with TL droplets, but more numerous. CB, with the highest boiling point, resulted in an even film surface with complete coverage and distinct grain characteristics. The device treated with CB reached a maximum PCE of 9.06% as well as retained good stability under 1.5G 100 mW cm^{-2} illumination conditions (maintaining 75% of the original PCE after 30 days).[27]

In the latest research, Su *et al.* developed an environmentally friendly antisolvent, acetic acid (HAc), to replace the traditional toxic antisolvent chlorobenzene (CB) for modifying the crystal growth and nucleation processes of Sn-based perovskite films. This work involves a more realistic perovskite nucleation and crystallization theory (salt precipitation crystallization). HAc forms hydrogen bonds with the precursor solvent, weakening the solvation effect of DMSO on SnI_2. Additionally, the

 This journal is © The Royal Society of Chemistry 2025

Published on 01 August 2025. Downloaded on 1/24/2026 5:38:31 AM.

Table 1 Summary of the doped substances and their performances in the structural engineering of Sn-based PSCs

Matrix	Doped site	V_{OC} (V)	J_{SC} (mA cm^{-2})	FF (%)	PCE (%)	Shelf stability	Ref.
A-site cation							
$MASnI_3$	FA	0.61	21.20	62.70	8.12	—	118
$FASnI_3$	Cs	0.44	20.70	66.70	6.08	Retain 90% of the initial PCE after 2000 h in N_2 without encapsulation	79
$FASnI_3$	en	0.48	22.54	65.96	7.14	—	83
$MASnI_3$	BA	0.23	23.20	45.20	2.5	—	87
$FASnI_3$	BA, EDA	0.58	21.30	71.80	8.90	Retain 141% of the initial PCE after 1462 h in N_2 with encapsulation	88
$FASnI_3$	PEA	0.53	24.10	71.00	9.00	Retain 59% of the initial PCE after 76 h in air without encapsulation	85
$FASnI_3$	HA	0.38	14.10	49.00	2.60	Retain 90% of the initial PCE after 5 d in N_2 with encapsulation	119
$FASnI_3$	PEA	0.45	24.87	63.00	7.05	—	120
$(BA_{0.5}PEA_{0.5})_2FA_3Sn_4I_{13}$	BA, PEA	0.60	21.82	66.73	8.82	—	29
$FASnI_3$	GA	0.62	21.20	72.90	9.60	—	82
$FASnI_3$	PPA	0.56	23.34	73.50	9.61	Retain 92% of the initial PCE after 1440 h in N_2 without encapsulation	121
$FASnI_3$	4AMP	0.64	14.90	44.30	4.22	—	110
$FASnI_3$	EA	0.51	23.75	70.00	8.40	Retain the initial PCE after 700 s in N_2 with encapsulation	31
$FASnI_3$	Cs	0.99	23.07	74.83	17.13	Retain 93.3% of its initial PCE 6000 h in N_2 without encapsulation	40
B-site cation							
$RbSnI_3$	Ge	—	—	—	—	—	91
$MASnI_3$	Bi	—	—	—	—	—	95
$MASnI_3$	Sr/Ca	—	—	—	—	—	94
PEA_2SnI_3	Ge	—	—	—	—	—	122
$MASnI_3$	Ge	—	—	—	—	—	92
$FA_{0.75}MA_{0.25}SnI_3$	Ge	0.43	20.30	60.00	4.79	—	123
$MASnI_3$	In	—	—	—	—	—	124
$CsSn_{0.5}Ge_{0.5}I_3$	Ge	0.63	18.61	60.60	7.11	—	125
$CsSnCl_3$	In/Mn	—	—	—	—	—	97
$FASnI_3$	Sr	—	—	—	—	—	96
$CsSnCl_3$	Ge	0.65	11.80	64.00	4.90	—	93
X-site anion							
$CsSnI_3$	Br	0.22	24.16	33.00	1.76	—	41
$MASnIBr_2$	Cl	0.38	14.00	57.30	3.10	Retain 90% of the initial PCE after 2000 h in N_2 with encapsulation	100
$FASnI_3$	Br	0.41	19.80	66.90	5.50	—	126
$MA_{0.25}FA_{0.75}SnI_3$	Br	0.60	22.48	69.00	9.31	—	101
$FASnI_3$	BF_4	0.19	20.20	34.00	1.30	—	127
$FASnI_3$	Cl/Br	0.81	22.42	—	13.40	—	32
$FASnI_3$	Br	0.80	23.12	76.71	14.13	Retain 87% of the initial PCE after 3 years in N_2 with encapsulation	103
$(BA)_2SnI_{4-x}Cl_x$	Cl	—	—	—	—	—	99
3D structure							
$FASnI_3$	PN/TN	0.44	22.15	60.67	5.85	—	106
$EA_{0.1}(FA_{0.75}MA_{0.25})_{0.9}SnI_3$	EA	0.46	14.34	64.00	5.41	—	128

Published on 01 August 2025. Downloaded on 1/24/2026 5:38:31 AM.

Table 1 (*Contd.*)

Matrix	Doped site	V_{OC} (V)	J_{SC} (mA cm^{-2})	FF (%)	PCE (%)	Shelf stability	Ref.
Quasi-two-dimensional structure							
$MASnI_3$	BA	0.23	23.20	45.20	2.50	Retain over 90% of the initial PCE after 1 month in air with encapsulation	87
$BA_2MA_3Sn_4I_{13}$	MAAc	0.38	21.87	48.30	4.03	Retain the initial PCE after 94 d in N_2 without encapsulation	129
$FASnI_3$	5AVA	0.61	21.00	68.00	8.71	Retain the initial PCE over 400 h in N_2 without encapsulation	109
$FASnI_3$	GBAC	0.88	23.20	73.72	15.02	—	115
$(BA_{0.5}PEA_{0.5})_2FA_3Sn_4I_{13}$	PEA	0.60	21.82	66.73	8.82	Retain 60% of the initial PCE after 24 d in N_2 without encapsulation	29
$A_2(FA)_{n-1}Sn_nI_{3n+1}$	OA	—	—	—	3.03	Retain 80% of the initial PCE after 14 d in N_2 without encapsulation	81
(π-DAM)$(FA)_{n-1}Sn_nX_{3n+1}$	π-DAM	—	—	—	—	—	111
$(BEA)FA_2Sn_3I_{10}$	BEA	0.62	18.85	55.00	6.43	Retain 90% of the initial PCE after 1000 h in N_2 without encapsulation	30
2D–3D tin PSCs							
$FASnI_3$	CAH	0.88	23.74	72.10	15.06	Retain 95% of the initial PCE after 2000 h in N_2 without encapsulation	117
$FASnI_3$	3-TEA	0.89	22.88	67.00	14.16	Retain 90% of the initial PCE after 1960 h in N_2 without encapsulation	116
$FASnI_3$	$PEAI/EDAI_2$	0.63	19.32	69.43	8.47	Retain 85% of the initial PCE after 120 h in dry room environment without encapsulation	113

substantial residual HAc on the precursor film helps to retard the crystal growth procedure, indicating that HAc, an environmentally friendly antisolvent, can broaden the processing window for Sn-based perovskites, enabling high-quality and large-scale production. After treatment with HAc, the device PCE reached as large as 12.78%, which is the greatest PCE reported for Sn-based perovskite devices fabricated using green antisolvents (Fig. 12d).[132] Studies have also shown that the introduction of 1,2-dichlorobenzene (DCB) as an antisolvent can relieve compressive strain and suppress non-radiative recombination in Sn perovskite films, benefiting efficient interfacial carrier transfer. Moreover, since grain boundaries are two-dimensionally extended defects and one of the sources of non-radiative recombination, DCB can suppress non-radiative recombination by increasing the average grain size. As a result, devices employing DCB achieved an PCE of 14.85% (Fig. 12e and f).[66]

3.2.2 Fast nucleation

3.2.2.1 Lower the nucleation energy barrier. The nucleation energy barrier refers to the energy barrier that must be surmounted to form a nucleus containing a new phase in a supersaturated parent phase. A lower nucleation energy barrier makes the nucleation process easier and the crystallization rate faster. By controlling the nucleation energy barrier, precise control of the crystallization rate can be achieved, resulting in ideal perovskite thin films. The following sections introduce strategies for reducing the nucleation energy barrier from the perspectives of pre-nucleation clusters, surface energy, and zeta potential.[133]

Meng *et al.* introduced piperazine dihydriodide into the $FASnI_3$ solution, forming pre-nucleation cluster (PNC) intermediate phases (Fig. 13a), lowering the energy barrier (Fig. 13b), decreasing defects in the perovskite layer, and increasing the PCE to 11.93%.[33] Research indicates that $FASnI_3$ nucleation begins at the solution–air surface. Meng *et al.* introduced pentafluorophen-oxyethylammonium iodide (FOEI), reducing solution–air surface's energy. FOEI and SnI_6^{4-} interact, reducing the total free energy of nucleation and increasing the nucleation rate by 20 times (Fig. 13c). The device ultimately achieved a PCE of 10.16%.[134] Furthermore, Wang *et al.* based on the Derjaguin–Landau–Verwey–Overbeek (DLVO) theory, found that after adding 3-aminopyridine dihydroiodide ($APDI_2$) to the precursor solution, perovskite colloidal particles' zeta potential changed sharply from −4.22 mV to 0.69 mV (Fig. 13d), thereby controllably reducing the total interaction potential energy between the colloidal particles and $APDI_2$, which increased the coagulation probability of the colloidal particles and reduced the critical nucleus concentration (Fig. 13e). After introducing 2 mol% $APDI_2$ into the original perovskite precursor solution, the perovskite device ultimately achieved a PCE of 15.13% (Fig. 13f).[39] In addition, Li *et al.* developed an apolar sulfur-containing symmetric molecule, cyclic polysulfide 1,3,5-trithiane (TT). The three symmetric centers of TT can engage in multisite coordination with Sn^{2+}, not only increasing the oxidation barrier for Sn^{2+} and forming large-sized colloids in the precursor solution (Fig. 13g), but also reducing the nucleation barrier as well as delaying the crystal growth of $FASnI_3$

 This journal is © The Royal Society of Chemistry 2025

Published on 01 August 2025. Downloaded on 1/24/2026 5:38:31 AM.

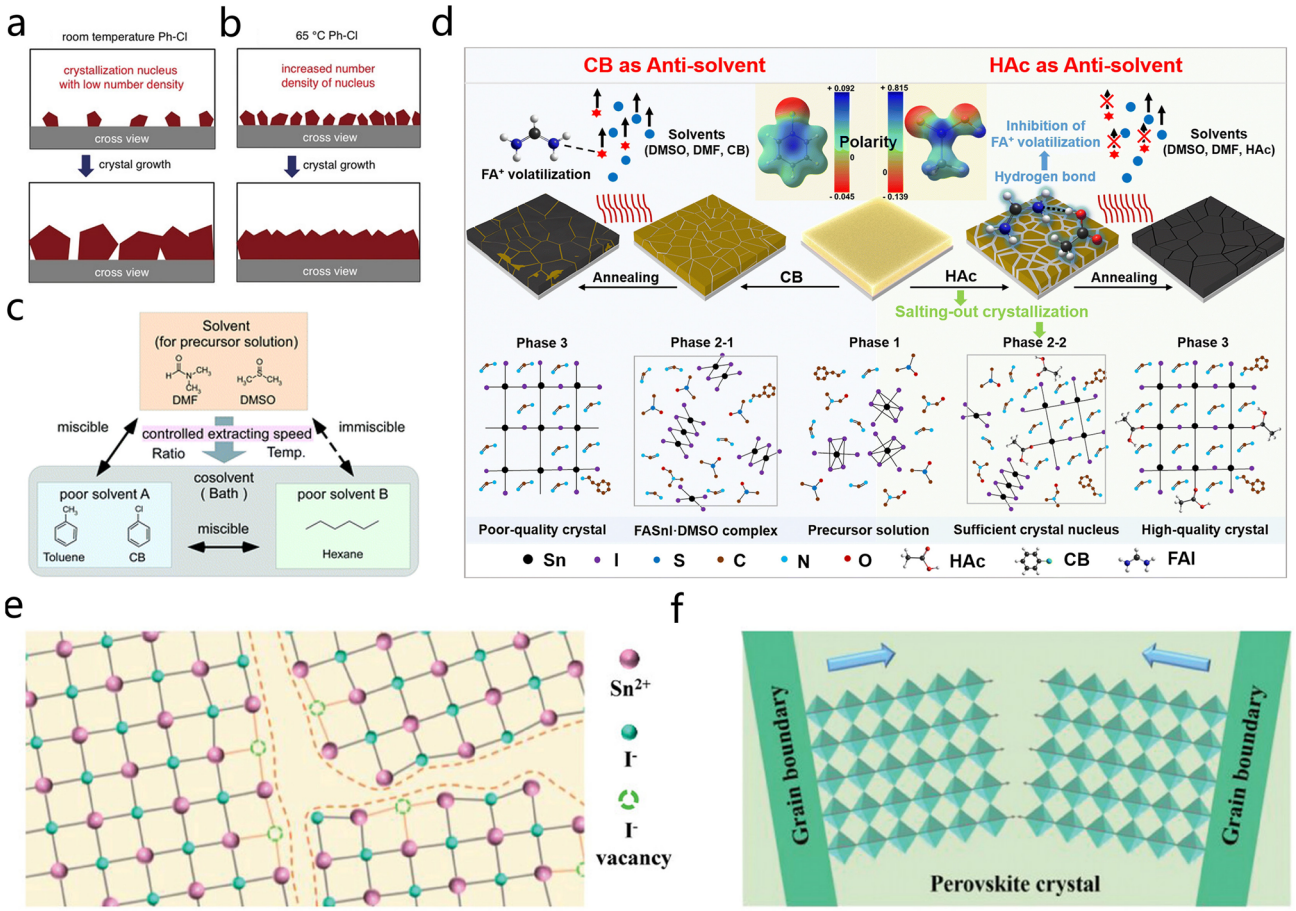

Fig. 12 Schematic of the mechanism for forming $FA_{0.75}MA_{0.25}SnI_3$ thin films using (a) rt Ph-Cl or (b) Ph-Cl preheated to 658 °C (HAT).[131] Copyright 2018, Wiley-VCH GmbH. (c) Conceptual illustration of controlling the crystallization rate by adding LT-Mix co-solvent technology to the solvent bath.[24] Copyright 2017, the Royal Society of Chemistry. (d) Process schemes for fabricating perovskite films using CB (control) or HAc as antisolvents and the composition of the films before and after each step.[132] Copyright 2023, the Royal Society of Chemistry. (e) Grain boundary iodide vacancies and (f) anisotropically stacked octahedral networks.[66] Copyright 2025, Wiley-VCH GmbH.

(Fig. 13h). The results indicate that the introduction of TT promotes the formation of uniform crystals during the film making process, achieving a PCE of 12.87% and excellent stability (unencapsulated devices maintain 90% of their initial PCE for over 3000 hours in nitrogen).[135]

3.2.2.2 Introduce nucleation sites. Nucleation sites perform a vital function in the crystallization process of perovskite thin layers. They provide starting points for the growth of perovskite crystals, helping to form uniform, large-sized perovskite unit cells. By introducing an appropriate amount of nucleation centers, the quality of perovskite thin films can be significantly improved, thereby enhancing the photoelectric PCE as well as the stability of solar cells. The following sections introduce non-homogeneous nucleation and hydrogen bond-assisted nucleation, respectively.[136]

SnF_2 is the least soluble compound in common solvents among the SnX_2 series (X = F, Cl, Br or I), because the bond energy of Sn halides increases as the radius of the halide ion decreases. During the spin-coating process, SnF_2 first precipitates out as the solvent evaporates. These precipitated homogeneous SnF_2 particles then act as non-homogeneous nucleation sites, promoting the growth of perovskite crystals and making the perovskite film more uniform (Fig. 14a).[137] Xiao *et al.* introduced SnF_2 into $MASnIBr_2$ perovskites, where it played a key role in providing non-homogeneous nucleation centers, promoting the formation of more Sn-based perovskite nucleus, as well as achieving better uniform, full-coverage crystal growth (Fig. 14b).[137] Studies have shown that polyvinyl alcohol (PVA) is a large-density hydroxyl group polymer, and its polar hydrogen group $O^{\delta-}$–$H^{\delta+}$ forms directional hydrogen bond interactions with electronegative iodide ions, $I^{\delta-}$ (Fig. 14c and d). Meng *et al.* introduced PVA into $FASnI_3$. The pendant hydroxyl groups of the PVA molecule engage in robust hydrogen bonding interactions with iodide ions, introducing nucleation sites (Fig. 14e and f), reducing the defect density, achieving a PCE of 8.9%, and improving stability (no attenuation after 400 h of maximum power operation).[138] In addition, Li *et al.* introduced the ionic liquid n-butylammonium acetate (BAAc) to regulate precursor coordination as well as the crystallization of perovskite towards high-performance thin films. O···Sn bonds, along with N–H···X hydrogen bonds, are established by the interaction of BAAc as well as the perovskite precursor. The

Published on 01 August 2025. Downloaded on 1/24/2026 5:38:31 AM.

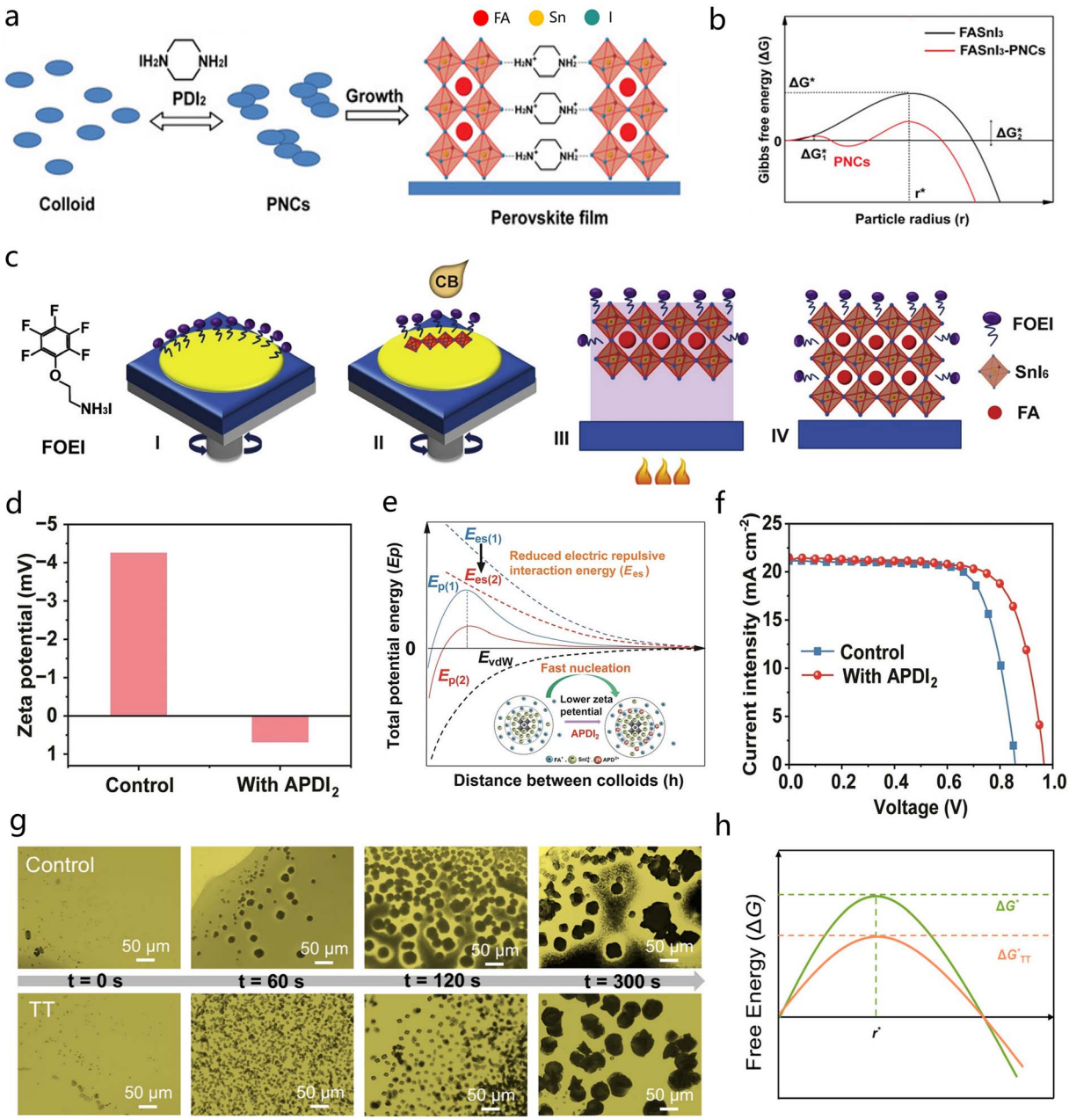

Fig. 13 (a) Schematic of the $FASnI_3$ perovskite film crystallization process based on PNCs.[33] Copyright 2020, Wiley-VCH GmbH. (b) Free energy distribution diagram of classical nucleation theory and non-classical nucleation theory based on pre-nucleation clusters (PNCs).[33] Copyright 2020, Wiley-VCH GmbH. (c) Possible scenarios for the surface-controlled growth of $FASnI_3$–FOEI perovskite films.[134] Copyright 2020, Elsevier. (d) Zeta potential of precursor solutions with and without $APDI_2$.[39] Copyright 2024, Wiley-VCH GmbH. (e) Effect of zeta potential on the total interaction potential energy of Sn halide perovskite colloidal particles with and without $APDI_2$.[39] Copyright 2024, Wiley-VCH GmbH. (f) *J*–*V* curve of the $FASnI_3$ champion device with 2 mol% $APDI_2$ added.[39] Copyright 2024, Wiley-VCH GmbH. (g) Optical microscopic images of perovskite precursor solutions heated at 100 °C without and with TT.[135] Copyright 2024, the American Chemical Society. (h) Schematic of the Gibbs free energy for nucleation as a function of nuclei radius in a precursor solution without (green) and with (orange) the addition of TT.[135] Copyright 2024, the American Chemical Society.

strong interaction formed provides more uniform nucleation sites, delaying the crystallization process (Fig. 14g and h), thereby forming flat and pinhole-free thin films, achieving a PCE of 10.4%.[139] Furthermore, Dong *et al.* introduced a hydrazine acetate (HAAc) that can form a strong coordination bond with Sn^{2+}. HAAc stabilizes Sn^{2+} and decouples crystallization by promoting the formation of pre-formed crystals (PFCs) in the precursor solution, allowing the PFCs to self-assemble during spin coating, thereby yielding $HA_xFA_{1-x}SnI_3$ perovskite films with tunable bandgaps, low defect densities, and crystalline orientation (Fig. 14i). The results show that the devices exhibit extremely high stability (unencapsulated devices

 This journal is © The Royal Society of Chemistry 2025

Published on 01 August 2025. Downloaded on 1/24/2026 5:38:31 AM.

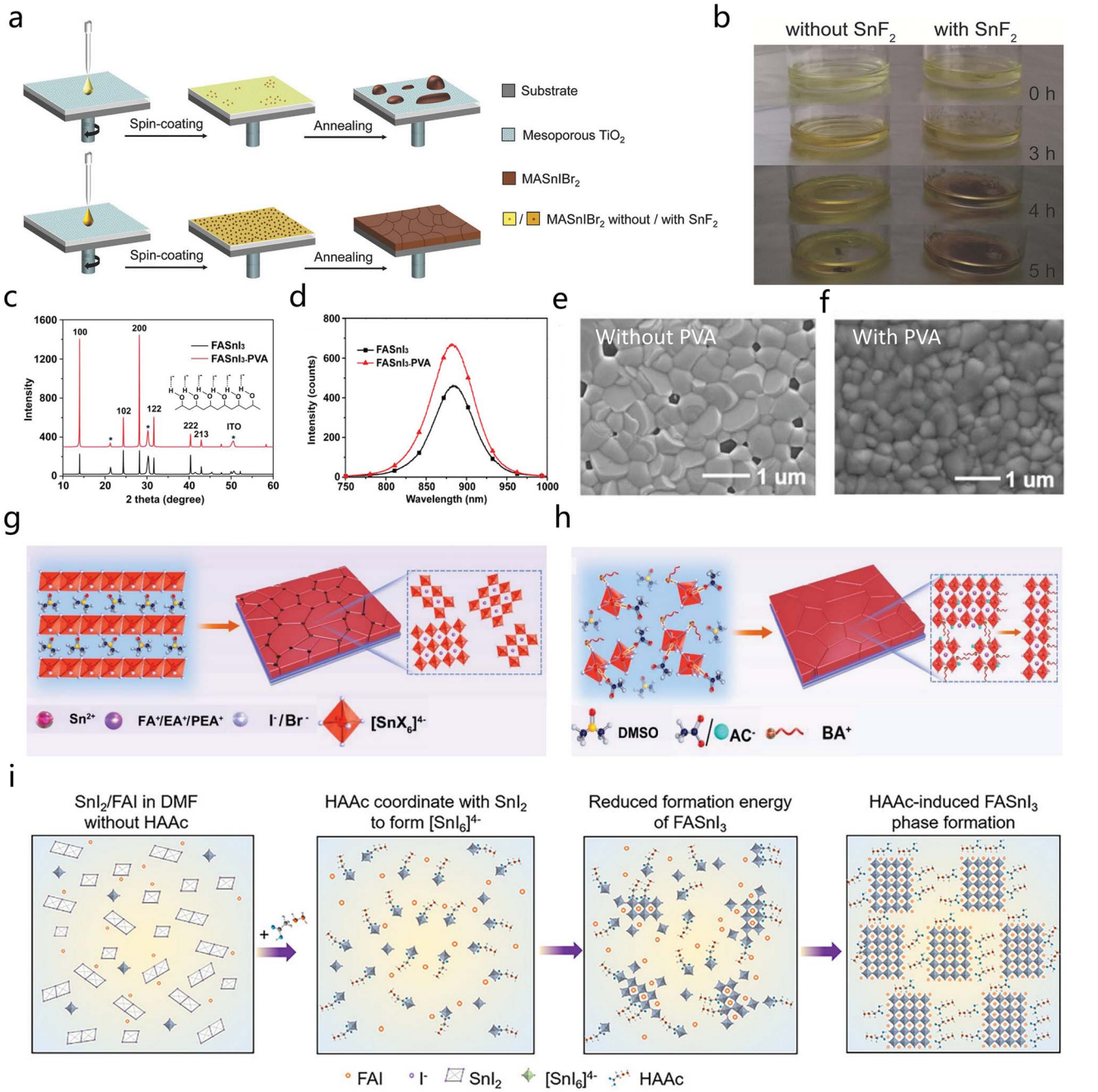

Fig. 14 (a) Schematic of two different nucleation and growth processes of Sn-based perovskites (with/without SnF_2).[137] Copyright 2017, Wiley-VCH GmbH. (b) Time-dependent crystallization products of $MASnBr_3$ without (left) and with 30 mol% SnF_2 (right).[137] Copyright 2017, Wiley-VCH GmbH. (c) ^1H NMR spectra of PVA, PVA + SnI_2 and PVA + FAI in DMSO-d_6 solution.[138] Copyright 2019, Wiley-VCH GmbH. (d) PL spectra of $FASnI_3$ perovskite films with and without PVA addition.[138] Copyright 2019, Wiley-VCH GmbH. SEM image of (e) $FASnI_3$ perovskite film and (f) $FASnI_3$–PVA perovskite film.[138] Copyright 2019, Wiley-VCH GmbH. Schematic of BAAc ionic liquid-assisted Sn-based perovskite thin film crystallization kinetics (g) without and (h) with BAAc.[139] Copyright 2021, Wiley-VCH GmbH. (i) Schematic of HAAc-induced crystallization of $FASnI_3$.[140] Copyright 2025, Wiley-VCH GmbH.

maintain 91% of their starting PCE after 700 hours of storage in N_2).[140]

3.2.3 Retarding crystallization

3.2.3.1 Lewis acid–base coordination. In TPSCs, Lewis acids typically represent Sn^{2+} ions, while Lewis bases usually function as additives to regulate the crystallization of perovskite layers. Lewis bases are defined by their capability to give electron pairs. By coordinating with Lewis acids (Sn^{2+}), Lewis base molecules form intermediate phases that delay crystallization during annealing. The coordinating ability of Lewis base molecules

Published on 01 August 2025. Downloaded on 1/24/2026 5:38:31 AM.

generally originates from the lone pairs of electrons provided by oxygen (O), sulfur (S), and nitrogen (N) atoms, which will be elaborated upon in the following sections.[141]

As a typical hard base, the O atom is characterized by its small atomic radius and high electronegativity. Sn^{2+} ions, acting as borderline acids, can form stable chemical bonds with O atom.[37] Dimethyl sulfoxide (DMSO) is one of the commonly used solvents in the production of perovskite films. Studies have shown that in the fabrication of Sn-based perovskites, DMSO can act as a Lewis base to interact with Sn^{2+}, forming the intermediate-phase $SnI_2 \cdot 3DMSO$, thereby delaying the crystallization of $CH_3NH_3SnI_3$ perovskites. Although the PCE is only 5.79%, the absorption range is relatively broad (Fig. 15a).[26] Jiang *et al.* introduced formamidinium acetate (FAAc) into $FASnI_3$ perovskites. FAAc dissociates into FA and Ac^-, with the latter possessing strong coordination ability. Ac^- preferentially coordinates with Sn^{2+} to form intermediate phases, thereby extending the reaction pathway for Sn perovskite film growth

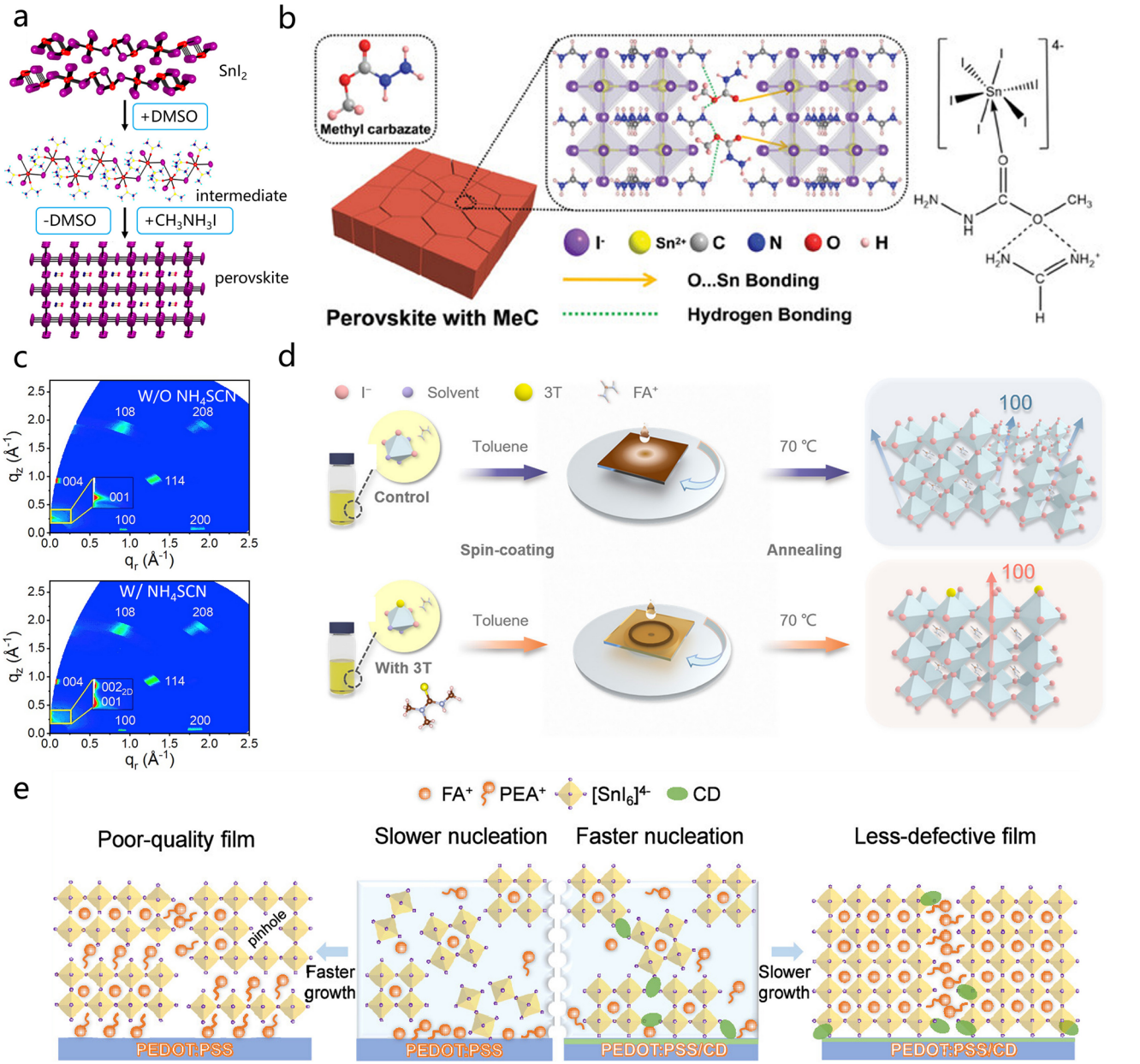

Fig. 15 (a) Schematic of the formation mechanism of the $CH_3NH_3SnI_3$ perovskite film: starting from SnI_2 and proceeding through the intermediate $SnI_2 \cdot 3DMSO$.[26] Copyright 2015, the American Chemical Society. (b) Schematic of the interaction between perovskites and MeC.[144] Copyright 2024, Wiley-VCH GmbH. (c) Absorption spectra (gray lines) and normalized photoluminescence spectra (red lines) of the control group, and absorption spectra (gray lines) and normalized photoluminescence spectra (orange lines) of the HSP structure.[147] Copyright 2018, Elsevier. (d) Schematic of the crystallization process of $FASnI_3$ films during spin-coating and annealing without (top) and with (bottom) 3T.[148] Copyright 2022, the American Chemical Society. (e) Schematic of the possible crystallization and nucleation process of Sn perovskite films without and with urea.[151] Copyright 2025, the American Chemical Society.

 This journal is © The Royal Society of Chemistry 2025

Published on 01 August 2025. Downloaded on 1/24/2026 5:38:31 AM.

and delaying crystallization. In a 1500 hour photostability test, the device retained 82% of its starting PCE.[142] Additionally to the coordination of O atoms, S atoms can also coordinate with Sn^{2+}, exhibiting even stronger coordination ability. Compared with O atoms, S atoms have a larger atomic radius and lower electronegativity, endowing them with soft base characteristics that match well with the borderline acid property of Sn^{2+} ions.[143] Research indicates that the introduction of methyl carbazate ($C_2H_6N_2O_2$, MeC) can boost Sn-based perovskite's crystallization through coordination between MeC and perovskite (O⋯Sn). The coordination of MeC with Sn^{2+} can delay the crystallization of perovskite in the precursor solution by enhancing nucleation sites, thereby reducing the density of deep-level trap states, significantly suppressing non-radiative recombination, and improving the carrier lifetime. This ultimately achieves a PCE of 14.02% and excellent stability (the champion device retains 93% of its starting PCE after 1500 hours of storage in a nitrogen environment) (Fig. 15b).[144] Additionally, Chen *et al.* found that urea, a Lewis base additive, can prolong the crystal growth process by coordination with Sn^{2+}, resulting in high-performance Sn-based perovskite layers with dense morphology, increased crystallinity, and reduced defects. This ultimately achieved a PCE of 14.22%.[145] In addition to this, the introduction of polymethyl methacrylate (PMMA) has been proven to facilitate the recrystallization of $FASnI_3$. During the recrystallization process, the carboxyl groups on PMMA form strong coordination bonds with Sn^{2+} cations, enriching Sn^{2+} on the surface of $FASnI_3$. This enrichment suppresses the formation of defects, thereby accelerating the directional separation of photo-generated electrons and holes as well as increasing the PCE to 13.82%.[146] Wang *et al.* introduced the mobile pseudo-halide ammonium thiocyanate (NH_4SCN) into $FASnI_3$. SCN^-, a π-conjugated Lewis base, coordinates with the Lewis acid SnI_2 to generate $FASnI_{3-x}SCN_x$, resulting in a parallel-oriented, layered 2D–3D structure that delays crystallization and enhances stability (retaining nearly 90% of its initial performance after 600 hours) (Fig. 15c).[147] Thiourea derivatives, which commonly coordinate through S atoms, are typical Lewis bases. Zhu *et al.* introduced a bifunctional ligand, trimethylthiourea (3T). By expanding and connecting individual grains, 3T delays crystallization and significantly improves the morphology of $FASnI_3$ perovskite films, achieving a PCE of 14.0% (Fig. 15d).[148] N atoms, acting as effective heteroatoms in Sn perovskites, exhibit strong coordination ability with Sn^{2+}.[149] A studies has shown that *trans*-pyridine (TPPF), a spatially separated Lewis base, has the ability to capture more perovskite colloids through coordination, which helps to decelerate Sn perovskite's crystallization procedure and ultimately achieves a high PCE of 15.38%.[150] Wang *et al.* co-introduced phenylhydrazinium cations ($PhNHNH_3^+$) and halide anions (Cl^- and Br^-). $PhNHNH_3^+$ passivates trap states in the perovskite film, while inhibiting the aggregation of Br^-, thereby increasing the grain size and delaying crystallization, achieving a PCE of 13.4%.[32] In addition to this, Zeng *et al.* constructed a supramolecular layer using 3D polydentate methyl-β-cyclodextrin (CD). The weakened coordination in the middle of CD and ammonium at the supramolecular interface is conducive to accelerating the nucleation rate, while the multi-site interactions across diverse spatial dimension directions decelerate their crystal growth, resulting in a more dense and lesser defective Sn-based perovskite film (Fig. 15e). The results show that this supramolecular interlayer has a better improvement effect on crystallization, increasing the PCE of TPSCs to 14.94%. Meanwhile, the unsealed devices perform excellent stability after about 4000 hours of storage.[151] Additionally, Muhammad *et al.* introduced a method of crystallization regulation using 4-aminopyridine hydrochloride (4APCl). 4APCl coordinates with the intermediate (+M) in the perovskite precursor, precisely controlling $FASnI_2Br$ perovskite's crystallization kinetics by the production of a 6H intermediate phase, thereby fabricating highly efficient indoor photovoltaics.[152]

3.2.4 Antioxidant. Oxidation is one of the primary reasons for the low PCE of PSCs. When Sn-based perovskites are exposed to an oxygen-rich environment, Sn^{2+} ions are readily oxidized to Sn^{4+}. This oxidation process leads to the degradation of the perovskite structure, thereby reducing the photovoltaic PCE. Moreover, under simultaneous exposure to light and oxygen, oxygen molecules have the ability to permeate the perovskite lattice, accepting photoexcited electrons from it and thereby generating superoxide ions (O_2^-). These reactive superoxide ions can disrupt the B–X bonds in the perovskite ABX_3 structure, leading to the deprotonation of the organic cations within the perovskite and accelerating the degradation of the material.[153] The following section introduces several substances that inhibit oxidation to achieve a deceleration of crystallization.

Omar *et al.* introduced a novel ligand, thiophene-2-ethylammonium halide (TEAX). The S atoms in TEAX coordinate with Sn^{2+} to form complexes, preventing the formation of low-dimensional phases and thereby inhibiting Sn^{2+} from being oxidized to Sn^{4+}. This significantly enhances Sn-based perovskite solar cells' stability, maintaining 95% PCE after persistent functioning below nitrogen for 2000 hours (Fig. 16a).[154] Studies have shown that when $SnCl_2$ is available in excess, the use of hydroxybenzenesulfonic acid (KHQSA) as a bifunctional additive significantly enhances the air stability of $FASnI_3$ PSCs. On the one hand, the additive helps eliminate phase separation caused by $SnCl_2$, forming a $SnCl_2$-additive complex layer that encapsulates the perovskite film. On the other hand, the reductive hydroxyl groups in the additive molecules act as oxygen scavengers (antioxidants), further protecting the internal perovskite and maintaining long-term air stability. Based on this approach, Tai *et al.* achieved highly stable $FASnI_3$ PSCs that retained 80% PCE after exposure to air for over 500 hours without encapsulation (Fig. 16b and c).[155] Additionally, Dong *et al.* utilized a reductive ionic liquid, methylammonium formate (MAFa), to drive a controlled crystallization process and inhibit the oxidation of Sn^{2+} in $FASnI_3$ perovskite films. During film formation, the interaction between C=O and Sn^{2+}, as well as the N–H⋯I hydrogen bonding in the middle of MAFa and $FASnI_3$ precursors, delays the crystallization of $FASnI_3$, promotes oriented film growth, and reduces defect traps. Moreover, the strong reductive nature of the –CHO groups in MAFa suppresses the oxidation of Sn^{2+} in the film. As a result, MAFa-modified TPSCs exhibited higher stability, maintaining

Published on 01 August 2025. Downloaded on 1/24/2026 5:38:31 AM.

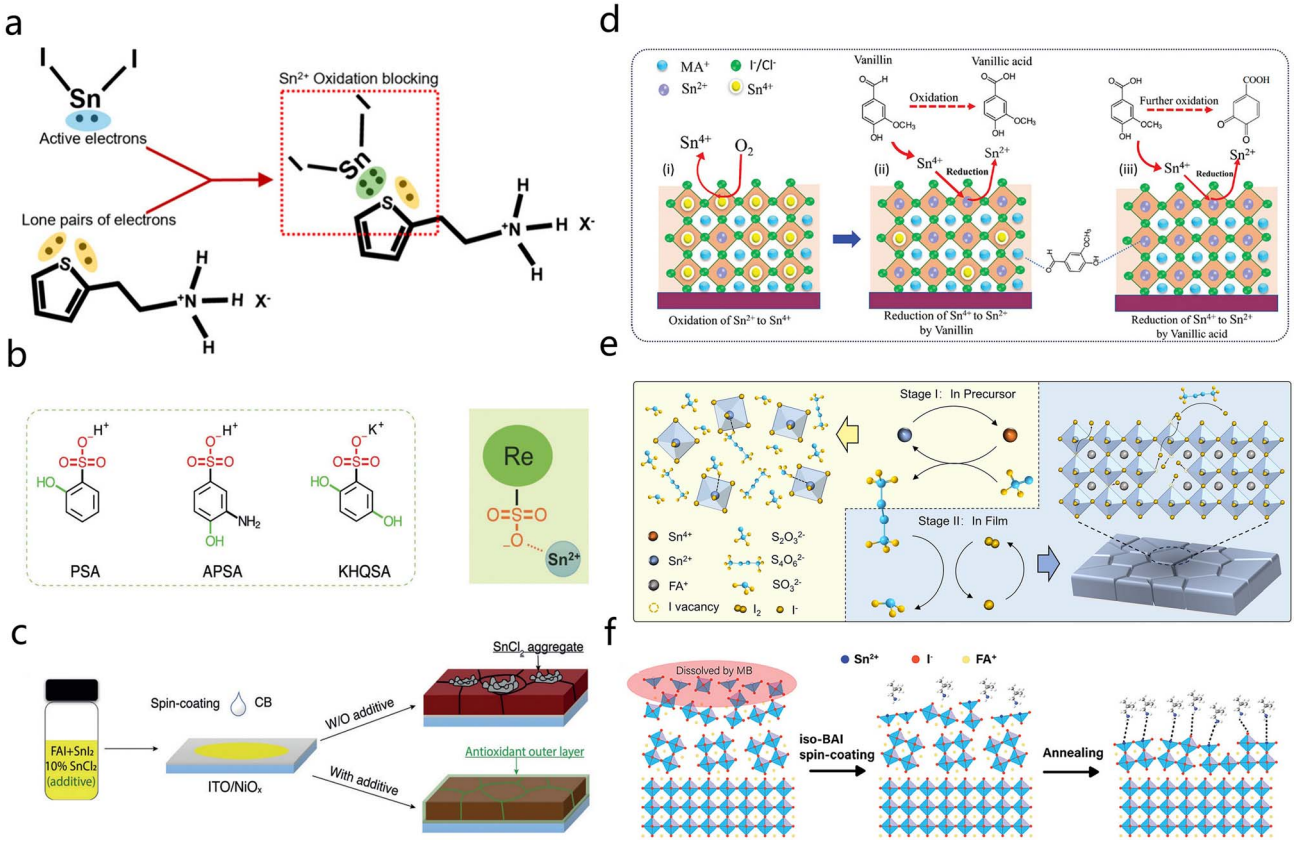

Fig. 16 (a) Coordination interactions between TEAX and Sn^{2+} ions.[154] Copyright 2024, the American Chemical Society. (b) Schematic of the interactions between additive molecules and Sn^{2+} ions.[155] Copyright 2019, Wiley-VCH GmbH. (c) Morphologies of the control and experimental groups.[155] Copyright 2019, Wiley-VCH GmbH. (d) Schematic of the two-stage redox reaction between vanillin and Sn-based perovskite.[158] Copyright 2024, Wiley-VCH GmbH. (e) Schematic of the dual reduction process of thiosulfate in precursors and thin films.[159] Copyright 2024, Wiley-VCH GmbH. (f) Schematic of the surface dissolution–recrystallization process of the Sn perovskite.[67] Copyright 2024, Wiley-VCH GmbH.

80% PCE after 500 hours in a N_2 atmosphere without encapsulation.[156] Furthermore, ammonium hypophosphite (AHP) can reduce oxidized perovskites to pale yellow-colored materials, inhibiting the oxidation of Sn^{2+} and promoting grain growth. Under these conditions, the stability of $FASnI_3$ PSCs was enhanced, retaining 50% of the starting PCE after 500 hours in air.[157]

In recent years, researchers have developed several dual antioxidants. Andrew *et al.* introduced vanillin, a dual-stage natural antioxidant. The hydroxyphenyl group on the vanillin molecule has a strong affinity for free radicals, rendering vanillin a potent reducing agent. Interestingly, vanillic acid, the oxidation product of vanillin, is also an antioxidant, which significantly enhances the antioxidant effect of vanillin (Fig. 16d). The lone-pair electrons on vanillin's oxygen-containing side groups such as aldehyde, ether, and phenol groups can induce coordination as well as electrostatic interactions in the middle of perovskite and vanillin, thereby slowing down crystallization. Ultimately, with the incorporation of 7.5% vanillin, the TPSC achieved a PCE of 13.18% and excellent stability and sustainability (after exposure for 3 minutes under 160 W microwave irradiation, the PCE recovered from 88% to 96.5% within 812 hours, and from 35.7% to 65.4% after 2200 hours).[158] Furthermore, Yang *et al.* discovered that thiosulfate $S_2O_3^{2-}$ has dual reduction capabilities. $S_2O_3^{2-}$ can reduce Sn^{4+} to Sn^{2+} in the precursor stage, and also reduce I_2 to I^- in the thin-film stage (Fig. 16e). This significantly prevents Sn^{2+} from being oxidized to Sn^{4+} as well as passivates defects, effectively enhancing the PCE and TPSC's stability. Consequently, the PCE of the TPSC was increased to 14.78%, and after operating at the maximum power point for 628 hours, its initial PCE remained at 90%.[159] In addition, the introduction of a ligand, isobutylammonium iodide (iso-BAI), can induce recrystallisation on Sn perovskite thin layers' surface, thereby slowing down crystallization and inhibiting Sn^{2+} oxidation (Fig. 16f).[67] This ligand enabled the TPSC to reach a PCE of 14.2%. Studies have shown that the introduction of 2,8-dibromo-dibenzothiophene-*S*,*S*-dioxide (BrDS) can effectively prevent the Sn^{2+} from being oxidized as well as address grain boundary defects and point defects in perovskite thin layers. BrDS-doped Sn-based perovskite thin films have greater carrier lifetimes as well as crystal quality, exhibiting a high PCE of 14.36% and stability maintaining 90% of the original PCE after storage in an N_2 atmosphere for 1200 hours.[160]

3.2.4.1 Hydrogen bonds. Hydrogen bonds originate from the attractive interactions between hydrogen atoms within

 This journal is © The Royal Society of Chemistry 2025

Published on 01 August 2025. Downloaded on 1/24/2026 5:38:31 AM.

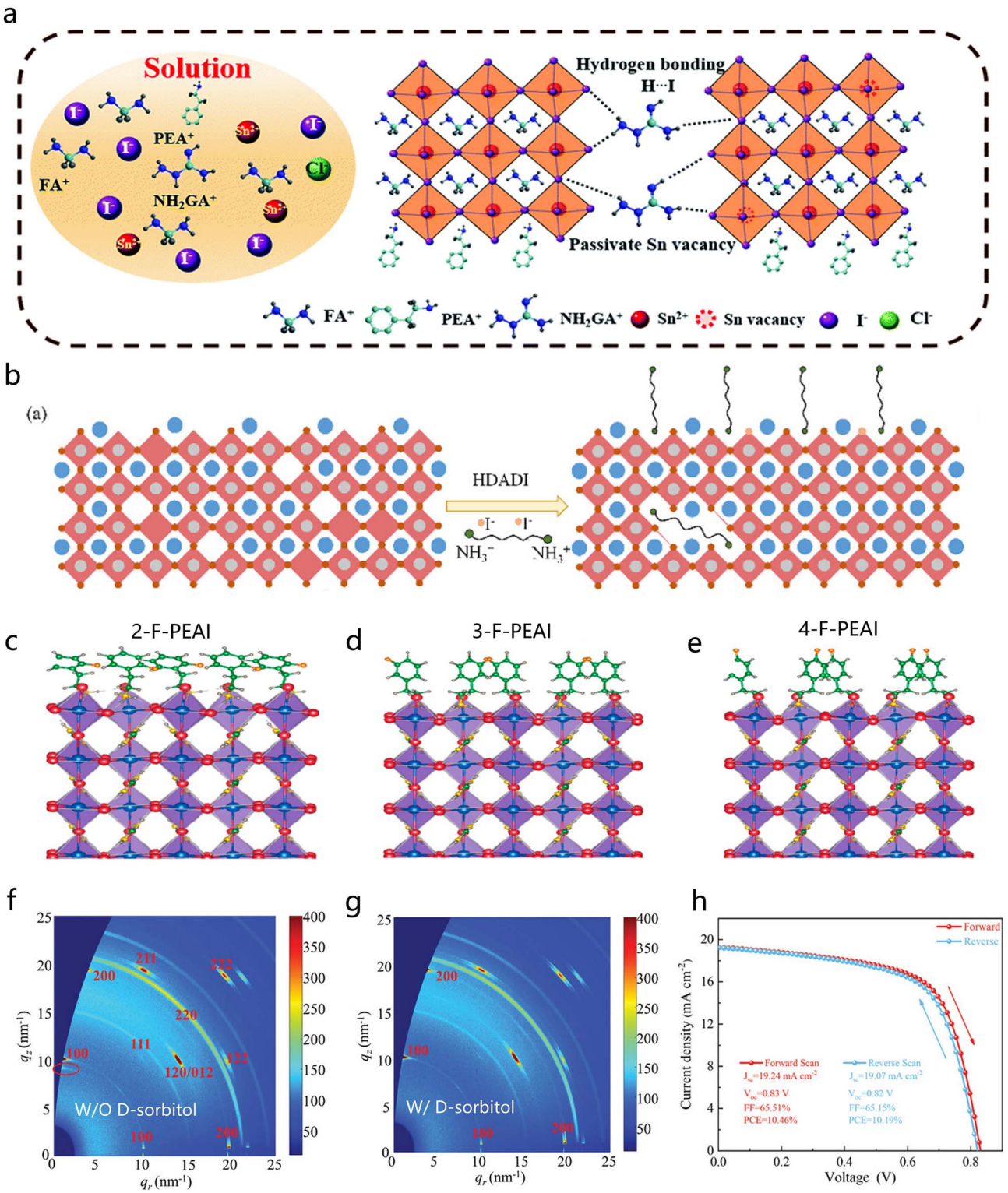

Fig. 17 (a) Schematic of the passivation mechanism of NH_2GACl.[162] Copyright 2020, the Royal Society of Chemistry. (b) Comparison of the crystallinity of $FASnI_3$ perovskites with and without HDADI additives.[163] Copyright 2020, the American Chemical Society. (c–e) DFT simulations of the spatial arrangement of supercells in 2-F-PEAI, 3-F-PEAI, and 4-F-PEAI modified perovskites.[164] Copyright 2020, the American Chemical Society. (f and g) GIWAXS of $PEA_{0.1}(FA_{0.75}MA_{0.25})_{0.9}SnI_3$ perovskite films on pristine PEDOT:PSS and D-sorbitol-doped PEDOT:PSS.[165] Copyright 2021, Wiley-VCH GmbH. (h) *J*–*V* curves of the highest-performing PSC measured under forward and reverse voltage scans (20 mg per mL D-sorbitol).[165] Copyright 2021, Wiley-VCH GmbH.

Published on 01 August 2025. Downloaded on 1/24/2026 5:38:31 AM.

molecules or their fragments, typically represented as R–H···X. As an important type of directional intermolecular interaction, the tunable strength and directionality of hydrogen bonds provide an effective means for modulating the properties of materials and devices.[161] The introduction of hydrogen bonds can increase nucleation sites, thereby slowing crystal growth and facilitating the formation of dense $FASnI_3$ films.

Fu *et al.* employed a facile method by incorporating guanidinium hydrochloride (NH_2GACl) into the perovskite precursor solution, thereby significantly improving the film quality. The halide ions in NH_2GACl form robust hydrogen bonds with the perovskite structure, which not only passivates defects but also reduces the oxidation rate of Sn^{2+}. This process enhances crystallinity while retarding crystallization, thereby improving film quality (Fig. 17a).[162]

Additionally, targeting the amino passivation of SnI_6^{4-}, Ma *et al.* introduced HDADI into $FASnI_3$ PSCs. The hydrogen bonding interactions between NH_3^+ and the SnI_6^{4-} octahedra result in high-performance perovskite films as well as high coverage, enhanced crystallinity, elimination of pinholes, increased radiative recombination, and extended carrier lifetimes. These hydrogen bonds neutralize charged defects or dangling bonds in the perovskite and form a shielding layer that inhibits the oxidation of Sn^{2+} to Sn^{2+}, thereby retarding crystallization (Fig. 17b). Consequently, this approach achieves excellent PCE and stability.[163] Meng *et al.* showed that the induction of polyvinyl alcohol (PVA) can retard $FASnI_3$'s crystallization rate by hydrogen bonding. Liquid-state ^1H NMR measurements revealed that –OH protons' resonance signals in PVA were significantly broader, pointing the presence of O–H···I^- hydrogen bonds. These interactions prevent the out-of-plane and in-plane rotation of the neighboring SnI_6^{4-} octahedral framework, thereby slowing crystal growth and guiding crystal orientation.[138] Furthermore, Li *et al.* utilized density functional theory (DFT) to perform first-principles calculations, finding that 2-F-PEA, with its bent geometry arranged in a uniform direction on the surface, exhibits stronger structural robustness compared to other isomers (*e.g.*, 4-F-PEA and 3-F-PEA), thereby controlling film crystallization (Fig. 17c and d).[164] Chen *et al.* introduced D-sorbitol into PEDOT:PSS, and the resulting perovskite films exhibited brighter and more discrete Bragg spots compared to pristine devices. The crystallization of the films was significantly suppressed, ultimately achieving maximum PCEs of 10.46% and 10.19% under forward and reverse voltage scans, respectively, for champion devices (Fig. 17e–g).[165]

All the key information on the structural engineering of Sn-based PSCs in this section is summarized in Table 2.

3.3 Interface engineering

TPSCs have two main types of structures: the formal (n-i-p) and the inverted (p-i-n). Initially, researchers focused on formal perovskite structures. However, formal PSCs generally exhibit lower efficiency.[171–175] Commonly used ETLs (electron transport layers) such as TiO_2 (ref. 171 and 173–175) and SnO_2 (ref. 172) are hydrophilic. This hydrophilicity leads to poor wettability of the perovskite precursor solution, which contains organic solvents, on the ETL surface. As a result, it is difficult to form high-quality, continuous thin films. In addition, the energy-level mismatch between Sn-based perovskites and ETLs results in insufficient charge extraction, causing significant hysteresis effects and substantial open-circuit voltage losses in the devices.[62] Consequently, since 2016, the p-i-n structure has gradually attracted researchers' attention and has become the predominant structure for most TPSCs over the subsequent decade.[17,43] The HTL (hole transport layer) substrate used in inverted perovskite structures is fabricated *via* low-temperature processes, which reduce the surface roughness of the thin films. Moreover, the HTL at the bottom and the ETL at the top typically have more compatible carrier mobility. However, inverted perovskite structures also have issues such as buried interfacial defects,[176] energy level mismatches,[177] and unstable transport layers.[178] Therefore, the interfacial problems in TPSCs can be discussed from the perspectives of the HTL/perovskite and ETL/perovskite interfaces.

3.3.1 HTL/PVSK interface. Interface engineering of the HTL/PVSK has a substantial impact on optimizing the alignment of interface energy levels, decreasing non-radiative recombination, and enhancing charge extraction PCE. To further improve film quality and facilitate carrier transport, researchers have mainly employed interface modification strategies (such as organic ammonium salts, SAMs, hydroxy-based molecules, and inorganic salts) and HTL replacements (such as SnO_x and PTAA). This section will provide a detailed discussion.[75]

3.3.1.1 Organic ammonium salts. Organic amines can anchor onto perovskite films to exert regulatory effects. These organic compounds containing amino groups ($-NH_2$) form strong coordination bonds with uncoordinated Sn^{2+} in perovskites through their lone pair of electrons, effectively passivating interfacial defects and reducing non-radiative recombination losses by an order of magnitude. Gao *et al.* confirmed the function of chiral cations, α-methylbenzylamine (*S*-/*R*-/*rac*-MBA), in facilitating hole transport in $FASnI_3$-based PSCs (Fig. 18a and b). It was found that the introduction of MBA forms 2D–3D films featuring low-dimensional structures at the interface of PEDOT:PSS/$FASnI_3$, which is beneficial for interfacial energy level alignment and efficient charge transfer. Importantly, the chiral *R*-MBA cation-induced chiral-driven spin selectivity (CISS) effect in *R*-MBA_2SnI_4 further facilitates accumulated holes' specific interfacial transport (Fig. 18c).[179] The results indicated that PSCs based on *R*-MBA achieved a good PCE of 10.73%, featuring minimized hysteresis as well as boosted device stability. Kuan *et al.* modified the surface of PTAA with phenethylammonium iodide (PEAI) (Fig. 18d and e). Studies have shown that the π–π interactions between phenyl rings help improve the hydrophobicity of PTAA films, thereby generating high-quality Sn-based perovskite films (Fig. 18f). TPSCs prepared with PTAA modified by PEAI achieved a photoelectric PCE of 8.3%, significantly higher than the 1.6% of untreated PTAA.[69] Studies have shown that the upper interface can be regulated by adjusting the main chain length of alkylamine. Long-chain alkylamine ODAI can act as a crystallization

 This journal is © The Royal Society of Chemistry 2025

Published on 01 August 2025. Downloaded on 1/24/2026 5:38:31 AM.

Table 2 Summary of the regulation strategies and performance in the crystallization of Sn-based PSCs

Matrix	Strategy	Solvent/additive	V_{OC} (V)	J_{SC} (mA cm^{-2})	FF (%)	PCE (%)	Shelf stability	Ref.
$MASnI_3$	Anti-solvent	DMSO/diethyl	44.90	20.69	58.20	6.22	Retain 85% of the initial PCE after 30 d in air with encapsulation	20
$MASnI_3$	Anti-solvent	DMSO/toluene	0.45	11.82	40	2.49	—	28
$FASnI_3$	Anti-solvent	DMSO/Ph-Cl	0.55	19.4	67	7.20	Retain 100% of the initial PCE after 70 h in N_2 without encapsulation	131
$FASnI_3$	Anti-solvent	DCB	0.82	22.82	79.32	14.85	—	66
$FA_{0.75}MA_{0.25}SnI_3$	Anti-solvent	DMF, DMSO/CB	0.55	24.30	67	9.06	Retain 75% of the initial PCE after 30 d in N_2 with encapsulation	27
$(FA_{0.9}EA_{0.1})_{0.98}EDA_{0.01}SnI_3$	Anti-solvent	HAc	0.92	18.84	73.72	12.78	—	132
$FASnI_3$	Lower energy barrier	PPA	0.56	23.34	73.50	9.61	Retain 92% of the initial PCE after 1440 h in N_2 without encapsulation	121
$FASnI_3$	Lower energy barrier	FOEI	0.67	21.59	75	10.16	—	134
$FASnI_3$	Lower energy barrier	BMIBr	0.70	19.86	72.36	10.09	Retain 85% of the initial PCE after 1200 h in N_2 without encapsulation	166
$CsSnBrI_2$	Lower energy barrier	PEASCN	0.43	17.20	68.70	5.01	—	167
$FASnI_3$	Lower energy barrier	PNCs	0.69	21.85	75.10	11.39	—	33
$FASnI_3$	Lower energy barrier	TT	0.81	22.88	69.44	12.87	Retain 90% of the initial PCE after 3000 h in N_2 without encapsulation	135
$FASnI_3$	Lower energy barrier	$APDI_2$	0.97	21.58	72.29	15.13	Retain over 90% of the initial PCE after 100 d in N_2 with encapsulation	39
$MASnIBr_2$	Introduce nucleation sites	SnF_2	0.45	13.77	59.58	3.70	Retain over 80% of the initial PCE after 60 d in N_2 with encapsulation	137
$FASnI_3$	Introduce nucleation sites	PVA	0.63	20.37	69.30	8.90	—	138
$FASnI_3$	Introduce nucleation sites	BAAc	0.65	22.20	71.60	10.4	Retain 96% of the initial PCE after 1000 h in N_2 without encapsulation	139
$FASnI_3$	Anti-oxidation	KHQSA, $SnCl_2$	—	17.64	—	6.76	Retain 80% of the initial PCE after 500 h in air without encapsulation	155
$FASnI_3$	Anti-oxidation	PHCl	0.76	23.50	64.00	11.40	Retain almost 100% of the initial PCE after 110 d in N_2 with encapsulation	168
$FASnI_3$	Anti-oxidation	LFA	—	21.97	—	10.37	—	169
$MASnI_3$	Anti-oxidation	EABr	0.72	19.08	69.62	9.59	Retain 93% of the initial PCE after 30 d in N_2 with encapsulation	153
$FASnI_3$	Anti-oxidation	MAFa	0.55	21.41	71.71	8.50	Retain 80% of the initial PCE after 500 h in N_2 with encapsulation	156
$FASnI_3$	Anti-oxidation	TU	0.55	22.80	67.00	10.90	Retain 115% of the initial PCE after 1 year in N_2 without encapsulation	170
$FASnI_3$	Anti-oxidation	TEAX	0.42	21.60	70.00	12.00	—	154
$FASnI_3$	Anti-oxidation	iso-BAI	0.72	26.10	75.70	14.20	—	67
$FASnI_3$	Anti-oxidation	$3AMPYSnI_4$	0.78	23.31	73.08	13.28	Retain 96% of the initial PCE after 1200 h in N_2 without encapsulation	129
$FASnI_3$	Anti-oxidation	BrDS	0.79	23.86	79.45	14.98	Retain 90% of the initial PCE after 3000 h in N_2 without encapsulation	160
$FASnI_3$	Anti-oxidation	$(S_2O_3)^{2-}$	0.96	21.67	70.94	14.78	Retain 99% of the initial PCE after 2000 h in N_2 with encapsulation	159

This journal is © The Royal Society of Chemistry 2025

Published on 01 August 2025. Downloaded on 1/24/2026 5:38:31 AM.

Table 2 (*Contd.*)

Matrix	Strategy	Solvent/additive	V_{OC} (V)	J_{SC} (mA cm^{-2})	FF (%)	PCE (%)	Shelf stability	Ref.
$MASnI_3$	Anti-oxidation	Vanillin	1.01	22.08	75.30	13.18	—	158
$FASnI_3$	Lewis acid–base coordination	PHCl-Br	0.81	22.42	—	13.4	Retain 91% of the initial PCE after 4800 h in N_2 without encapsulation	32
$FASnI_3$	Lewis acid–base coordination	$C_3H_6N_6$	0.69	21.17	70.36	10.3	Retain 85% of the initial PCE after 1350 h in N_2 without encapsulation	149
$FASnI_3$	Lewis acid–base coordination	TPPF	0.85	24.81	72.37	15.38	Retain 99% of the initial PCE after 3000 h in N_2 without encapsulation	150
$FASnI_3$	Lewis acid–base coordination	FAAc	0.96	20.47	74.56	14.60	—	142
$FASnI_3$	Lewis acid–base coordination	4A3HA	0.84	20.98	68.53	13.43	Retain 80% of the initial PCE after 133 h in air without encapsulation	34
$FASnI_3$	Lewis acid–base coordination	3T	0.92	20.30	77.00	14.00	Retain almost 100% of the initial PCE after 30 d in N_2 without encapsulation	148
$FASnI_3$	Lewis acid–base coordination	PMMA	0.85	22.74	71.50	13.82	—	146
$FASnI_3$	Lewis acid–base coordination	urea–SnI_2	0.89	22.09	72.46	14.22	Retain 88.7% of the initial PCE after 2184 h in N_2 without encapsulation	145
PEA_2SnI_4	Lewis acid–base coordination	NH_4SCN	0.61	22.00	70.10	9.41	Retain 90% of the initial PCE after 600 h in N_2 without encapsulation	147
$FASnI_3$	Hydrogen bond	HDADI	0.51	21.46	68.87	7.60	Retain 80% of the initial PCE after 550 h in N_2 without encapsulation	163
$PEA_{0.1}FA_{0.9}SnI_3$	Hydrogen bond	NH_2GACl	0.54	19.30	68.10	7.30	Retain 90% of the initial PCE after 30 d in N_2 without encapsulation	162
$FASnI_3$	Hydrogen bond	2-F-PEA	0.69	21.53	68.46	10.17	—	164
$FA_{0.75}MA_{0.25}SnI_3$	Hydrogen bond	D-Sorbitol	0.83	19.24	67.00	10.46	Retain over 75% of the initial PCE after 700 h in N_2 without encapsulation	165
$FASnI_3$	Hydrogen bond	MeC	0.77	24.34	74.42	14.02	—	144

This journal is © The Royal Society of Chemistry 2025

Published on 01 August 2025. Downloaded on 1/24/2026 5:38:31 AM.

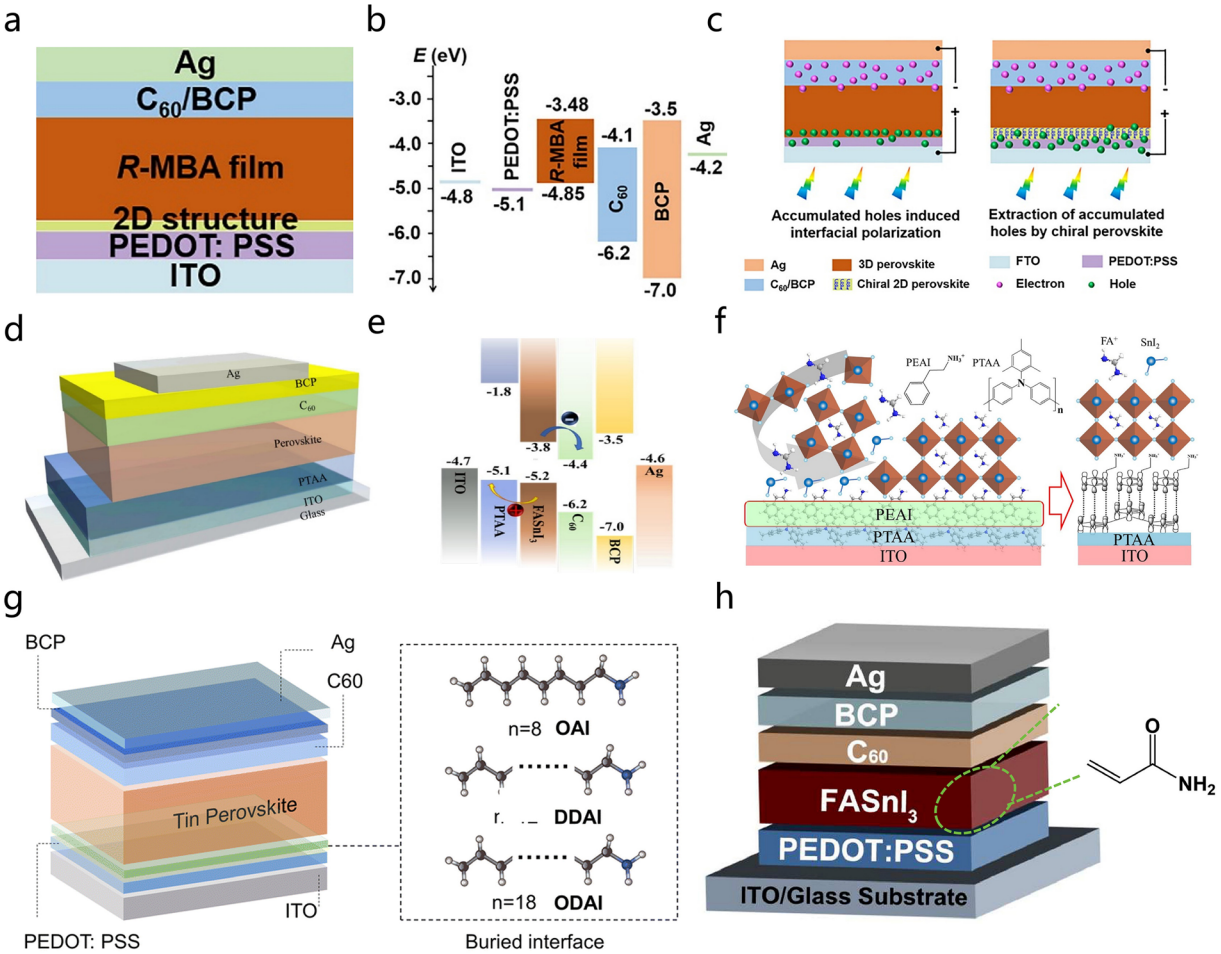

Fig. 18 (a) Device structure under investigation.[179] Copyright 2021, Elsevier. (b) Energy level diagram of the PSC device based on *R*-MBA.[179] Copyright 2021, Elsevier. (c) Schematic of enhanced hole extraction in PSC devices with non-chiral and chiral perovskite layers.[179] Copyright 2021, Elsevier. (d) Inverted configuration of the TPSC device.[69] Copyright 2022, Elsevier. (e) Potential energy diagram of each layer in the device.[69] Copyright 2022, Elsevier. (f) Schematic of the π–π stacking effect at the PTAA/PEAI interface.[69] Copyright 2022, Elsevier. (g) Schematic of the device structure of TPSCs: three long-chain alkylamines as buried interlayers, namely OAI, DDAI, and ODAI.[180] Copyright 2023, the Royal Society of Chemistry. (h) Device structure and chemical structure of acrylamide.[181] Copyright 2024, Elsevier.

buffer molecule to release residual compressive strain in Sn perovskite films, thereby reducing trap state density, suppressing non-radiative recombination, and ultimately achieving a PCE of 13.82% (Fig. 18g).[180] Additionally, Zeng *et al.* introduced the Lewis base acrylamide (AM), containing carbon–carbon double bonds as well as electrophilic amide groups, as a dopant in a PEDOT:PSS solution. AM can optimize the energy level matching and the hole transfer PCE of TPSCs, achieving a PCE of 6.22% (Fig. 18h).[181]

3.3.1.2 Self-assembled monolayer (SAM). SAMs have demonstrated unique advantages in precise regulation for interfacial engineering in PSCs. These molecules form chemical bonds with the substrate through terminal anchoring groups (such as phosphate or carboxyl groups), while their functional groups at the other end (such as amine, thiol, or methyl groups) can directionally modulate interfacial properties. In addition, SAMs possess several other advantages including molecular designability, excellent mechanical flexibility, no need for dopants, and negligible light transmission loss.[182]

Song *et al.* prepared an integrated SAM as the HTL layer using a one-step method (Fig. 19a). The introduction of 6PA forms a MeO-2PACz : 6PA mixed SAM, which, in addition to the C–O···Sn^{2+} coordination bond of MeO-2PACz, can promote the interaction between Sn perovskite and carboxylic acid through OH···halide hydrogen bonds and C···O···Sn^{2+} coordination bonds (Fig. 19b). The 6PA enables hydrogen bonds to suppress iodide vacancies, thereby reducing the trap state concentration in Sn perovskite. Meanwhile, the hydrophobicity of the terminal MeO-2PACz group is lower than that of the precursor solvent DMSO, leading to phase separation in the Sn-based perovskite layer. In contrast, a fully covered and uniform Sn-based perovskite film is formed on the self-assembled monolayer with a molar ratio of MeO-2PACz to 6PA of 1/1, effectively preventing the oxidation of Sn^{2+} (Fig. 19c).[76] The bulk defects clearly visible in the HTL/PVK film may emerge from the high acidity and PEDOT:PSS's hydrophilicity. Therefore, Cho *et al.* introduced MeO-2PACz as well as 2PACz SAM molecules at the interface between PEDOT:PSS HTL and Sn-PVK (Fig. 19d and e). The

Published on 01 August 2025. Downloaded on 1/24/2026 5:38:31 AM.

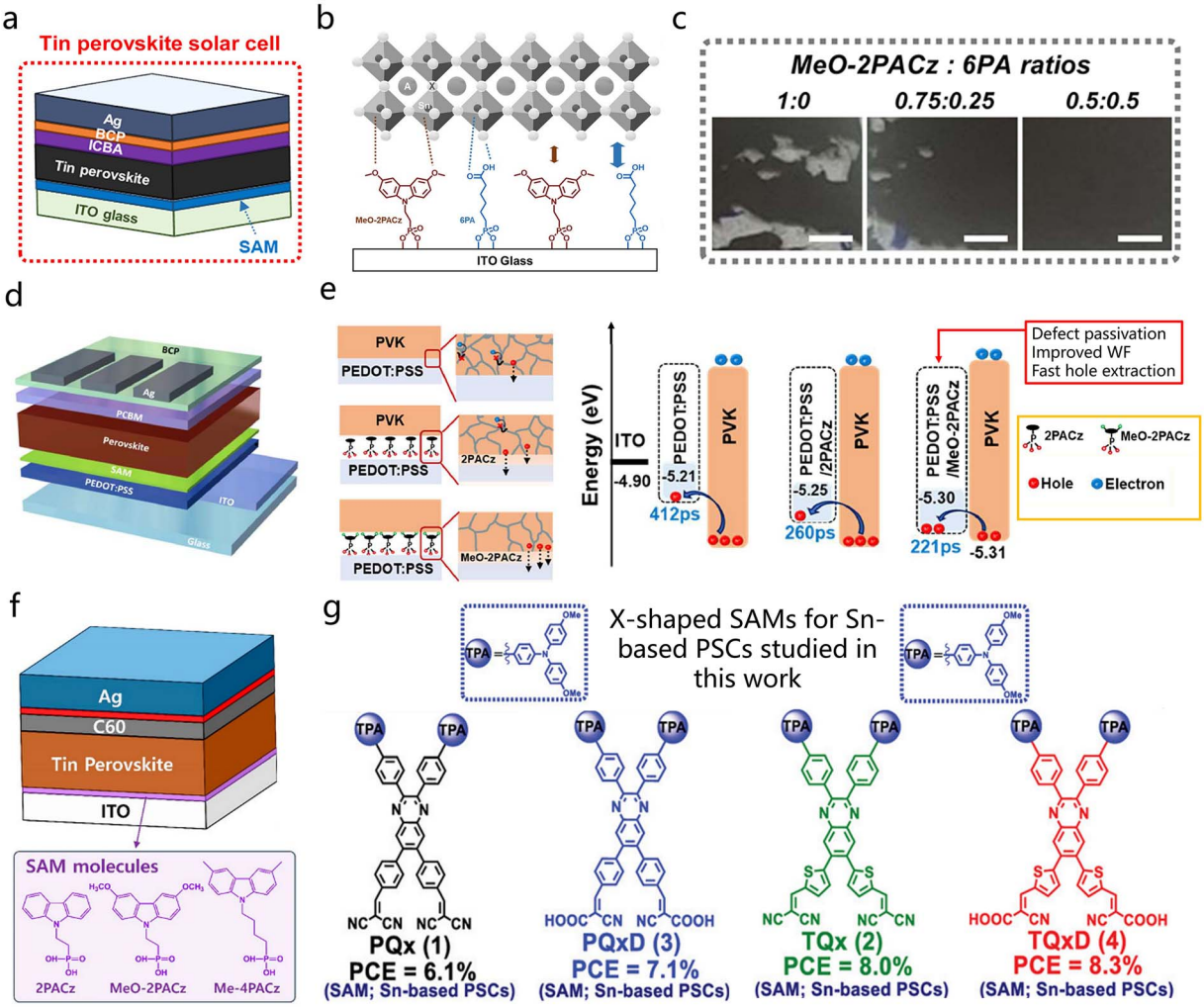

Fig. 19 (a) Device structure of TPSCs under investigation.[76] Copyright 2024, the American Chemical Society. (b) Schematic of the interaction between Sn perovskite and different SAM molecules.[76] Copyright 2024, the American Chemical Society. (c) Photographs of Sn-based perovskite films obtained on SAMs at different MeO-2PACz/6PA molar ratios (scale bar: 3 mm).[76] Copyright 2024, the American Chemical Society. (d) Schematic of the p-i-n device structure.[183] Copyright 2023, Elsevier. (e) Interactions between SAMs, anchoring groups, and PEDOT:PSS at the HTL/perovskite layer interface, and the interaction of the terminal group (methoxy) of MeO-2PACz with perovskite and work function changes and energy level alignment.[183] Copyright 2023, Elsevier. (f) Schematic of the device structure of Sn-based PSCs showing two perovskite deposition methods and the chemical structures corresponding to three SAM molecules.[184] Copyright 2021, the American Chemical Society. (g) Chemical structures of the SAMs: PQx (1), TQx (2), PQxD (3), and TQxD (4).[185] Copyright 2023, Wiley-VCH GmbH.

oxygen donor originating from the methoxy (CH_3O^-) terminal group of MeO-2PACz interacts chemically with the Sn halide octahedra. This helps to inhibit the oxidation of Sn^{2+} states as well as the perovskite's defect concentration to some extent, increasing the PCE of TPSCs to 12.16%.[183] A two-step method can also be used to prepare SAMs. Song *et al.* attached SAMs to the ITO substrate using a MeO-2PACz solution. The phosphonic acid in the molecule firmly anchors the SAM molecules to the ITO surface through ester linkages or hydrogen bonds, while the spacer groups help their dense packing through lateral interactions, and the terminal groups are responsible for surface properties and interactions with perovskite (Fig. 19f). The dipole moment of the SAM determines the energy levels of its CBM and VBM relative to vacuum, thereby improving charge transfer and enhancing the PCE of perovskite (6.5%).[184] Additionally, Shakil *et al.* constructed a series of X-shaped D–A organic SAM molecules with quinoxaline fragments as the core species (Fig. 19g). These molecules have two anchoring groups (CN or/and –COOH) at both ends of the quinoxaline core, which have a strong anchoring ability to the ITO surface, forming better molecular alignment on the surface, while ordinary single linear dyes cannot align on the surface. This unique X-shaped molecular design will help guide photoinduced charge transfer, thereby increasing the hole injection degree of ITO.[185]

3.3.1.3 Hydroxy-based molecules. Hydroxyl-containing molecules are a class of polar molecules with hydroxyl (–OH) functional groups, which can generate coordination bonds with uncoordinated Sn^{2+} ions in perovskites through the lone pair of electrons on the oxygen atom, effectively passivating surface defects and those at grain boundaries of perovskites.

 This journal is © The Royal Society of Chemistry 2025

Published on 01 August 2025. Downloaded on 1/24/2026 5:38:31 AM.

Additionally, the dipole moment induced by the hydroxyl group can modulate the interfacial alignment of energy level, reducing non-radiative recombination losses. Common hydroxyl-containing molecules used in TPSCs include alcohols, acids, and aldehydes.[186]

Zhao *et al.* performed a post-treatment on the perovskite surface using ethanol (EtOH). The treated HTL exhibited the largest PEDOT crystal size and the smallest PSS crystal size, with better molecular alignment (Fig. 20a and b). Meanwhile, the energy gap in the middle of the HTL and the valence band of the perovskite was reduced, achieving better energy level alignment at the heterojunction interface, which is favorable for charge carrier transport. The PCE of the perovskite device reached 13.32%.[187] Meanwhile, Ren *et al.* introduced multifunctional acetaminophen (ACE) to modulate the interface in the middle of the perovskite layer and the HTL. The $FASnI_3$ surface has a high density of defects, and Sn^{2+} and Sn vacancies can exacerbate the oxidation of Sn^{2+}, leading to severe non-radiative recombination. The multifunctional ACE can act as a bridge in the middle of the perovskite film and PEDOT:PSS, playing a positive role in reducing non-radiative recombination at the interface (Fig. 20c). The PCE of the TPSC device reached 12.04% and maintained 99% of its starting PCE after kept in N_2 for over 2100 hours.[188] In addition, Liu *et al.* introduced polyethylene glycol (PEG) as an interlayer material at the perovskite/HTL interface. Upon the inclusion of PEG in the PEDOT:PSS solution, it interacted with PSS's SO_3H^+ groups, diminishing the coulombic interaction in the middle of PEDOT:PSS and PEDOT. Meanwhile, PEG ensured good energy level alignment between the HTL and the perovskite layer, reducing non-radiative

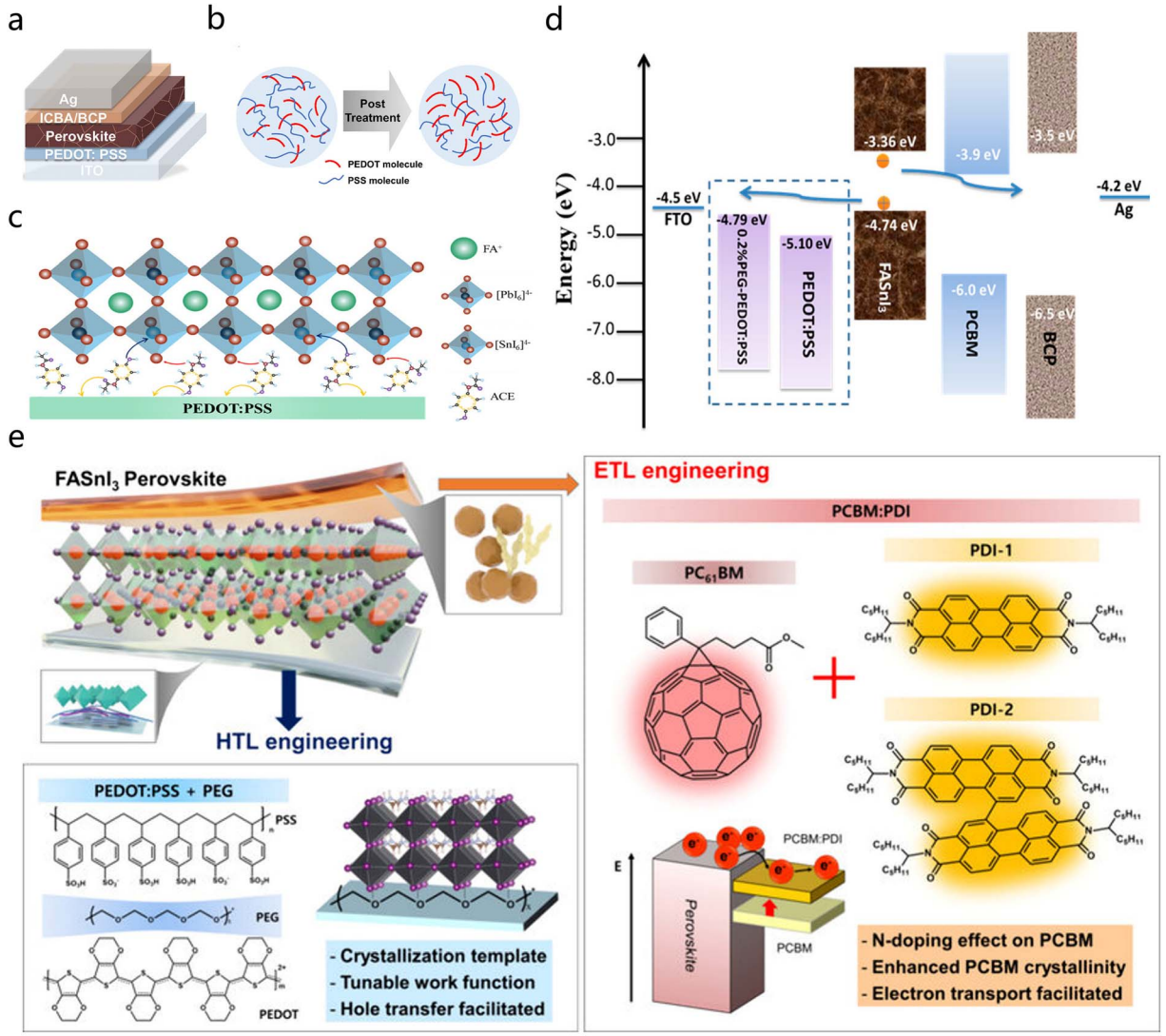

Fig. 20 (a) Schematic of the changes in the PEDOT:PSS film after the post-treatment process.[187] Copyright 2025, the Royal Society of Chemistry. (b) Schematic of the effect of the post-treatment.[187] Copyright 2025, the Royal Society of Chemistry. (c) Schematic of the interaction between ACE and PEDOT: PSS as well as the perovskite layer.[188] Copyright 2024, the American Chemical Society. (d) Energy diagram for $FASnI_3$ PSCs.[189] Copyright 2018, the American Chemical Society. (e) Schematic of the interlayer modification and doping mechanism.[191] Copyright 2024, the American Chemical Society.

Published on 01 August 2025. Downloaded on 1/24/2026 5:38:31 AM.

recombination losses (Fig. 20d).[189] Another strategy for adjusting the PEDOT:PSS's work function was to insert a PEDOT:PSS layer positioned in the middle of the ITO electrode and PEDOT:PSS regulated with sulfamic acid (SA), forming a pseudo-bilayer structure of polystyrene/sulfonic acid-modified polystyrene (PS/SA@PS) HTL to safeguard the ITO electrode against the higher acidic sulfonic acid-modified polystyrene (SA@PS). SA induces charge shielding *via* zwitterionic interactions, reconfiguring the PEDOT chain conformation to enhance the mobility as well as the conductivity of the HTL, facilitating easier extraction and movement of holes. Simultaneously, increasing the number of PSS chains at the HTL surface increases the work function of PEDOT:PSS to align with the valence band of the perovskite absorber layer ($FA_{0.98}EDA_{0.01}SnI_3$), creating a more hydrophilic surface for the deposition of high-performance Sn-based perovskite films.[190] In the latest research, Na *et al.* incorporated PEG and perylene diimide (PDI) into the HTL, which improved energy-level alignment and carrier transport, achieving a PCE of 10.1% in TPSCs.[191]

3.3.1.4 Inorganic salts. Inorganic salts, an important class of interfacial modification materials, play multiple crucial roles. The most commonly used inorganic salt in TPSCs is the SnO_x family. SnO_x can serve as an efficient electron transport layer, with its suitable energy level position (conduction band at approximately −4.3 eV) forming a good alignment of energy level with Sn-based perovskite materials, significantly enhancing the electron extraction PCE and reducing interfacial recombination. In addition, SnO_x exhibits excellent chemical stability, effectively blocking the penetration of moisture and oxygen, thereby significantly elevating the long-term stability of devices.[192]

Chiang *et al.* investigated the bilayer material (SnO/PDTON) as the HTL for TPSCs. Thermally evaporated SnO has the advantages of high hole mobility, good transparency, and tunable frontier orbital energy levels, while the bipolar polymer PDTON (with amine and ether groups in its side chains) is commonly used as a co-HTL, passivator, and interfacial modifier. One reason for the superior performance of SnO/PDTON over PEDOT is that PDTON can act as an interfacial bridge between the perovskite and SnO (Fig. 21a), promoting the alignment of energy level in the middle of the SnO/PDTON and the perovskite film (Fig. 21b).[193] In addition, to prevent the acidic nature of PEDOT:PSS from damaging the Sn-based perovskite layer, Takeshi *et al.* introduced an inorganic hole scavenger, nano-SnO_2. Holes in the Sn-based perovskite layer's valence band are ejected through the deeper valence band of C_{60} as well as captured through the mid-gap states of P-Nano SnO_x, thereby reducing nano-SnO_2 to SnO_x ($x < 2$) nanoparticles on the surface as the HTL for TPSCs (Fig. 21d). P-Nano SnO_x Fermi level is deeper than that of nano-SnO_2 relative to the bandgap center, indicating that the p-type character of P-Nano SnO_x is boosted upon contact with the Sn-based perovskite (Fig. 21c), thereby increasing hole mobility and achieving a PCE of 9.77%.[194] Furthermore, Hayase *et al.* fabricated bipolar P-SnO_x with a Sn-to-oxygen ratio of 1/1.77. They determined the perovskite valence band by X-ray photoelectron spectroscopy (XPS) and UV-vis spectroscopy, finding that the deeper Fermi level in P-SnO_x results in more Sn^{2+} compared to C-SnO_x, indicating that P-SnO_x can suppress Sn^{2+} oxidation (Fig. 21f). Combining P-SnO_x directly as the HTL for perovskite solar cells (S-PSCs) with T-SnO_x can increase the PCE of S-PSCs to over 14% (Fig. 21e).[77] In addition to SnO_x-based inorganic salts, other inorganic salts such as fluoride ions (F^-), thiocyanate ions (SCN^-), and other oxides have been explored.[114,195,196] For example, Hahn *et al.* first introduced nitrogen-doped graphene oxide (N_xGO) into the HTL and interfacial layer (IL) of Sn-PSCs, aiming to develop stable and efficient inverted TPSCs. The energy levels of N_xGO match well with those of Sn-based perovskites, facilitating charge extraction and reducing non-radiative recombination.[197]

3.3.2 ETL/PVSK interface. Interface engineering of the ETL/PVSK plays a crucial role in optimizing the energy level alignment, reducing the electron extraction barrier, and passivating perovskite surface defects. Researchers have primarily employed interface modification strategies (such as fullerenes and their derivatives, organic salts, and inorganic salts) and ETL replacements (such as SnO_2, Nb_2O_5, and metal sulfides).[198]

3.3.2.1 Fullerene and derivatives. The cost of C_{60} and its derivatives is higher than that of other ETL materials, yet they possess numerous significant advantages. Regarding energy level alignment, the LUMO energy level of the fullerene family matches the conduction band of perovskite and exhibits high electron mobility. Moreover, the nanoscale spherical shape of the fullerene family enables their effective distribution on the surface of the light absorber, thereby creating highly selective contacts for electron extraction.[199]

In TPSCs, the functions that the ETL needs to fulfill are the efficient extraction as well as transport of electrons from the perovskite absorption film toward the electrode, while blocking the holes' movement. This selective charge extraction minimizes recombination losses in the solar cell and maximizes PCE. The most common ETMs are C_{60} and its derivatives, including C_{60}, ICBA, PCBM ([6,6]-phenyl-C_{61}-butyric acid methyl ester), and CPTA (pyrrolidinetricarboxylic acid). CPTA is an early fullerene-based ETL material applied in PSCs. Studies have shown that SnO_2 alone as an ETL tends to cause non-radiative recombination between electrons and holes. When CPTA and SnO_2 are used together as an ETL, CPTA acts as an electron donor, coordinating with the Sn atoms in SnO_2 to form a Lewis adduct. This results in an energy barrier at the SnO_2/CPTA interface that effectively suppresses charge recombination (blocking holes), ultimately achieving a PCE of 7.4% (Fig. 22a).[172] PCBM is a commonly used ETL material at present, with high electron mobility that enables efficient extraction as well as transport of photogenerated electrons from the perovskite film, reducing recombination losses. Sun *et al.* synthesized four multidentate fullerene molecules on PCBM-based devices: FM3, FM4, FM5, and FM6 (containing 3, 4, 5, and 6 diethylmalonate groups, respectively) as interfacial layers. These fullerenes' functional groups lead to a shallower LUMO energy level, enhancing interfacial chemical interactions. Among them, FM5 achieved the highest PCE of 15.05% (Fig. 22b).[200] Similarly, Chen *et al.* added a fullerene dimer C_{60}BB as an intermediate layer on top of PCBM as the ETL material to

 This journal is © The Royal Society of Chemistry 2025

Published on 01 August 2025. Downloaded on 1/24/2026 5:38:31 AM.

optimize the energy level alignment. Meanwhile, C_{60}BB reduced the potential difference between the perovskite film and the ETL from 85 mV to 47 mV. This smaller potential difference helps to reduce V_{OC} loss, thereby improving the device performance, ultimately achieving a PCE of 16.05% (Fig. 22c and d).[17] Unlike C_{60} and PCBM, ICBA has a shallower energy level, which delivers a greater maximum attainable voltage while suppressing remote doping of iodide and decreasing interfacial carrier recombination. As shown in Fig. 22e, compared to the band offset of PCBM, a shallower LUMO energy level is in ICBA, ultimately increasing the device PCE to 12.4%.[201] However, ICBA still has some drawbacks that need to be regulated through various methods. ICBA has poor control of energetic disorder, resulting in the elongation of its band tail, thereby limiting the devices' photovoltage and reducing the PCE. Studies have shown that ICBA can be improved by optimizing the selection of solvents and annealing temperatures. Mixing CB with TCB (chlorobenzene/1,2,4-trichlorobenzene) as a solvent can reduce the energetic disorganization of the deposited ICBA film to below 80% of that of a pure CB solution. Boosting the ICBA film's annealing temperature from 70 °C toward 100 °C can further reduce energetic disorder (Fig. 22f and g).[36] In addition to the fullerene and derivatives, Sun *et al.* discovered four regioisomers of diethylmalonate C_{60} bisadduct (DCBA) that can react with Sn^{2+}, which is beneficial for interfacial charge extraction. Among the four isomers, the champion device achieved a PCE of 14.30%. Additionally, Yang *et al.* implemented a strategy leveraging steric hindrance to synthesize single isomers of C_{60}- and C_{70}-based diethylmalonate-functionalized bisadducts (C_{60}BB and C_{70}BB) as ETLs. They also treated the fullerene-dimer films with different solvents to enhance the

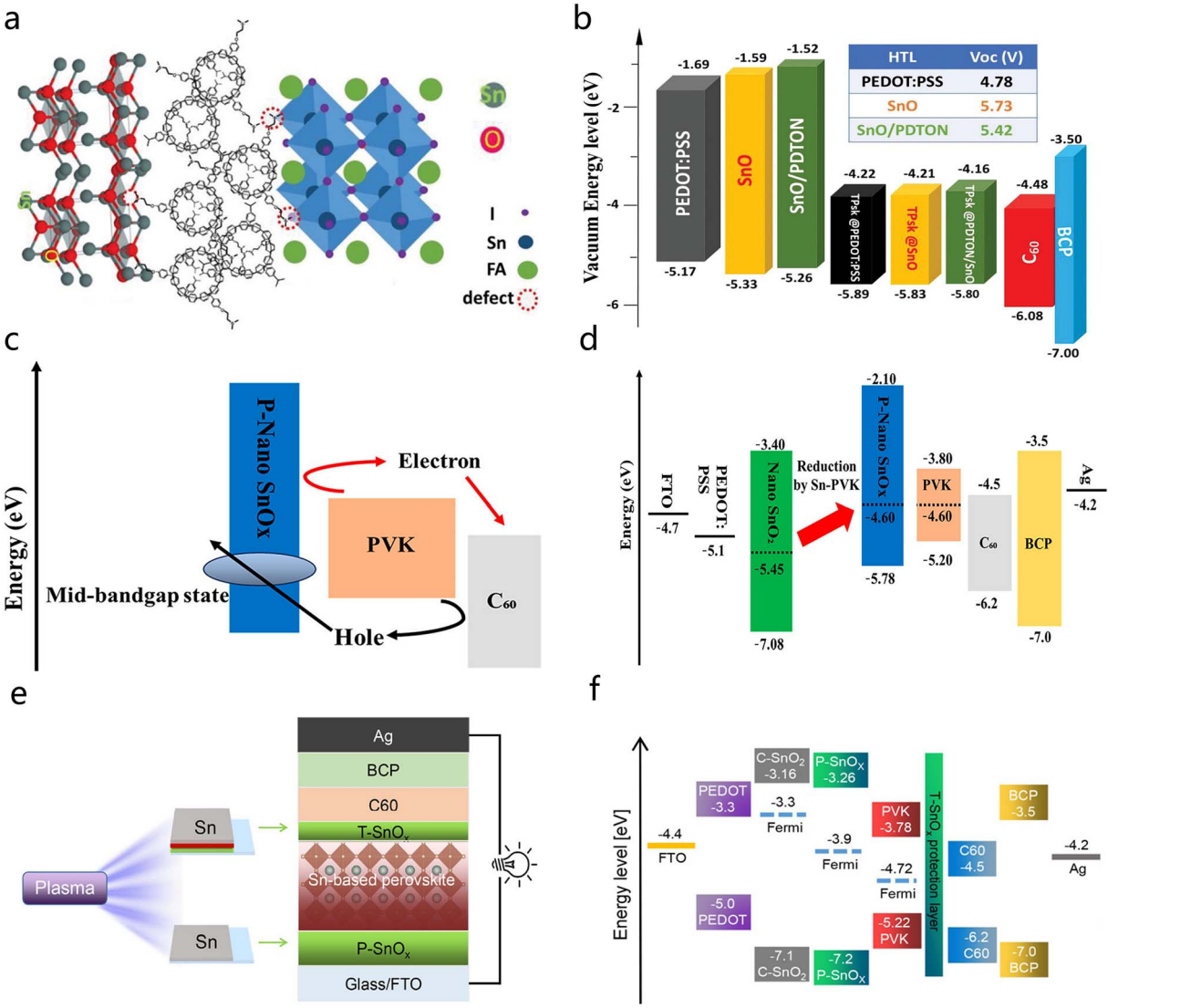

Fig. 21 (a) Schematic of the PDTON film as a linker and passivation agent for SnO and TPSK.[193] Copyright 2024, Wiley-VCH GmbH. (b) Frontier orbital energy levels of HTLs.[193] Copyright 2024, Wiley-VCH GmbH. (c) Working mechanism of P-Nano SnO_x as HTL.[194] Copyright 2023, the American Chemical Society. (d) Energy diagram of Sn-PSC.[194] Copyright 2023, the American Chemical Society. (e) Plasma-assisted strategy (P-SnO_x) for the *in situ* fabrication of bipolar SnO_x.[77] Copyright 2022, the American Chemical Society. (f) Energy level diagram of S-PSC.[77] Copyright 2022, the American Chemical Society.

Published on 01 August 2025. Downloaded on 1/24/2026 5:38:31 AM.

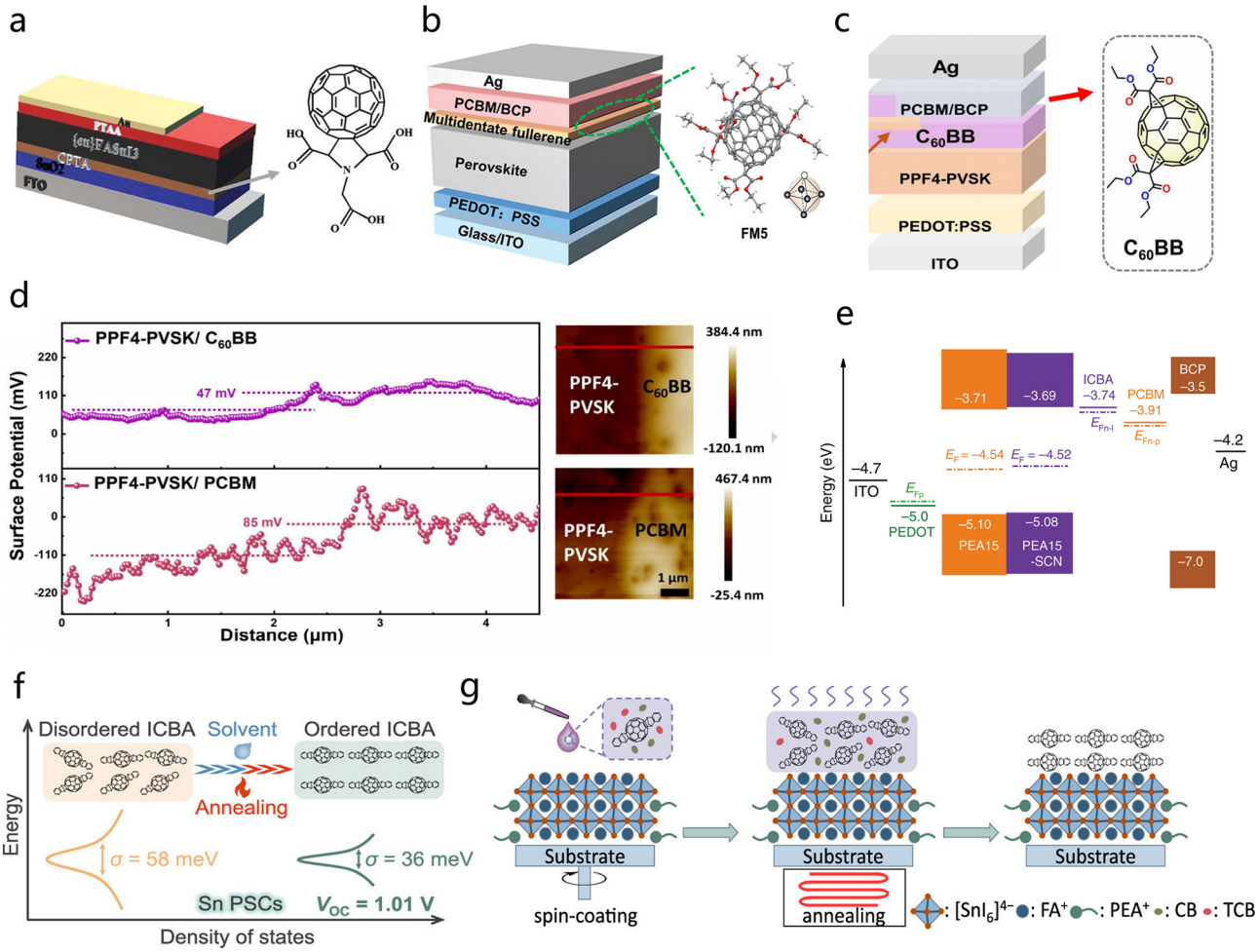

Fig. 22 (a) Schematic of the device structure and molecular structure of CPTA.[172] Copyright 2019, Wiley-VCH GmbH. (b) Single-crystal structure of FM5, and schematic of the device structure of TPSC.[200] Copyright 2017, Elsevier. (c) Molecular structure of C_{60}BB, schematic of the interlayer device, and surface potential distribution of different samples.[17] Copyright 2025, Wiley-VCH GmbH. (d) Surface potential distribution across various samples.[17] Copyright 2025, Wiley-VCH GmbH. (e) Energy level diagram of $PEA_xFA_{1-x}SnI_3$. The dashed lines represent the quasi-Fermi levels of ICBAs (E_{Fn-I}), PCBM (E_{Fn-P}), and PEDOT (E_{Fp}).[201] Copyright 2020, Springer Nature. (f) Effect of chlorobenzene solvent on ICBA.[36] Copyright 2023, the American Chemical Society. (g) Schematic of the ICBA film preparation process.[36] Copyright 2023, the American Chemical Society.

electron mobility. C_{60}BB and C_{70}BB achieved PCEs of 14.51% and 14.28%, correspondingly.[202]

3.3.2.2 Organic salts. Organic salts can bind with uncoordinated ions (such as Sn^{2+} or I^-) at the surface or perovskite structures' grain boundaries, reducing the density of defect states and suppressing non-radiative recombination, thereby enhancing V_{OC} and the fill factor (FF). Additionally, organic salts can modulate the energy level alignment between perovskites and charge transport layers, improving charge extraction and transport PCE and reducing energy losses at the interface. The introduction of organic salts can be categorized into two types: precursor solution treatment and post-treatment.[203]

Shi *et al.* incorporated a molecular dipole, 4-fluorophenethylamine hydrobromide (FPEABr), into $FASnI_3$ PSCs to regulate the energy level alignment in the middle of the perovskite layer and the ETL. The presence of FPEABr resulted in an upward shift of the perovskite layer's VBM and CBM by 0.10 eV due to interfacial dipoles, making the perovskite-ICBA (indene-C_{60} bisadduct) energetically favorable for electron transport, ultimately achieving a PCE of 15.7% (Fig. 23a).[204] Cao *et al.* introduced an n-type conjugated non-fullerene molecule, IO-4Cl, to modify the ETL layer. IO-4Cl, with its electron-rich groups (C=O), can neutralize defects in Sn-based perovskite layers by Lewis acid–base coordination, effectively suppressing non-radiative recombination. The existence of electron-rich and electron-poor regions around the molecule enhances its passivation effect. Additionally, IO-4Cl can decrease the Sn-based perovskite layer's band edges, greatly optimizing the interfacial energy level matching with its nearby ETL layer. The LUMO energy level of this molecule lies between the perovskite layer's CBM and the ETL's LUMO energy level, providing additional enhancement of the convenience of charge extraction as well as transport (Fig. 23b).[205] Ultimately, TPSCs incorporating IO-4Cl achieved a top PCE of 11.49% with an increased V_{OC} by

 This journal is © The Royal Society of Chemistry 2025

Published on 01 August 2025. Downloaded on 1/24/2026 5:38:31 AM.

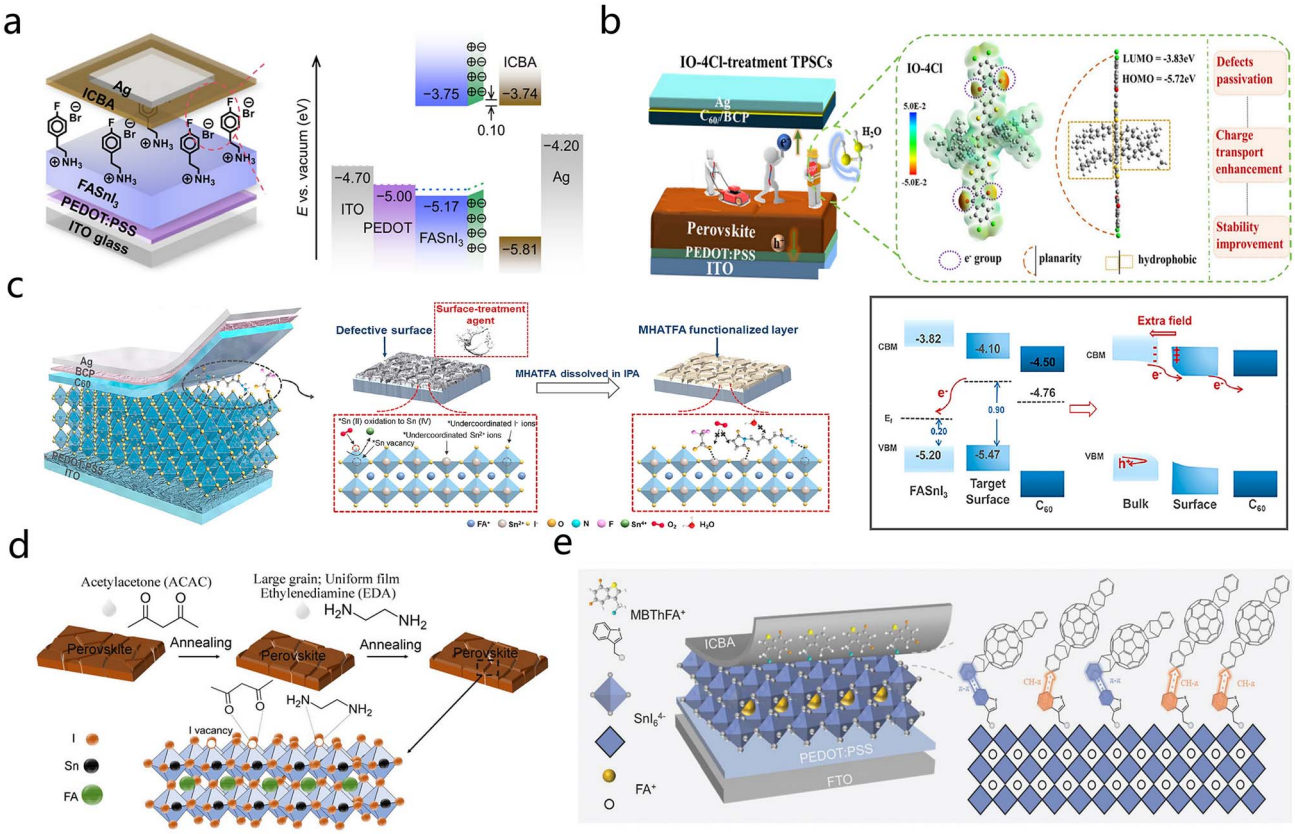

Fig. 23 (a) Schematic of the inverted solar cell structure and energy levels. The interfacial dipoles (green) are assumed to be located between the perovskite and the electron transport layer, increasing the energy of the band edges by 0.10 eV.[204] Copyright 2024, the American Chemical Society. (b) Schematic of the fabrication process and working mechanism of TPSCs using IO-4Cl.[205] Copyright 2023, Wiley-VCH GmbH. (c) Schematic of the surface reconstruction strategy and the passivation protection mechanism of MHATFA, and the energy level scheme based on UPS spectra (left) and the formation of a back-surface field on the perovskite surface after surface treatment (right).[208] Copyright 2022, the American Chemical Society. (d) Schematic of the passivation mechanism of perovskite by ACAC and EDA.[35] Copyright 2022, Wiley-VCH GmbH. (e) Schematic of the partial device structure and the charge bridge path.[209] Copyright 2024, Wiley-VCH GmbH.

100 mV. Studies have shown that dicyanomethanone (DAMN)'s push–pull effect promotes rapid electron transfer from the $FASnI_3$ layer toward C_{60}.[206] The DAMN molecule, with its two strong electron-withdrawing groups (CN), effectively extracts electrons from the perovskite film (pull effect), while the good energy level matching in the middle of the $FASnI_3$–DAMN and C_{60} layers facilitates electron transfer from the perovskite film to C_{60} (push effect). DAMN increased the final PCE of TPSCs to 8.11%. Furthermore, the incorporation of cyanoacetohydrazide (CAH) optimizes the band alignment and interfacial charge extraction at the ETL/PVSK interface by suppressing the formation of 2D phases. In addition, the introduction of multifunctional groups within CAH further enhances structural compactness and reduces defect density, thereby inhibiting non-radiative recombination and facilitating charge transport. These collective improvements effectively extend the charge-carrier lifetime from 36.48 ns to 150.99 ns.[117] Additionally, Ning *et al.* incorporated 1% poly(methyl methacrylate) (PMMA) into the ICBA precursor to fabricate the ETL. The polar C=O groups in PMMA interact strongly with Sn^{2+} ions on the perovskite surface, generating a robustly adherent electron-transport layer that ensures efficient charge transfer across the ETL/PVSK interface. As a result, TPSCs delivered a power-conversion efficiency of 15.8%.[207]

Unlike precursor treatment, post-treatment refers to the modification of the perovskite film after its formation. Li *et al.* designed a surface regulation strategy grounded in 6-maleimidohexylhydrazine trifluoroacetate (MHATFA) to reconfigure the $FASnI_3$ films' surface structure, controlling the Fermi level as well as passivating defects. Initially, the ion-pairing agent provides passivating cations and anions to eliminate the surface enriched with charged defects. Meanwhile, the evolution of electronic states leads to a shift of the n-type Fermi level towards the surface, generating an additional back-surface field that influences electron extraction. The combined effect significantly enhanced the device's PCE (13.64%) (Fig. 23c).[208] Additionally, Zhang *et al.* proposed a simple and universal post-treatment strategy involving passivation in sequence using acetylacetone (ACAC) and ethylenediamine (EDA). Fig. 23d indicates that ACAC is capable of reducing trap density and boosting short circuit current, whereas EDA bonds under-coordinate Sn as well as modulate energy levels (enhanced open-circuit voltage). The final PCE of the perovskite devices exceeded 13%.[35] Studies have shown that adding 3-

Published on 01 August 2025. Downloaded on 1/24/2026 5:38:31 AM.

aminomethylbenzo[*b*]thiophene (3-AMBTh) to the perovskite layer is a novel method for constructing charge transfer pathways. The reaction of 3-AMBTh with FA^+ on the perovskite surface selectively inhibits iodine vacancy defect formation, leading to reduced trap concentration. Moreover, the remaining aromatic rings on the surface engage in effective π–π stacking interactions with the subsequently deposited ICBA, promoting charge transfer at the interface. Leveraging the possibility of charge transfer pathways, the device achieved a PCE as high as 14.53% (Fig. 23e). In the latest research, Yang *et al.* introduced dihydropiperazine iodide (PDI) and ferrocene (Fc) to the PVSK/ETL interface. The PD^+ molecules interact with FA^+ to form interfacial dipoles, while Fc forms π–π conjugation with C_{60}. These effects significantly enhance electron extraction at the PVSK/ETL interface and reduce energy loss. Consequently, the PCE of the TPSCs increased from 10.62% to 13.65%.[43]

3.3.2.3 Inorganic salts. Inorganic salts, with their high chemical stability, tunable energy level structures, and interfacial passivation properties, contribute significantly to interfacial regulation. The introduction of metal halide salts can effectively modulate the energy level matching in the middle of the perovskite film and the charge transport layer, reducing interfacial energy losses. Meanwhile, the cations in inorganic salts can combine with uncoordinated Sn^{2+} defects on the perovskite surface, suppressing Sn^{2+}'s oxidation and reducing interfacial non-radiative recombination. Their dense crystalline structures can also block moisture penetration, enhancing the device stability.[210] Common inorganic salts include metal oxides such as SnO_x and metal salts such as ZnS and In_2S_3.

SnO_x can serve as an antioxidant material in interfacial regulation. Wang *et al.* employed a simple and rapid plasma-assisted strategy for the *in situ* fabrication of bipolar SnO_x. SnO_x (T-SnO_x) on top, consisting of SnO_2 and Sn metal, acts as a regulator and protective film for perovskites, decreasing Sn^{4+} to Sn^{2+}, with a maximum device performance of 13.41% (Fig. 24a).[77] Yokoyama *et al.* introduced a novel ETL material, Nb_2O_5. Nb_2O_5 addresses the conduction band offset (CBO) issue in TPSCs caused by low electron affinity. Compared to other ETL materials such as TiO_2, Nb_2O_5 has a near-zero conduction band offset, increasing the gap between the CBM and the VBM, thereby reducing the electron–hole recombination rate (Fig. 24b), achieving a PCE of 5.1%.[175] Li *et al.* found that the poor performance of TPSCs might be due to oxygen vacancies as well as significant energy levels in metal oxides. Therefore, they proposed a metal chalcogenide electron transport layer, particularly $Sn(S_{0.92}Se_{0.08})_2$, which bypasses the desorption of oxygen molecules and hinders Sn^{2+} from being oxidized. Consequently, the V_{OC} value of TPSCs containing $Sn(S_{0.92}Se_{0.08})_2$ increased from 0.48 V toward 0.73 V, as well as the PCE improved from 6.98% toward 11.78%. Studies have shown that metal chalcogenides can serve as ETL materials, with advantages such as matching energy levels with Sn perovskites and enhancing electron mobility (Fig. 24c).[211] Ke *et al.* discovered that ZnS could be used to encapsulate TiO_2, forming a cascaded conduction band structure in the ETL, facilitating electron extraction from $FASnI_3$ to TiO_2, thereby reducing interfacial charge recombination and promoting electron transfer (Fig. 24d and e).[171] Widianto *et al.* introduced low-temperature In_2S_3 as an ETL in SCAPS-1D simulations. Theoretical simulations showed that this approach can reduce the density of interfacial defects at the ETL/perovskite interface, thereby achieving a high-performance photovoltaic PCE (Fig. 24f).[212]

All the key information on the structural engineering of Sn-based PSCs in this section is summarized in Table 3.

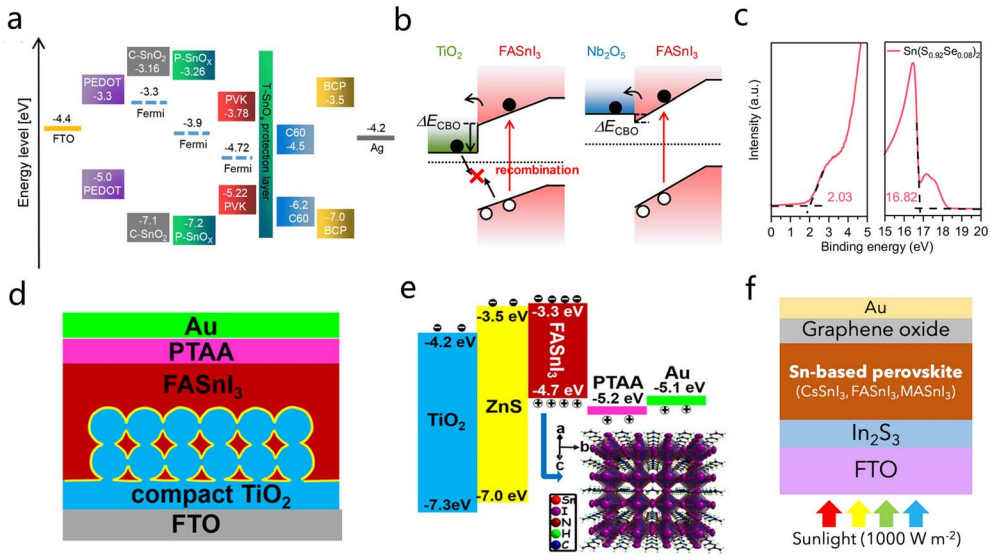

Fig. 24 (a) Energy level diagram of PSCs incorporating SnO_x as the ETL.[77] Copyright 2022, the American Chemical Society. (b) Conceptual illustration of the band profile at the ETL/perovskite layer interface.[175] Copyright 2020, the American Chemical Society. (c) $Sn(S_{0.92}Se_{0.08})_2$ ETL shows the shallowest CBM position, highlighting its potential as the preferred ETL candidate for clamp-type TPSCs.[211] Copyright 2024, Springer Nature. (d) Schematic of the device structure of $FASnI_3$.[171] Copyright 2016, the American Chemical Society. (e) Band diagram of $FASnI_3$, and schematic of the crystal structure of the perovskite absorber.[171] Copyright 2016, the American Chemical Society. (f) Schematic of TPSCs incorporating In_2S_3.[212] Copyright 2024, Springer Nature.

 This journal is © The Royal Society of Chemistry 2025

Published on 01 August 2025. Downloaded on 1/24/2026 5:38:31 AM.

Table 3 Summary of the device performance and strategy of Sn-based perovskites by interface engineering

Strategy/CTL material	Device structure		V_{OC} (V)	J_{SC} (mA cm^{-2})	FF (%)	PCE (%)	Shelf stability	Ref.
TiO_2–ZnS	FTO/TiO_2/$FASnI_3$/PTAA/Au	n-i-p	0.38	23.09	60.01	5.27	—	171
PbSCN	ITO/PEDOT:PSS/$MASnI_3$/PCBM/PEI/Al	p-i-n	0.50	17.69	64.00	6.03	—	213
TPE	FTO/TiO_2/{en}$FASnI_3$/TPE/Au	n-i-p	0.46	22.39	68.01	7.23	—	173
PEG	FTO/PEDOT:PSS/$FASnI_3$/PCBM/BCP/Ag	p-i-n	0.37	21.30	63.60	5.12	Retain 95% of the initial PCE after 30 d in N_2 without encapsulation	189
LiF	ITO/PEDOT:PSS/(PEA,FA)SnI_3/C_{60}/BCP/Ag	p-i-n	0.47	20.07	74.00	6.98	Retain 88% of the initial PCE after 5 d in N_2 without encapsulation	114
EDA	ITO/PEDOT:PSS/$FASnI_3$/C_{60}/BCP/Ag	p-i-n	0.59	21.11	73.00	10.18	—	214
CPTA	FTO/SnO_2/{en}$FASnI_3$/PTAA/Au	n-i-p	0.72	16.45	65.00	7.40	Retain 88% of the initial PCE after 100 h in air without encapsulation	172
BDT	FTO/TiO_2/{en}$FASnI_3$/BDT/Au	n-i-p	0.50	22.41	68.21	7.59	—	174
PEABr	ITO/PEDOT:PSS/$FASnI_3$/PCBM/BCP/Al	p-i-n	0.54	22.64	64.00	7.86	—	215
ICBA	ITO/PEDOT:PSS/$FA_{0.9}PEA_{0.1}SnI_3$/ICBA/BCP/Al	p-i-n	0.65	16.88	64.00	7.05	Retain 93% of the initial PCE after 400 h in Ar without encapsulation	216
ICBA	ITO/PEDOT:PSS/$FASnI_3$/ICBA/BCP/Ag	p-i-n	0.94	17.40	75.00	12.40	Retain 90% of the initial PCE after 3800 h in air with encapsulation	201
Nb_2O_5	ITO/Nb_2O_5/$FASnI_3$/PTAA/Au	n-i-p	0.42	22.80	52.00	5.10	—	175
D-Sorbitol	ITO/PEDOT:PSS/$PEA_{0.1}(FA_{0.75}MA_{0.25})_{0.9}SnI_3$/ICBA/BCP/Ag	p-i-n	0.83	19.24	67.00	10.46	Retain 80% of the initial PCE after 750 h in N_2 without encapsulation	165
R-MBA	ITO/PEDOT:PSS/$FASnI_3$/C_{60}/BCP/Ag	p-i-n	0.65	22.56	73.10	10.73	Retain 90% of the initial PCE after 120 d in N_2 without encapsulation	179
No HTL	ITO/$FASnI_3$/PCBM/BCP/Ag	p-i-n	0.68	23.16	67.10	10.58	—	217
MeO-2PACz	ITO/MeO-2PACz/(FA,EDA)SnI_3/C_{60}/BCP/Ag	p-i-n	—	—	—	6.50	Retain 80% of the initial PCE after 1900 h in N_2 without encapsulation	184
DAMN	ITO/PEDOT:PSS/$FASnI_3$/C_{60}/BCP/Ag	p-i-n	0.65	16.62	75.00	8.11	—	206
3FEAI	ITO/PEDOT:PSS/$MASnI_3$/C_{60}/BCP/Al	p-i-n	0.62	22.11	68.47	9.34	Retain 90% of the initial PCE after 500 h in N_2 without encapsulation	195
PEASCN	ITO/PEDOT:PSS/$FASnI_3$/PCBM/BCP/Ag	p-i-n	0.67	22.16	65.30	9.65	—	218
$EDAFa_2$	ITO/PEDOT:PSS/$FASnI_3$/C_{60}/Li/Ag	p-i-n	0.60	23.71	66.21	9.40	Retain 95% of the initial PCE after 1960 h in N_2 without encapsulation	219
2PACz	FTO/HTL/$EDA_{0.01}(GA_{0.06}(FA_{0.8}Cs_{0.2})_{0.94})_{0.98}SnI_2Br$/$C_{60}$/BCP/Ag	p-i-n	0.74	16.22	73.00	8.66	Retain over 80% of the initial PCE after 48 h in air without encapsulation	220
KSCN	FTO/PEDOT:PSS/$FA_{0.75}MA_{0.25}SnI_2Br$/ICBA/Bphen/Ag	p-i-n	0.82	20.88	64.00	11.17	Retain 80% of the initial PCE after 1200 h in N_2 without encapsulation	196
SA	ITO/PEDOT:PSS/$FA_{0.98}EDA_{0.01}SnI_3$/	p-i-n	0.64	23.14	71.00	10.49	Retain 95% of the initial PCE after 2000 h in N_2 without encapsulation	190
N_xGO	FTO/PEDOT:PSS–$N_{0.12}$GO/Al_2O_3–$N_{0.12}$GO/Sn–PS:$N_{0.12}$GO/PCBM/BCP/Au	p-i-n	0.96	21.21	65.05	13.26	Retain 91% of the initial PCE after 60 d in Ar with encapsulation	197
PTAA	ITO/PTAA/$FASnI_3$/C_{60}/BCP/Ag	p-i-n	—	—	—	8.30	—	69
T-SnO_x	ITO/PEDOT:PSS/$FASnI_3$/C_{60}/BCP/Ag	p-i-n	0.75	24.34	74.00	13.41	Retain 90% of the initial PCE after 50 d in N_2 without encapsulation	77
GuaSCN	ITO/NiO_x/$FASnI_3$/ICBA/BCP/Ag	p-i-n	1.01	20.32	68.90	13.79	Retain the initial PCE after 1200 h in N_2 with encapsulation	221

This journal is © The Royal Society of Chemistry 2025

Published on 01 August 2025. Downloaded on 1/24/2026 5:38:31 AM.

Table 3 (*Contd.*)

Strategy/CTL material	Device structure		V_{OC} (V)	J_{SC} (mA cm^{-2})	FF (%)	PCE (%)	Shelf stability	Ref.
PCBH	ITO/PEDOT:PSS/$FASnI_3$/PCBH/BCP/Ag	p-i-n	0.63	19.77	73.96	9.21	Retain 80% of the initial PCE after 8 h in air without encapsulation	222
EABr	ITO/PEDOT:PSS/$MASnI_3$/PCBM/BCP/Ag	p-i-n	0.72	19.08	69.62	9.59	Retain 127% of the initial PCE after 50 d in N_2 without encapsulation	153
ACAC/EDA	ITO/PEDOT:PSS/$FASnI_3$/C_{60}/BCP/Ag	p-i-n	0.79	22.70	72.00	13.00	Retain 80% of the initial PCE after 70 d in N_2 without encapsulation	35
MHATFA	ITO/PEDOT:PSS/$FASnI_3$/C_{60}/BCP/Ag	p-i-n	0.80	23.10	72.99	13.64	Retain 76.4% of the initial PCE after 1000 h in air with encapsulation	208
CF_3PEAI	ITO/PEDOT:PSS/$FA_{0.75}MA_{0.25}SnI_{2.75}Br_{0.25}$/PCBM/BCP/Ag	p-i-n	0.55	18.26	—	10.35	Retain 70% of the initial PCE after 150 h in air without encapsulation	223
4AMPY$(Ac)_2$	ITO/PEDOT:PSS/(PEA,FA)SnI_3/PCBM/BCP/Ag	p-i-n	0.83	20.70	70.80	12.10	Retain 117% of the initial PCE after 2800 h in N_2 without encapsulation	183
FHZ	ITO/PEDOT:PSS/Sn–HaP/ICBA/BCP/Ag	p-i-n	0.87	19.58	75.20	12.87	Retain 62% of the initial PCE after 120 h in N_2 with encapsulation	224
ImAcCl	ITO/PEDOT:PSS/(PEA,EA,FA)SnI_3/PCBM/BCP/Ag	p-i-n	0.82	18.87	65.03	12.08	Retain over 95% of the initial PCE after 2500 h in N_2 without encapsulation	225
MeO-2PACz and 2PACz	ITO/PEDOT:PSS/$PEA_{0.15}FA_{0.75}MA_{0.10}SnI_2Br$/PCBM/BCP/Ag	p-i-n	0.93	16.60	—	12.16	Retain 70% of the initial PCE after 70 min in N_2 without encapsulation	184
D-Glucamine	ITO/PEDOT:PSS/$PEA_{0.1}(FA_{0.75}MA_{0.25})_{0.9}SnI_3$/Spiro-OMeTAD/Au	p-i-n	0.84	17.46	65.89	9.61	Retain over 80% of the initial PCE after 700 h in N_2 without encapsulation	226
ODAI	ITO/PEDOT:PSS/perovskite/C_{60}/BCP/silver/Ag	p-i-n	0.82	23.05	73.30	13.82	—	180
TQxD	ITO/TQxD/$FASnI_3$/C_{60}/BCP/Ag	p-i-n	0.57	21.05	68.80	8.30	Retain about 90% of the initial PCE after over1600 h in N_2 without encapsulation	185
ICBA	ITO/PEDOT:PSS/$PEA_{0.15}FA_{0.85}SnI_3$/ICBA/BCP/Ag	p-i-n	0.84	20.02	68.00	11.57	Retain over 80% of the initial PCE after 1300 h in N_2 without encapsulation	36
IO-4Cl	ITO/PEDOT:PSS/$FASnI_3$/C_{60}/BCP/Ag	p-i-n	0.68	22.26	75.91	11.49	Retain 90% of the initial PCE after 2500 h in N_2 without encapsulation	205
PNDI-BT	ITO/PEDOT:PSS/$FASnI_3$/ICBA/BCP/Ag	p-i-n	0.80	22.28	77.80	13.90	Retain 81% of the initial PCE after 1000 h in N_2 with encapsulation	198
FM5	ITO/PEDOT:PSS/$FASnI_3$/PCBM/BCP/Ag	p-i-n	0.86	24.54	71.06	15.05	Retain 90% of the initial PCE after 300 h in air without encapsulation	200
C_{60}BB/PPF4	ITO/PEDOT:PSS/$FASnI_3$/PCBM/BCP/Ag	p-i-n	0.86	26.17	71.35	16.05	—	17
ICBA	ITO/PEDOT:PSS/PEAX–$FASnI_3$/ICBA/BCP/Ag	p-i-n	0.68	20.60	65.00	9.10	—	38
F-PEABr	ITO/PEDOT:PSS/$FASnI_3$/ICBA/BCP/Ag	p-i-n	0.97	21.70	74.10	15.70	—	204
3-AMBTh	FTO/PEDOT:PSS/$FASnI_3$/ICBA/BCP/Ag	p-i-n	0.65	21.52	65.70	14.53	Retain 94.7% of the initial PCE after 1000 h in N_2 without encapsulation	209
$Sn(S_{0.92}Se_{0.08})_2$	ITO/$Sn(S_{0.92}Se_{0.08})_2$/$FASnI_3$/PTAA/Ag	n-i-p	0.73	22.28	72.68	11.78	Retain 95% of the initial PCE after 1632 h in N_2 without encapsulation	211
MXene	ITO/PEDOT:PSS/$PEA_{0.2}FA_{0.8}SnI_3$/ICBA/BCP/Ag	p-i-n	0.65	21.80	59.00	8.35	Retain 89% of the initial PCE after 450 h in N_2 without encapsulation	227
$Pb(SCN)_2$	ITO/PEDOT:PSS/$FA_{0.9}PEA_{0.1}SnI_3$/PCBM/PEI/Ag	p-i-n	0.70	22.37	77.14	12.04	Retain 99% of the initial PCE after over 2100 h in N_2 without encapsulation	188
TFE	ITO/PEDOT:PSS/(PEA,FA)SnI_3/PTAA/Au	p-i-n	0.85	20.50	76.43	13.32	Retain 85% of the initial PCE after 2880 h in N_2 with encapsulation	187

This journal is © The Royal Society of Chemistry 2025

Published on 01 August 2025. Downloaded on 1/24/2026 5:38:31 AM.

Table 3 (*Contd.*)

Strategy/CTL material	Device structure		V_{OC} (V)	J_{SC} (mA cm^{-2})	FF (%)	PCE (%)	Shelf stability	Ref.
AM	ITO/PEDOT:PSS/$FASnI_3$/C_{60}/BCP/Ag	p-i-n	0.45	23.75	57.50	6.22	—	181
CD	ITO/PEDOT:PSS/(PEA,FA)SnI_3/ICBA/BCP/Ag	p-i-n	1.017	19.67	74.68	14.94	Retain 100% of the initial PCE after 4000 h in N_2 without encapsulation	151
DCBA	ITO/PEDOT:PSS/$PEA_{0.15}FA_{0.85}SnI_3$/fullerene ETL/BCP/Ag	p-i-n	0.90	21.39	75.70	14.58	—	228
C_{60}BB	ITO/PEDOT:PSS/$PEA_{0.15}FA_{0.85}SnI_3$/fullerene/BCP/Ag	p-i-n	0.81	25.07	71.84	14.51	Retain 97% of the initial PCE after 3000 h in N_2 without encapsulation	202
PEG	ITO/HTL/$PEA_{0.1}FA_{0.9}SnI_3$/ICBA/Ag	p-i-n	0.71	24.42	58.30	10.10	Retain 70% of the initial PCE after 270 h in air without encapsulation	191
Cl-RCB	ITO/$FASnI_3$/PC_{61}BM/BCP/Ag	p-i-n	0.97	20.02	73.00	14.20	—	37
PDI and Fc	ITO/PEDOT:PSS/$FASnI_3$/BCP/Ag	p-i-n	0.77	23.97	74.37	13.65	—	43
PMMA in ICBA	ITO/PEDOT:PSS/$FASnI_3$/PMMA–ICBA/Ag	p-i-n	0.90	22.60	—	15.80	Retain 80% of the initial PCE after 60 in N_2 atmosphere without encapsulation	207

4. Challenges and outlook

The intensive research efforts surrounding hybrid organic–inorganic halide perovskites epitomize one of the most rapidly evolving domains in contemporary chemistry and materials science. Notably, the exceptional properties exhibited by Sn-based perovskite materials have galvanized the photovoltaic research community to channel substantial efforts, which could also be of great potential for upgrading their application and integration into various optoelectronic technologies.[3,4,16,229–240] While the PCE of TPSCs has surpassed 17%, it highly demands sustained innovation focused on bridging the gap between the current performance and the theoretical Shockley–Queisser limit (>33%), coupled with enhancing operational stability for practical commercialization. This section examines the present challenges and future prospects in the TPSC field through the lens of crystallization control, addressing Sn^{2+} instability and large-area film fabrication (Fig. 25).

4.1 Crystallization control: balancing kinetics and thermodynamics for defect-free films

Sn-based perovskites suffer from uncontrollable crystallization kinetics because of the rapid nucleation as well as growth driven by Sn^{2+}'s small ionic radius. This results in polycrystalline films with dense grain boundaries, Sn vacancies, and under-coordinated Sn^{2+} sites, which act as nonradiative recombination centers. While solvent engineering and additive strategies (*e.g.*, hypophosphorous acid) have improved the film quality, achieving millimeter-scale grains uniformly across large areas remains a challenge. To address this challenge, interdisciplinary approaches integrating material innovation, *in situ* diagnostics, and machine learning are imperative. First, multifunctional molecular additives such as Lewis base thiourea derivatives with dual passivation and crystallization-retardation capabilities can coordinate with Sn^{2+} to suppress the defects. Second, real-time monitoring using techniques such as Raman spectroscopy and grazing-incidence wide-angle X-ray scattering (GIWAXS) coupled with automated feedback systems allows for the dynamic adjustment of processing parameters (*e.g.*, anti-solvent drip rates and temperature gradients) to tailor nucleation pathways. Template-guided growth using 2D perovskite seed layers or mesoporous scaffolds (*e.g.*, TiO_2/Al_2O_3 hybrids) further constrains crystal orientation, significantly reducing the defect density of the grain boundary.

4.2 Addressing Sn^{2+} instability: oxidation pathways and degradation mechanisms

The commercialization of TPSCs is critically hindered by the inherent instability of Sn^{2+}, which undergoes rapid oxidation to Sn^{4+} (p-type self-doping) and Sn^0 (metallic clusters) under ambient conditions. Even trace moisture penetration generates deep mid-gap states (0.4–0.6 eV above valence band maximum), degrading the V_{OC} and FF during accelerated aging tests. Conventional stabilization approaches such as hydrophobic encapsulants (*e.g.*, PMMA) and reducing agents (*e.g.*, SnF_2)

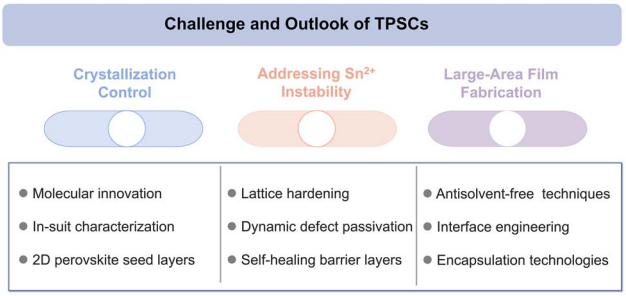

Fig. 25 Challenges and prospects of TPSCs in three domains: crystallization control, Sn^{2+} instability, and large-area film fabrication.

Published on 01 August 2025. Downloaded on 1/24/2026 5:38:31 AM.

provide only transient protection, failing to mitigate thermal- or UV-induced degradation. Oxidation-driven p-type doping further disrupts interfacial band alignment, increasing recombination losses at the electron/hole-transport layer interfaces. Achieving operational durability requires a multifaceted strategy integrating lattice hardening, dynamic defect passivation, and advanced encapsulation. Chemical hardening *via* B-site alloying can increase the Sn^{4+} formation energy, while mixed-halide compositions (*e.g.*, Cl/Br co-substitution) suppress oxidation by aligning the conduction band minimum with the Sn^{2+} redox potential. In addition, self-healing barrier layers, such as ascorbic acid-functionalized polymers, have been shown to reduce Sn^{4+} concentration. Future work must integrate these strategies with machine learning-guided additive screening and multiscale oxidation modeling to predict long-term degradation, targeting Sn-based perovskites with long-term operational lifetimes.

4.3 Large-area film fabrication: bridging the gap between lab-scale efficiency and industrial scalability

The future commercialization of TPSCs hinges critically on overcoming the formidable challenges associated with large-area film fabrication. Currently, scaling up from laboratory-scale high-efficiency devices to industrially relevant module sizes exacerbates inherent material vulnerabilities, particularly the rapid, uncontrolled crystallization kinetics of tin perovskites, which leads to non-uniform grain growth, elevated defect densities at grain boundaries, and detrimental Sn^{2+} oxidation. These issues manifest as severe PCE losses, pronounced spatial inhomogeneity, and compromised operational stability across substrates, directly conflicting with the stringent uniformity and durability requirements of photovoltaic modules. To address these bottlenecks, future strategies must prioritize advanced crystallization control methodologies, such as vacuum-assisted or antisolvent-free coating techniques combined with *in situ* spectroscopic monitoring, to regulate nucleation and growth dynamics. Concurrently, innovative interface engineering approaches utilizing multifunctional ligands, 2D/3D heterostructures, or atomic layer deposition passivation layers will be pivotal in mitigating interfacial recombination and stabilizing Sn^{2+} against oxidation. Furthermore, the development of scalable, solution-processable encapsulation technologies and roll-to-roll compatible manufacturing platforms, integrated with machine learning-driven process optimization, will be essential to bridge the efficiency-stability-cost trilemma.

5. Conclusion

In this review, we highlighted the transformative promise of TPSCs as sustainable, lead-free alternatives to perovskite-based photovoltaics. The fundamental properties of Sn-based perovskites and strategic advancements in terms of structural engineering, crystallization kinetics, and interfacial optimization aiming at enhancing TPSCs performance were systematically reviewed. Furthermore, we provided critical perspectives on the design methods of functional materials for achieving highly efficient and stable TPSCs that meet the stringent requirements for industrial-scale production. This review offered a comprehensive roadmap to accelerate the realization of high-performance Sn-based perovskite photovoltaics *via* advanced regulation strategies, and it is expected to inspire more efforts in the field of Sn-based optoelectronics beyond solar cells.

Conflicts of interest

There are no conflicts to declare.

Data availability

No primary research results, software or code have been included, and no new data were generated or analysed as part of this review.

Acknowledgements

This work was financially supported by the Natural Science Foundation of China (Grants 52372226, 52202300, and 62288102), the National Key R&D Program of China (2023YFB4204500), the Postdoctoral Fellowship Program of the China Postdoctoral Science Foundation (CPSF) (Grant GZC20233506), the China Postdoctoral Science Foundation (Grants 2022M722591 and 2024M764252), the Natural Science Basic Research Program of Shaanxi (Program No. 2025JC-YBQN-140), the Natural Science Foundation of Chongqing China (grant no. 2023NSCQ-MSX0097), the Guangdong Basic and Applied Basic Research Foundation (2024A1515010918), the Shenzhen Science and Technology Program (Grant JCYJ20240813150819026), and the Fundamental Research Funds for the Central Universities.

References

1 M. A. Green, E. D. Dunlop, M. Yoshita, N. Kopidakis, K. Bothe, G. Siefer, D. Hinken, M. Rauer, J. Hohl-Ebinger and X. Hao, *Prog. Photovoltaics Res. Appl.*, 2024, **32**, 425–441.
2 H. Dong, C. Ran, W. Gao, M. Li, Y. Xia and W. Huang, *eLight*, 2023, **3**, 3.
3 J. Yang, Z. Wang, X. Zhao, W. Gao, G. Xing, X. Wang, L. Wang, C. Li, Y. Wang, Y. Ren, W. Liu, F. Yang, J. Sun,

 This journal is © The Royal Society of Chemistry 2025

Published on 01 August 2025. Downloaded on 1/24/2026 5:38:31 AM.

H. Dong, L. Chao, Y. Zhou, Y. Chen, Z. Wu, C. Ran and W. Huang, *Energy Environ. Sci.*, 2025, **18**, 2883–2894.
4 G. Xing, C. Li, W. Gao, J. Yang, X. Zhao, J. Wang, X. Ran, L. Chao, H. Huang, Y. Zhou, Y. Chen, Z. Wu, C. Ran and W. Huang, *Adv. Mater.*, 2024, **36**, e2404185.
5 C. Li, C. Chen, W. Gao, H. Dong, Y. Zhou, Z. Wu and C. Ran, *ACS Nano*, 2024, **18**, 35130–35163.
6 M. Kundar, P. Kumar, S. K. Sharma, R. Singh and S. K. Pal, *Sol. RRL*, 2023, **7**, 2300572.
7 P. Kumar, S. K. Sharma and R. Singh, *EES Sol.*, 2025, **1**, 356–365.
8 B. Mondal, R. Tiwari, S. Manna, F. Banerjee, R. Singh and S. K. Samanta, *ACS Appl. Energy Mater.*, 2025, **8**, 3459–3469.
9 R. Singh, M. Parashar, S. Sandhu, K. Yoo and J.-J. Lee, *Sol. Energy*, 2021, **220**, 43–50.
10 M. Wang and Y. Shi, *Sci. China:Chem.*, 2024, **67**, 1117–1136.
11 H. Liu, Z. Zhang, W. Zuo, R. Roy, M. Li, M. M. Byranvand and M. Saliba, *Adv. Energy Mater.*, 2023, **13**, 2202209.
12 B. Park, B. Philippe, X. Zhang, H. Rensmo, G. Boschloo and E. M. J. Johansson, *Adv. Mater.*, 2015, **27**, 6806–6813.
13 T. Krishnamoorthy, H. Ding, C. Yan, W. L. Leong, T. Baikie, Z. Zhang, M. Sherburne, S. Li, M. Asta, N. Mathews and S. G. Mhaisalkar, *J. Mater. Chem. A*, 2015, **3**, 23829–23832.
14 X. Wei, S. Chen, G. Zheng, Q. Zhao, S. Mo, J. Wang, D. Yao, N. Tian and F. Long, *J. Mol. Struct.*, 2024, **1304**, 137634.
15 W.-Y. Gao, C.-X. Ran, L. Zhao, H. Dong, W.-Y. Li, Z.-Q. Gao, Y.-D. Xia, H. Huang and Y.-H. Chen, *Rare Met.*, 2024, **43**, 5720–5733.
16 W. Gao, R. Huang, H. Dong, W. Li, Z. Wu, Y. Chen and C. Ran, *Chem. Soc. Rev.*, 2025, **54**, 1384–1428.
17 J. Chen, J. Luo, Y. Li, X. Chen, Z. Song, E. Hou, C. Sun, H. Zhang, S. Cheng, Y. Xing, S. Chen, X. Zhao, L. Xie, C. Tian and Z. Wei, *Angew. Chem., Int. Ed.*, 2025, **64**, e202420150.
18 F. Hao, C. C. Stoumpos, D. H. Cao, R. P. H. Chang and M. G. Kanatzidis, *Nat. Photonics*, 2014, **8**, 489–494.
19 N. K. Noel, S. D. Stranks, A. Abate, C. Wehrenfennig, S. Guarnera, A.-A. Haghighirad, A. Sadhanala, G. E. Eperon, S. K. Pathak, M. B. Johnston, A. Petrozza, L. M. Herz and H. J. Snaith, *Energy Environ. Sci.*, 2014, **7**, 3061–3068.
20 W. Liao, D. Zhao, Y. Yu, C. R. Grice, C. Wang, A. J. Cimaroli, P. Schulz, W. Meng, K. Zhu, R. Xiong and Y. Yan, *Adv. Mater.*, 2016, **28**, 9333–9340.
21 Z. Zhang, Y. Huang, J. Jin, Y. Jiang, Y. Xu, J. Zhu and D. Zhao, *Angew Chem. Int. Ed. Engl.*, 2023, **62**, e202308093.
22 Z. Xiao, Z. Song and Y. Yan, *Adv. Mater.*, 2019, **31**, 1803792.
23 N. Arora, M. I. Dar, A. Hinderhofer, N. Pellet, F. Schreiber, S. M. Zakeeruddin and M. Grätzel, *Science*, 2017, **358**, 768–771.
24 H. Dong, C. Ran, W. Gao, N. Sun, X. Liu, Y. Xia, Y. Chen and W. Huang, *Adv. Energy Mater.*, 2022, **12**, 2102213.
25 S. J. Lee, S. S. Shin, Y. C. Kim, D. Kim, T. K. Ahn, J. H. Noh, J. Seo and S. I. Seok, *J. Am. Chem. Soc.*, 2016, **138**, 3974–3977.
26 F. Hao, C. C. Stoumpos, P. Guo, N. Zhou, T. J. Marks, R. P. H. Chang and M. G. Kanatzidis, *J. Am. Chem. Soc.*, 2015, **137**, 11445–11452.
27 X. Liu, K. Yan, D. Tan, X. Liang, H. Zhang and W. Huang, *ACS Energy Lett.*, 2018, **3**, 2701–2707.
28 T. Fujihara, S. Terakawa, T. Matsushima, C. Qin, M. Yahiro and C. Adachi, *J. Mater. Chem. C*, 2017, **5**, 1121–1127.
29 J. Qiu, Y. Xia, Y. Zheng, W. Hui, H. Gu, W. Yuan, H. Yu, L. Chao, T. Niu, Y. Yang, X. Gao, Y. Chen and W. Huang, *ACS Energy Lett.*, 2019, **4**, 1513–1520.
30 P. Li, X. Liu, Y. Zhang, C. Liang, G. Chen, F. Li, M. Su, G. Xing, X. Tao and Y. Song, *Angew. Chem., Int. Ed.*, 2020, **59**, 6909–6914.
31 S. Shao, J. Dong, H. Duim, G. H. Ten Brink, G. R. Blake, G. Portale and M. A. Loi, *Nano Energy*, 2019, **60**, 810–816.
32 C. Wang, Y. Zhang, F. Gu, Z. Zhao, H. Li, H. Jiang, Z. Bian and Z. Liu, *Matter*, 2021, **4**, 709–721.
33 X. Meng, Y. Li, Y. Qu, H. Chen, N. Jiang, M. Li, D. Xue, J. Hu, H. Huang and S. Yang, *Angew. Chem., Int. Ed.*, 2021, **60**, 3693–3698.
34 S. Wang, L. Yan, W. Zhu, Z. Cao, L. Zhou, L. Ding and F. Hao, *Nano Energy*, 2022, **99**, 107416.
35 Z. Zhang, M. A. Kamarudin, A. K. Baranwal, G. Kapil, S. R. Sahamir, Y. Sanehira, M. Chen, L. Wang, Q. Shen and S. Hayase, *Angew. Chem., Int. Ed.*, 2022, **61**, e202210101.
36 W. Liu, S. Hu, J. Pascual, K. Nakano, R. Murdey, K. Tajima and A. Wakamiya, *ACS Appl. Mater. Interfaces*, 2023, **15**, 32487–32495.
37 Z. Zhang, Y. Huang, C. Wang, Y. Jiang, J. Jin, J. Xu, Z. Li, Z. Su, Q. Zhou, J. Zhu, R. He, D. Hou, H. Lai, S. Ren, C. Chen, X. Gao, T. Shi, W. Hu, F. Fu, P. Gao and D. Zhao, *Energy Environ. Sci.*, 2023, **16**, 3430–3440.
38 F. Zargar, D. Desta, S. Mertens, M. Van Landeghem, S. Hamtaei, J. Prooth, J. Zillner, J. Hajhemati, M. Safari, A. Hardy, P. Schulz, E. Ahlswede, B. Vermang, K. Vandewal and H.-G. Boyen, *ACS Appl. Energy Mater.*, 2024, **7**, 3618–3626.
39 J. Wang, J. Huang, M. Abdel-Shakour, T. Liu, X. Wang, Y. Pan, L. Wang, E. Cui, J. Hu, S. Yang and X. Meng, *Angew. Chem., Int. Ed.*, 2024, **63**, e202317794.
40 D. He, P. Chen, J. A. Steele, Z. Wang, H. Xu, M. Zhang, S. Ding, C. Zhang, T. Lin, F. Kremer, H. Xu, M. Hao and L. Wang, *Nat. Nanotechnol.*, 2025, **20**, 779–786.
41 D. Sabba, H. K. Mulmudi, R. R. Prabhakar, T. Krishnamoorthy, T. Baikie, P. P. Boix, S. Mhaisalkar and N. Mathews, *J. Phys. Chem. C*, 2015, **119**, 1763–1767.
42 H. Zhu, J. Ma, P. Li, S. Zang, Y. Zhang and Y. Song, *Chem*, 2022, **8**, 2939–2960.
43 F. Yang, K. Wang, Y. Yang, Y. Chen, Z. Kang, T. Li, R. Sun, Y. Tong and H. Wang, *Nano Lett.*, 2025, **25**, 5957–5964.
44 J. Cao and F. Yan, *Energy Environ. Sci.*, 2021, **14**, 1286–1325.
45 C. Luo, G. Zheng, F. Gao, X. Wang, C. Zhan, X. Gao and Q. Zhao, *Nat. Photonics*, 2023, **17**, 856–864.
46 E. A. R. Assirey, *Saudi Pharm. J.*, 2019, **27**, 817–829.
47 Z. Hasan, M. A. Rahman, D. K. Das and H. K. Rouf, *Sci. Rep.*, 2023, **13**, 10487.
48 S. Kahmann, O. Nazarenko, S. Shao, O. Hordiichuk, M. Kepenekian, J. Even, M. V. Kovalenko, G. R. Blake and M. A. Loi, *ACS Energy Lett.*, 2020, **5**, 2512–2519.

Published on 01 August 2025. Downloaded on 1/24/2026 5:38:31 AM.

49 T. Nakamura, T. Handa, R. Murdey, Y. Kanemitsu and A. Wakamiya, *ACS Appl. Electron. Mater.*, 2020, **2**, 3794–3804.
50 X. Jiang, Z. Zang, Y. Zhou, H. Li, Q. Wei and Z. Ning, *Acc. Mater. Res.*, 2021, **2**, 210–219.
51 T. Shi, H.-S. Zhang, W. Meng, Q. Teng, M. Liu, X. Yang, Y. Yan, H.-L. Yip and Y.-J. Zhao, *J. Mater. Chem. A*, 2017, **5**, 15124–15129.
52 R. Prasanna, A. Gold-Parker, T. Leijtens, B. Conings, A. Babayigit, H.-G. Boyen, M. F. Toney and M. D. McGehee, *J. Am. Chem. Soc.*, 2017, **139**, 11117–11124.
53 K. M. Anoop, D. Deepak, M. S. Sunitha and T. N. Ahipa, *Phys. Status Solidi A*, 2025, **222**, 2400569.
54 M. I. Saidaminov, I. Spanopoulos, J. Abed, W. Ke, J. Wicks, M. G. Kanatzidis and E. H. Sargent, *ACS Energy Lett.*, 2020, **5**, 1153–1155.
55 Y. Su, J. Yang, G. Liu, W. Sheng, J. Zhang, Y. Zhong, L. Tan and Y. Chen, *Adv. Funct. Mater.*, 2022, **32**, 2109631.
56 L. Lanzetta, T. Webb, N. Zibouche, X. Liang, D. Ding, G. Min, R. J. E. Westbrook, B. Gaggio, T. J. Macdonald, M. S. Islam and S. A. Haque, *Nat. Commun.*, 2021, **12**, 2853.
57 P. Xu, S. Chen, H.-J. Xiang, X.-G. Gong and S.-H. Wei, *Chem. Mater.*, 2014, **26**, 6068–6072.
58 D. Ricciarelli, D. Meggiolaro, F. Ambrosio and F. De Angelis, *ACS Energy Lett.*, 2020, **5**, 2787–2795.
59 Z. Zhang, X. Tian, C. Wang, J. Jin, Y. Jiang, Q. Zhou, J. Zhu, J. Xu, R. He, Y. Huang, S. Ren, C. Chen, P. Gao, R. Long and D. Zhao, *Energy Environ. Sci.*, 2022, **15**, 5274–5283.
60 Y. Zhang, J. Zhou, X. Ma, J. Dong, J. Wang, D. Han, Z. Zang, M.-G. Ju, Q. Zhang and N. Wang, *Sol. RRL*, 2023, **7**, 2200997.
61 E. W.-G. Diau, E. Jokar and M. Rameez, *ACS Energy Lett.*, 2019, **4**, 1930–1937.
62 N. Sun, W. Gao, H. Dong, Y. Liu, X. Liu, Z. Wu, L. Song, C. Ran and Y. Chen, *ACS Energy Lett.*, 2021, **6**, 2863–2875.
63 J. Liu, H. Yao, S. Wang, C. Wu, L. Ding and F. Hao, *Adv. Energy Mater.*, 2023, **13**, 2300696.
64 A. Soultati, M. Tountas, K. K. Armadorou, A. R. B. M. Yusoff, M. Vasilopoulou and M. K. Nazeeruddin, *Energy Adv.*, 2023, **2**, 1075–1115.
65 H. Li, M. Liu, M. Li, H. Park, N. Mathews, Y. Qi, X. Zhang, H. J. Bolink, K. Leo, M. Graetzel and C. Yi, *iEnergy*, 2022, **1**, 434–452.
66 Y. Jiang, Z. Zhang, Y. Wang, J. Jin, Y. Huang, W. Wang, D. Ma, H. Huang, C. Chen, S. Ren, S. Tsang, H. Yip and D. Zhao, *Adv. Funct. Mater.*, 2025, 2504541.
67 P. F. Chan, M. Qin, C. Su, L. Ye, X. Wang, Y. Wang, X. Guan, Z. Lu, G. Li, T. Ngai, S. W. Tsang, N. Zhao and X. Lu, *Adv. Sci.*, 2024, **11**, 2309668.
68 Y. Shih, A. Velusamy, C. Kuan, P. Huang, C. Kuo, D. Zeng, C. Liu, S. Hong, X. Jiang, M. Chen and E. W. Diau, *Small*, 2025, **21**, 2500642.
69 C.-H. Kuan, G.-S. Luo, S. Narra, S. Maity, H. Hiramatsu, Y.-W. Tsai, J.-M. Lin, C.-H. Hou, J.-J. Shyue and E. Wei-Guang Diau, *Chem. Eng. J.*, 2022, **450**, 138037.
70 Y. Yu, D. Zhao, C. R. Grice, W. Meng, C. Wang, W. Liao, A. J. Cimaroli, H. Zhang, K. Zhu and Y. Yan, *RSC Adv.*, 2016, **6**, 90248–90254.
71 D. Moghe, L. Wang, C. J. Traverse, A. Redoute, M. Sponseller, P. R. Brown, V. Bulović and R. R. Lunt, *Nano Energy*, 2016, **28**, 469–474.
72 P. Wang, F. Li, K. Jiang, Y. Zhang, H. Fan, Y. Zhang, Y. Miao, J. Huang, C. Gao, X. Zhou, F. Wang, L. Yang, C. Zhan and Y. Song, *Adv. Sci.*, 2020, **7**, 1903047.
73 T. Yokoyama, D. H. Cao, C. C. Stoumpos, T.-B. Song, Y. Sato, S. Aramaki and M. G. Kanatzidis, *J. Phys. Chem. Lett.*, 2016, **7**, 776–782.
74 P. Zhu, C. Chen, S. Gu, R. Lin and J. Zhu, *Sol. RRL*, 2018, **2**, 1700224.
75 X. Chen, J. Cheng, L. He, L. Zhao, C. Zhang, A. Pang and J. Li, *Molecules*, 2023, **28**, 3787.
76 D. Song, S. Ramakrishnan, Y. Zhang and Q. Yu, *ACS Energy Lett.*, 2024, **9**, 1466–1472.
77 L. Wang, M. Chen, S. Yang, N. Uezono, Q. Miao, G. Kapil, A. K. Baranwal, Y. Sanehira, D. Wang, D. Liu, T. Ma, K. Ozawa, T. Sakurai, Z. Zhang, Q. Shen and S. Hayase, *ACS Energy Lett.*, 2022, **7**, 3703–3708.
78 W. Gao, C. Chen, C. Ran, H. Zheng, H. Dong, Y. Xia, Y. Chen and W. Huang, *Adv. Funct. Mater.*, 2020, **30**, 2000794.
79 W. Gao, C. Ran, J. Li, H. Dong, B. Jiao, L. Zhang, X. Lan, X. Hou and Z. Wu, *J. Phys. Chem. Lett.*, 2018, **9**, 6999–7006.
80 C. Ferrara, M. Patrini, A. Pisanu, P. Quadrelli, C. Milanese, C. Tealdi and L. Malavasi, *J. Mater. Chem. A*, 2017, **5**, 9391–9395.
81 F. Li, Y. Xie, Y. Hu, M. Long, Y. Zhang, J. Xu, M. Qin, X. Lu and M. Liu, *ACS Energy Lett.*, 2020, **5**, 1422–1429.
82 E. Jokar, C. Chien, C. Tsai, A. Fathi and E. W. Diau, *Adv. Mater.*, 2019, **31**, 1804835.
83 W. Ke, C. C. Stoumpos, M. Zhu, L. Mao, I. Spanopoulos, J. Liu, O. Y. Kontsevoi, M. Chen, D. Sarma, Y. Zhang, M. R. Wasielewski and M. G. Kanatzidis, *Sci. Adv.*, 2017, **3**, e1701293.
84 D. Yang, J. Lv, X. Zhao, Q. Xu, Y. Fu, Y. Zhan, A. Zunger and L. Zhang, *Chem. Mater.*, 2017, **29**, 524–538.
85 S. Shao, J. Liu, G. Portale, H. Fang, G. R. Blake, G. H. Ten Brink, L. J. A. Koster and M. A. Loi, *Adv. Energy Mater.*, 2018, **8**, 1702019.
86 W. Ke, C. C. Stoumpos, I. Spanopoulos, L. Mao, M. Chen, M. R. Wasielewski and M. G. Kanatzidis, *J. Am. Chem. Soc.*, 2017, **139**, 14800–14806.
87 D. H. Cao, C. C. Stoumpos, T. Yokoyama, J. L. Logsdon, T.-B. Song, O. K. Farha, M. R. Wasielewski, J. T. Hupp and M. G. Kanatzidis, *ACS Energy Lett.*, 2017, **2**, 982–990.
88 E. Jokar, C.-H. Chien, A. Fathi, M. Rameez, Y.-H. Chang and E. W.-G. Diau, *Energy Environ. Sci.*, 2018, **11**, 2353–2362.
89 F. Du, H. Gu, W. Jiang, W. Yang, Y. Lin, W. Zhu, X. Qin, X. Xie, L. Bu, X. Liu, S. Yang and C. Liang, *Adv. Funct. Mater.*, 2025, **35**, 2413281.
90 S.-H. Chin and J.-W. Lee, *Nano Res. Energy*, 2023, **2**, e9120071.
91 M.-G. Ju, J. Dai, L. Ma and X. C. Zeng, *J. Am. Chem. Soc.*, 2017, **139**, 8038–8043.
92 S. Nagane, D. Ghosh, R. L. Z. Hoye, B. Zhao, S. Ahmad, A. B. Walker, M. S. Islam, S. Ogale and A. Sadhanala, *J. Phys. Chem. C*, 2018, **122**, 5940–5947.

 This journal is © The Royal Society of Chemistry 2025

Published on 01 August 2025. Downloaded on 1/24/2026 5:38:31 AM.

93 M. Liu, H. Pasanen, H. Ali-Löytty, A. Hiltunen, K. Lahtonen, S. Qudsia, J. Smått, M. Valden, N. V. Tkachenko and P. Vivo, *Angew. Chem., Int. Ed.*, 2020, **59**, 22117–22125.
94 R. Ali, G.-J. Hou, Z.-G. Zhu, Q.-B. Yan, Q.-R. Zheng and G. Su, *J. Mater. Chem. A*, 2018, **6**, 9220–9227.
95 H. Hasegawa, K. Kobayashi, Y. Takahashi, J. Harada and T. Inabe, *J. Mater. Chem. C*, 2017, **5**, 4048–4052.
96 S. Adjokatse, S. Kahmann, H. Duim and M. A. Loi, *APL Mater.*, 2019, **7**, 031116.
97 Z. Wu, Q. Zhang, B. Li, Z. Shi, K. Xu, Y. Chen, Z. Ning and Q. Mi, *Chem. Mater.*, 2019, **31**, 4999–5004.
98 Q. Li, Y. Zhao, W. Zhou, Z. Han, R. Fu, F. Lin, D. Yu and Q. Zhao, *Adv. Energy Mater.*, 2019, **9**, 1902239.
99 J. Wang, H. Shen, W. Li, S. Wang, J. Li and D. Li, *Adv. Sci.*, 2019, **6**, 1802019.
100 C. Tsai, N. Mohanta, C. Wang, Y. Lin, Y. Yang, C. Wang, C. Hung and E. W. Diau, *Angew. Chem., Int. Ed.*, 2017, **56**, 13819–13823.
101 B. Yu, M. Liao, Y. Zhu, X. Zhang, Z. Du, Z. Jin, D. Liu, Y. Wang, T. Gatti, O. Ageev and Z. He, *Adv. Funct. Mater.*, 2020, **30**, 2002230.
102 L. Gu, M. Chen, X. Liu, D. Chen, Y. Gu and S. Wang, *Sol. RRL*, 2024, **8**, 2301001.
103 J. Jin, Z. Zhang, S. Zou, F. Cao, Y. Huang, Y. Jiang, Z. Gao, Y. Xu, J. Qu, X. Wang, C. Chen, C. Xiao, S. Ren and D. Zhao, *Adv. Energy Mater.*, 2025, **15**, 2403718.
104 Y.-E. Lye, K.-Y. Chan and Z.-N. Ng, *Nanomaterials*, 2023, **13**, 585.
105 Z.-Q. Ma, H. Pan and P. K. Wong, *J. Electron. Mater.*, 2016, **45**, 5956–5966.
106 W. Ke, C. C. Stoumpos, I. Spanopoulos, M. Chen, M. R. Wasielewski and M. G. Kanatzidis, *ACS Energy Lett.*, 2018, **3**, 1470–1476.
107 J. Tian, J. Wu, R. Li, Y. Lin, J. Geng, W. Lin, Y. Wang, Q. Ouyang, Z. Wu, W. Sun, L. Li, Z. Lan and Y. Lin, *Nano Energy*, 2023, **118**, 108939.
108 G. Grancini, C. Roldán-Carmona, I. Zimmermann, E. Mosconi, X. Lee, D. Martineau, S. Narbey, F. Oswald, F. De Angelis, M. Graetzel and M. K. Nazeeruddin, *Nat. Commun.*, 2017, **8**, 15684.
109 H. Xu, Y. Jiang, T. He, S. Li, H. Wang, Y. Chen, M. Yuan and J. Chen, *Adv. Funct. Mater.*, 2019, **29**, 1807696.
110 M. Chen, M.-G. Ju, M. Hu, Z. Dai, Y. Hu, Y. Rong, H. Han, X. C. Zeng, Y. Zhou and N. P. Padture, *ACS Energy Lett.*, 2019, **4**, 276–277.
111 M.-G. Ju, J. Dai, L. Ma, Y. Zhou, W. Liang and X. C. Zeng, *J. Mater. Chem. A*, 2019, **7**, 16742–16747.
112 Y. Liao, H. Liu, W. Zhou, D. Yang, Y. Shang, Z. Shi, B. Li, X. Jiang, L. Zhang, L. N. Quan, R. Quintero-Bermudez, B. R. Sutherland, Q. Mi, E. H. Sargent and Z. Ning, *J. Am. Chem. Soc.*, 2017, **139**, 6693–6699.
113 S. Sandhu, R. Singh, K. Yoo, M. Kumar and J.-J. Lee, *J. Power Sources*, 2021, **491**, 229574.
114 C. Ran, J. Xi, W. Gao, F. Yuan, T. Lei, B. Jiao, X. Hou and Z. Wu, *ACS Energy Lett.*, 2018, **3**, 713–721.
115 Z. Kang, P. Feng, K. Wang, L. Zhang, R. Meng, Y. Chen, J. Wu, F. Yang, X. Zhang, T. Li, J. Shang, Y. Tong and H. Wang, *Energy Environ. Sci.*, 2025, **18**, 4108–4119.
116 G. Feng, H. Loi, T. Wang, W. Deng, Z. Guan, Q. Wei, J. He, M. Li, C. Lee, J. Wang, Q. Zhang and F. Yan, *Angew. Chem., Int. Ed.*, 2025, **64**, e202413584.
117 Y. Chen, K. Wang, W. Chen, T. Li, H. Tu, F. Yang, Z. Kang, Y. Tong and H. Wang, *Adv. Energy Mater.*, 2025, **15**, 2406024.
118 Z. Zhao, F. Gu, Y. Li, W. Sun, S. Ye, H. Rao, Z. Liu, Z. Bian and C. Huang, *Adv. Sci.*, 2017, **4**, 1700204.
119 S. Tsarev, A. G. Boldyreva, S. Yu. Luchkin, M. Elshobaki, M. I. Afanasov, K. J. Stevenson and P. A. Troshin, *J. Mater. Chem. A*, 2018, **6**, 21389–21395.
120 K. Chen, P. Wu, W. Yang, R. Su, D. Luo, X. Yang, Y. Tu, R. Zhu and Q. Gong, *Nano Energy*, 2018, **49**, 411–418.
121 C. Ran, W. Gao, J. Li, J. Xi, L. Li, J. Dai, Y. Yang, X. Gao, H. Dong, B. Jiao, I. Spanopoulos, C. D. Malliakas, X. Hou, M. G. Kanatzidis and Z. Wu, *Joule*, 2019, **3**, 3072–3087.
122 P. Cheng, T. Wu, J. Liu, W.-Q. Deng and K. Han, *J. Phys. Chem. Lett.*, 2018, **9**, 2518–2522.
123 N. Ito, M. A. Kamarudin, D. Hirotani, Y. Zhang, Q. Shen, Y. Ogomi, S. Iikubo, T. Minemoto, K. Yoshino and S. Hayase, *J. Phys. Chem. Lett.*, 2018, **9**, 1682–1688.
124 K. Kobayashi, H. Hasegawa, Y. Takahashi, J. Harada and T. Inabe, *Mater. Chem. Front.*, 2018, **2**, 1291–1295.
125 M. Chen, M.-G. Ju, H. F. Garces, A. D. Carl, L. K. Ono, Z. Hawash, Y. Zhang, T. Shen, Y. Qi, R. L. Grimm, D. Pacifici, X. C. Zeng, Y. Zhou and N. P. Padture, *Nat. Commun.*, 2019, **10**, 16.
126 S. J. Lee, S. S. Shin, J. Im, T. K. Ahn, J. H. Noh, N. J. Jeon, S. I. Seok and J. Seo, *ACS Energy Lett.*, 2018, **3**, 46–53.
127 M. Rameez, S. Shahbazi, P. Raghunath, M. C. Lin, C. H. Hung and E. W.-G. Diau, *J. Phys. Chem. Lett.*, 2020, **11**, 2443–2448.
128 K. Nishimura, D. Hirotani, M. A. Kamarudin, Q. Shen, T. Toyoda, S. Iikubo, T. Minemoto, K. Yoshino and S. Hayase, *ACS Appl. Mater. Interfaces*, 2019, **11**, 31105–31110.
129 J. Qiu, Y. Xia, Y. Chen and W. Huang, *Adv. Sci.*, 2019, **6**, 1800793.
130 Z. Zhang, Y. Xu, S. Wang, C. Peng, P. Liu, S. Du, D. Pu, X. Zhao, M. Shang, G. Fang and Z. Yu, *Energy Environ. Sci.*, 2025, **18**, 3223–3234.
131 J. Liu, M. Ozaki, S. Yakumaru, T. Handa, R. Nishikubo, Y. Kanemitsu, A. Saeki, Y. Murata, R. Murdey and A. Wakamiya, *Angew. Chem., Int. Ed.*, 2018, **57**, 13221–13225.
132 Y. Su, J. Yang, H. Rao, Y. Zhong, W. Sheng, L. Tan and Y. Chen, *Energy Environ. Sci.*, 2023, **16**, 2177–2186.
133 Z. He, F. Wang, Y. Dong, Y. Zhang, R. Yu, F. Gao and Z. Tan, *Natl. Sci. Rev.*, 2025, **12**, nwaf097.
134 X. Meng, Y. Wang, J. Lin, X. Liu, X. He, J. Barbaud, T. Wu, T. Noda, X. Yang and L. Han, *Joule*, 2020, **4**, 902–912.
135 W. Li, W. Gao, R. Huang, H. Dong, Y. Zhou, Z. Wu, C. Ran and W. Huang, *Nano Lett.*, 2024, **24**, 16081–16089.

Published on 01 August 2025. Downloaded on 1/24/2026 5:38:31 AM.

136 N. Liu, M. Liu, J. Dai, X. Cheng and Z. Chen, *Angew Chem. Int. Ed. Engl.*, 2025, **64**, e202500947.
137 M. Xiao, S. Gu, P. Zhu, M. Tang, W. Zhu, R. Lin, C. Chen, W. Xu, T. Yu and J. Zhu, *Adv. Opt. Mater.*, 2018, **6**, 1700615.
138 X. Meng, J. Lin, X. Liu, X. He, Y. Wang, T. Noda, T. Wu, X. Yang and L. Han, *Adv. Mater.*, 2019, **31**, 1903721.
139 G. Li, Z. Su, M. Li, F. Yang, M. H. Aldamasy, J. Pascual, F. Yang, H. Liu, W. Zuo, D. Di Girolamo, Z. Iqbal, G. Nasti, A. Dallmann, X. Gao, Z. Wang, M. Saliba and A. Abate, *Adv. Energy Mater.*, 2021, **11**, 2101539.
140 H. Dong, R. Huang, W. Gao, W. Li, X. Ran, L. Chao, X. Wang, Y. Zhou, Z. Wu, Y. Chen and C. Ran, *Adv. Funct. Mater.*, 2025, **35**, 2420593.
141 S. Wang, A. Wang, X. Deng, L. Xie, A. Xiao, C. Li, Y. Xiang, T. Li, L. Ding and F. Hao, *J. Mater. Chem. A*, 2020, **8**, 12201–12225.
142 X. Jiang, Z. Zang, M. Ma, J. Wang, H. Wang and Z. Ning, *ACS Photonics*, 2023, **10**, 1992–1998.
143 R. Paul, F. Du, L. Dai, Y. Ding, Z. L. Wang, F. Wei and A. Roy, *Adv. Mater.*, 2019, **31**, 1805598.
144 C. Yuan, J. Wang, Y. Yang, X. Ma, Z. Zhao, M. Sun, H. Xu, Y. Pan, J. Hu, K. Mao, Y. Li, H. Ding, D. Luo, Y. Yang, J. Zhu, A. Abate, J. Xu, Z. Lu, X. Meng, A. K. Jen and Q. Hu, *Small*, 2025, **21**, 2408302.
145 Y. Chen, Y. Tong, F. Yang, T. Li, W. Li, H. Qi, Z. Kang, H. Wang and K. Wang, *Nano Lett.*, 2024, **24**, 5460–5466.
146 T. Wu, X. Liu, X. Luo, H. Segawa, G. Tong, Y. Zhang, L. K. Ono, Y. Qi and L. Han, *Nano-Micro Lett.*, 2022, **14**, 99.
147 F. Wang, X. Jiang, H. Chen, Y. Shang, H. Liu, J. Wei, W. Zhou, H. He, W. Liu and Z. Ning, *Joule*, 2018, **2**, 2732–2743.
148 Z. Zhu, X. Jiang, D. Yu, N. Yu, Z. Ning and Q. Mi, *ACS Energy Lett.*, 2022, **7**, 2079–2083.
149 J. Liu, S. Wang, W. Zhu, Z. Tang, L. Ding and F. Hao, *Chem. Eng. J.*, 2023, **453**, 139975.
150 J. Chen, J. Luo, E. Hou, P. Song, Y. Li, C. Sun, W. Feng, S. Cheng, H. Zhang, L. Xie, C. Tian and Z. Wei, *Nat. Photonics*, 2024, **18**, 464–470.
151 M. Zeng, Z. Yan, X. Ye, Y. Lou, T. Sheng, X. Jiang, Y. Mao, A. Huang, X. Yang, Z. Wang, Y. Sun, Y. Bai, H.-M. Cheng and G. Xing, *ACS Energy Lett.*, 2025, **10**, 1357–1365.
152 M. Abdel-Shakour, J. Wang, J. Huang, Z. Gao, Y. Pan and X. Meng, *Angew. Chem., Int. Ed.*, 2025, **64**, e202421547.
153 L. Ji, T. Zhang, Y. Wang, D. Liu, H. Chen, H. Zheng, X. Peng, S. Yuan, Z. D. Chen and S. Li, *Nanoscale*, 2022, **14**, 1219–1225.
154 O. E. Solis, M. Mínguez-Avellán, P. F. Betancur, R. I. Sánchez-Alarcón, I. Rodriguez, J. P. Martínez-Pastor, T. S. Ripolles, R. Abargues and P. P. Boix, *ACS Energy Lett.*, 2024, **9**, 5288–5295.
155 Q. Tai, X. Guo, G. Tang, P. You, T. Ng, D. Shen, J. Cao, C. Liu, N. Wang, Y. Zhu, C. Lee and F. Yan, *Angew. Chem., Int. Ed.*, 2019, **58**, 806–810.
156 H. Dong, C. Ran, W. Li, X. Liu, W. Gao, Y. Xia, Y. Chen and W. Huang, *Sci. China:Chem.*, 2022, **65**, 1895–1902.
157 J. Cao, Q. Tai, P. You, G. Tang, T. Wang, N. Wang and F. Yan, *J. Mater. Chem. A*, 2019, **7**, 26580–26585.
158 A. Balilonda, M. Du, Z. Li, W. Li, W. Mei, M. Y. Leung, G. Wu, X. Tao and W. Chen, *Adv. Funct. Mater.*, 2024, **34**, 2313833.
159 Y. Yang, F. Hu, T. Teng, C. Chen, J. Chen, N. Nizamani, K. Wang, Y. Xia, L. Huang and Z. Wang, *Angew. Chem., Int. Ed.*, 2025, **64**, e202415681.
160 X. Zhou, W. Peng, Z. Liu, Y. Zhang, L. Zhang, M. Zhang, C. Liu, L. Yan, X. Wang and B. Xu, *Energy Environ. Sci.*, 2024, **17**, 2837–2844.
161 E. Arunan, G. R. Desiraju, R. A. Klein, J. Sadlej, S. Scheiner, I. Alkorta, D. C. Clary, R. H. Crabtree, J. J. Dannenberg, P. Hobza, H. G. Kjaergaard, A. C. Legon, B. Mennucci and D. J. Nesbitt, *Pure Appl. Chem.*, 2011, **83**, 1637–1641.
162 Q. Fu, X. Tang, D. Li, L. Huang, S. Xiao, Y. Chen and T. Hu, *J. Mater. Chem. C*, 2020, **8**, 7786–7792.
163 B. Ma, J. Chen, M. Wang, X. Xu, J. Qian, Y. Lu, W. Zhang, P. Xia, M. Qin, W. Zhu, L. Zhang, S. Chen, X. Lu and W. Huang, *J. Phys. Chem. C*, 2020, **124**, 16289–16299.
164 P. Li, H. Dong, J. Xu, J. Chen, B. Jiao, X. Hou, J. Li and Z. Wu, *ACS Energy Lett.*, 2020, **5**, 2327–2334.
165 J. Chen, X. Zhao, Y. Cheng, J. Qian, M. Wang, W. Shen, K. Cao, Y. Huang, W. Hui, Y. Gu, Y. Chen, X. Gao and S. Chen, *Adv. Opt. Mater.*, 2021, **9**, 2100755.
166 Z. Lin, Y. Su, R. Dai, G. Liu, J. Yang, W. Sheng, Y. Zhong, L. Tan and Y. Chen, *ACS Appl. Mater. Interfaces*, 2021, **13**, 15420–15428.
167 H. Li, X. Jiang, Q. Wei, Z. Zang, M. Ma, F. Wang, W. Zhou and Z. Ning, *Angew. Chem., Int. Ed.*, 2021, **60**, 16330–16336.
168 C. Wang, F. Gu, Z. Zhao, H. Rao, Y. Qiu, Z. Cai, G. Zhan, X. Li, B. Sun, X. Yu, B. Zhao, Z. Liu, Z. Bian and C. Huang, *Adv. Mater.*, 2020, **32**, e1907623.
169 X. Meng, T. Wu, X. Liu, X. He, T. Noda, Y. Wang, H. Segawa and L. Han, *J. Phys. Chem. Lett.*, 2020, **11**, 2965–2971.
170 C. Zheng, P. Qiu, S. Zhong, X. Luo, S. Wu, Q. Wang, J. Gao, X. Lu, X. Gao, L. Shui, S. Wu and J.-M. Liu, *Adv. Funct. Mater.*, 2023, **33**, 2212106.
171 W. Ke, C. C. Stoumpos, J. L. Logsdon, M. R. Wasielewski, Y. Yan, G. Fang and M. G. Kanatzidis, *J. Am. Chem. Soc.*, 2016, **138**, 14998–15003.
172 Z. Yang, M. Zhong, Y. Liang, L. Yang, X. Liu, Q. Li, J. Zhang and D. Xu, *Adv. Funct. Mater.*, 2019, **29**, 1903621.
173 W. Ke, P. Priyanka, S. Vegiraju, C. C. Stoumpos, I. Spanopoulos, C. M. M. Soe, T. J. Marks, M.-C. Chen and M. G. Kanatzidis, *J. Am. Chem. Soc.*, 2018, **140**, 388–393.
174 S. Vegiraju, W. Ke, P. Priyanka, J. Ni, Y. Wu, I. Spanopoulos, S. L. Yau, T. J. Marks, M. Chen and M. G. Kanatzidis, *Adv. Funct. Mater.*, 2019, **29**, 1905393.
175 T. Yokoyama, Y. Nishitani, Y. Miyamoto, S. Kusumoto, R. Uchida, T. Matsui, K. Kawano, T. Sekiguchi and Y. Kaneko, *ACS Appl. Mater. Interfaces*, 2020, **12**, 27131–27139.
176 S. Liu, J. Li, W. Xiao, R. Chen, Z. Sun, Y. Zhang, X. Lei, S. Hu, M. Kober-Czerny, J. Wang, F. Ren, Q. Zhou, H. Raza, Y. Gao, Y. Ji, S. Li, H. Li, L. Qiu, W. Huang, Y. Zhao, B. Xu, Z. Liu, H. J. Snaith, N.-G. Park and W. Chen, *Nature*, 2024, **632**, 536–542.

 This journal is © The Royal Society of Chemistry 2025

Published on 01 August 2025. Downloaded on 1/24/2026 5:38:31 AM.

177 C. Chen, P. Zhu, X. Dong, Y. Dou, Y. Zhang, J. Liang, R. Mao, Y. Jiang, J. Wang, M. Wang, S. Chen and J. Zhu, *Chem. Eng. J.*, 2024, **489**, 151403.
178 N. Yan, Y. Cao, Z. Jin, Y. Liu, S. Liu, Z. Fang and J. Feng, *Adv. Mater.*, 2024, **36**, 2403682.
179 W. Gao, H. Dong, N. Sun, L. Chao, W. Hui, Q. Wei, H. Li, Y. Xia, X. Gao, G. Xing, Z. Wu, L. Song, P. Müller-Buschbaum, C. Ran and Y. Chen, *J. Energy Chem.*, 2022, **68**, 789–796.
180 B. Li, Z. Li, D. Gao, X. Wu, X. Li, C. Zhang, S. Li, J. Gong, D. Zhang, X. Xie, S. Xiao, H. Lu, M. Li and Z. Zhu, *Mater. Chem. Front.*, 2023, **7**, 3406–3413.
181 W. Zeng, Y. Shi, C. Yuan, E. Li, J. Li, Q. Niu, R. Xia, Y. Min and X. Peng, *Thin Solid Films*, 2024, **792**, 140264.
182 S. Y. Kim, S. J. Cho, S. E. Byeon, X. He and H. J. Yoon, *Adv. Energy Mater.*, 2020, **10**, 2002606.
183 S. Cho, P. Pandey, S. Yoon, J. Ryu, D.-G. Lee, Q. Shen, S. Hayase, H. Song, H. Choi, H. Ahn, C.-M. Oh, I.-W. Hwang, J. S. Cho and D.-W. Kang, *Surf. Interfaces*, 2023, **42**, 103478.
184 D. Song, S. Narra, M.-Y. Li, J.-S. Lin and E. W.-G. Diau, *ACS Energy Lett.*, 2021, **6**, 4179–4186.
185 S. N. Afraj, C. Kuan, J. Lin, J. Ni, A. Velusamy, M. Chen and E. W. Diau, *Adv. Funct. Mater.*, 2023, **33**, 2213939.
186 W. Gao, P. Li, J. Chen, C. Ran and Z. Wu, *Adv. Mater. Interfaces*, 2019, **6**, 1901322.
187 Z. Zhao, M. Sun, F. Xiang, X. Wu, Z. Fink, Z. Huang, J. Gao, H. Ding, P. Tan, C. Yuan, Y. Yang, N. A. Emelianov, L. A. Frolova, Z. Xiao, P. A. Troshin, T. P. Russell, J. Zhu, Y. Li and Q. Hu, *J. Mater. Chem. A*, 2025, **13**, 409–417.
188 X. Ren, S. Wang, H. Cai, P. Qiu, Q. Wang, X. Lu, X. Gao, L. Shui, S. Wu and J.-M. Liu, *Langmuir*, 2024, **40**, 19905–19916.
189 X. Liu, Y. Wang, F. Xie, X. Yang and L. Han, *ACS Energy Lett.*, 2018, **3**, 1116–1121.
190 C.-C. Shih and C.-G. Wu, *ACS Appl. Mater. Interfaces*, 2022, **14**, 16125–16135.
191 H. Na, S. Alam, G. Ham, D. Baek, T. O. Yoon, G. Lee, M. Q. Li, M. Lee, H. Cha, J. Lee and M. Kim, *ACS Energy Lett.*, 2024, **9**, 4306–4315.
192 L. Li, Y. Zhao, Q. Su, Q. Guo, J. Duan, J. Dou, L. Sun, Q. Zhang and Q. Tang, *Chem. Eng. J.*, 2025, **508**, 161132.
193 C. Chiang, H. Chen, W. Chen, W. Wang, S. Feng and C. Wu, *Adv. Energy Mater.*, 2024, **14**, 2400346.
194 T. Kitamura, L. Wang, Z. Zhang, A. K. Baranwal, G. Kapil, S. R. Sahamir, Y. Sanehira, H. Bi, T. Ma, Q. Shen and S. Hayase, *ACS Energy Lett.*, 2023, **8**, 3565–3568.
195 J. Zillner, H. Boyen, P. Schulz, J. Hanisch, N. Gauquelin, J. Verbeeck, J. Küffner, D. Desta, L. Eisele, E. Ahlswede and M. Powalla, *Adv. Funct. Mater.*, 2022, **32**, 2109649.
196 J.-J. Cao, Y.-H. Lou, W.-F. Yang, K.-L. Wang, Z.-H. Su, J. Chen, C.-H. Chen, C. Dong, X.-Y. Gao and Z.-K. Wang, *Chem. Eng. J.*, 2022, **433**, 133832.
197 T. Mahmoudi, M. Kohan, W. Rho, Y. Wang, Y. H. Im and Y. Hahn, *Adv. Energy Mater.*, 2022, **12**, 2201977.
198 F. He, T. Li, T. Shen, Y. Zhao, Z. Jin, Z. Zhang, Y. Pu, L. Deng, L. Qin, Y. Zhan, Y. Liu, Y. Wang and J. Liang, *Adv. Funct. Mater.*, 2024, **34**, 2405611.
199 Y. Shang, P. Wang, L. Jia, X. Li, W. Lian, P. Qian, M. Chen, T. Chen, Y. Lu and S. Yang, *Nano Res. Energy*, 2023, **2**, e9120073.
200 C. Sun, H. Zhang, S. Cheng, J. Chen, Y. Xing, Z. Nan, P. Yang, Y. Wang, X. Zhao, L. Xie, C. Tian and Z. Wei, *Adv. Mater.*, 2024, **36**, 2410248.
201 X. Jiang, F. Wang, Q. Wei, H. Li, Y. Shang, W. Zhou, C. Wang, P. Cheng, Q. Chen, L. Chen and Z. Ning, *Nat. Commun.*, 2020, **11**, 1245.
202 P. Yang, C. Sun, X. Fu, S. Cheng, J. Chen, H. Zhang, Z.-A. Nan, J. Yang, X.-J. Zhao, L.-Q. Xie, L. Meng, C. Tian and Z. Wei, *J. Am. Chem. Soc.*, 2024, **146**, 2494–2502.
203 F. H. Isikgor, S. Zhumagali, L. V. T. Merino, M. De Bastiani, I. McCulloch and S. De Wolf, *Nat. Rev. Mater.*, 2023, **8**, 89–108.
204 Y. Shi, Z. Zhu, D. Miao, Y. Ding and Q. Mi, *ACS Energy Lett.*, 2024, **9**, 1895–1897.
205 X. Cao, P. Li, X. Zhu, H. Li, R. Xu, J. Li, L. Ma, H. Dong and Z. Wu, *Sol. RRL*, 2023, **7**, 2300268.
206 M. Abdel-Shakour, T. H. Chowdhury, K. Matsuishi, Md. A. Karim, Y. He, Y. Moritomo and A. Islam, *ACS Appl. Energy Mater.*, 2021, **4**, 12515–12524.
207 Q. Ning, D. Miao, M. Ma, Z. Zhu, Y. Chen, Y. Ding, W. Li, W. Zhou, Y. Shi, Z. Ning and Q. Mi, *ACS Appl. Mater. Interfaces*, 2025, **17**, 32489–32496.
208 H. Li, B. Chang, L. Wang, Z. Wang, L. Pan, Y. Wu, Z. Liu and L. Yin, *ACS Energy Lett.*, 2022, **7**, 3889–3899.
209 F. Hu, C.-H. Chen, T.-Y. Teng, Y.-R. Shi, B. Wang, D. Xue, Y. Xia, J. Chen, K.-L. Wang, L.-Z. Huang, I. Yavuz, Z.-K. Wang and L.-S. Liao, *Adv. Energy Mater.*, 2024, **14**, 2302926.
210 Y. Miyamoto, S. Kusumoto, T. Yokoyama, Y. Nishitani, T. Matsui, T. Kouzaki, R. Nishikubo, A. Saeki and Y. Kaneko, *ACS Appl. Nano Mater.*, 2020, **3**, 11650–11657.
211 T. Li, B. Li, Y. Yang, Z. Jin, Z. Zhang, P. Wang, L. Deng, Y. Zhan, Q. Zhang and J. Liang, *Nat. Commun.*, 2024, **15**, 9435.
212 E. Widianto, M. Riswan, C. Driyo, N. Fauji, Kardiman, M. F. Hakim, N. M. Nursam and I. Santoso, *J. Electron. Mater.*, 2024, **53**, 7642–7654.
213 F. Gao, C. Li, L. Qin, L. Zhu, X. Huang, H. Liu, L. Liang, Y. Hou, Z. Lou, Y. Hu and F. Teng, *RSC Adv.*, 2018, **8**, 14025–14030.
214 M. A. Kamarudin, D. Hirotani, Z. Wang, K. Hamada, K. Nishimura, Q. Shen, T. Toyoda, S. Iikubo, T. Minemoto, K. Yoshino and S. Hayase, *J. Phys. Chem. Lett.*, 2019, **10**, 5277–5283.
215 M. Liao, B. Yu, Z. Jin, W. Chen, Y. Zhu, X. Zhang, W. Yao, T. Duan, I. Djerdj and Z. He, *ChemSusChem*, 2019, **12**, 5007–5014.
216 M. Lee, D. Kim, Y. K. Lee, H. Koo, K. T. Lee and I. Chung, *ACS Appl. Energy Mater.*, 2020, **3**, 5581–5588.
217 X. Liu, T. Wu, C. Zhang, Y. Zhang, H. Segawa and L. Han, *Adv. Funct. Mater.*, 2021, **31**, 2106560.

Published on 01 August 2025. Downloaded on 1/24/2026 5:38:31 AM.

218 D. B. Khadka, Y. Shirai, M. Yanagida and K. Miyano, *ACS Appl. Energy Mater.*, 2021, **4**, 12819–12826.
219 Y. Lin, J. Liu, J. Hu, C. Ran, Y. Chen, G. Xing, Y. Xia and Y. Chen, *ACS Appl. Mater. Interfaces*, 2021, **13**, 58809–58817.
220 M. Chen, G. Kapil, L. Wang, S. Razey Sahamir, A. K. Baranwal, K. Nishimura, Y. Sanehira, Z. Zhang, M. Akmal Kamarudin, Q. Shen and S. Hayase, *Chem. Eng. J.*, 2022, **436**, 135196.
221 T. Wang, H. Loi, J. Cao, Z. Qin, Z. Guan, Y. Xu, H. Cheng, M. G. Li, C. Lee, X. Lu and F. Yan, *Adv. Sci.*, 2022, **9**, 2200242.
222 C. Tian, C. Sun, J. Chen, P. Song, E. Hou, P. Xu, Y. Liang, P. Yang, J. Luo, L. Xie and Z. Wei, *Nanomaterials*, 2022, **12**, 532.
223 B. Chen, S. Wang, X. Zhang, W. Zhu, Z. Cao and F. Hao, *Chem. Eng. J.*, 2022, **445**, 136769.
224 D. Song, H. Li, Y. Xu and Q. Yu, *ACS Energy Lett.*, 2023, **8**, 3280–3287.
225 Y. Chen, H. Qi, K. Wang, Z. Kang, G. Pan, C. R. Everett, P. Müller-Buschbaum, Y. Tong and H. Wang, *Small Methods*, 2024, **8**, 2300029.
226 J. Chen, C. Wu, M. Wang, Y. Shen, J. Qian, W. Shen, K. Cao and S. Chen, *ACS Appl. Energy Mater.*, 2023, **6**, 9815–9823.
227 J. Ling, D. T. Cuzzupè, M. F. U. Din, A. Stepura, T. Burgard, Y. A. Temitmie, E. Majkova, M. Omastova, R. Jose, L. Schmidt-Mende and A. Fakharuddin, *ACS Appl. Energy Mater.*, 2024, **7**, 7152–7158.
228 C. Sun, P. Yang, Z. Nan, C. Tian, Y. Cai, J. Chen, F. Qi, H. Tian, L. Xie, L. Meng and Z. Wei, *Adv. Mater.*, 2023, **35**, 2205603.
229 J. H. Park, S. K. Hwang, S. G. Ji and J. Y. Kim, *Exploration*, 2023, **3**, 20220029.
230 W. Gao, X. Liu, H. Jin, W. Li, X. Wang, R. Huang, G. Xing, H. Dong, Y. Zhou, Z. Wu and C. Ran, *ACS Energy Lett.*, 2024, **9**, 5045–5055.
231 S.-H. Chin, *Journal of Optics and Photonics Research*, 2024, DOI: **10.47852/bonviewjopr42022936**.
232 S. Farhan, M. Q. Shah, M. N. Khan, M. Arif and A. Ghafoor, *Journal of Optics and Photonics Research*, 2024, **1**, 190–201.
233 G. Kim, K. Kim, H. J. Kim, H. S. Jung, I. Jeon and J. Lee, *EcoMat*, 2023, **5**, e12319.
234 J. Lee, T. Son, K. Min, S. Park, Y. Kim and J. Seo, *EcoMat*, 2023, **5**, e12414.
235 R. Li, X. Liu and J. Chen, *Exploration*, 2023, **3**, 20220027.
236 X. Lu, R. Lin, Y. Ding, M. Xia, W. Zheng and F. Huang, *InfoMat*, 2024, **6**(10), e12604.
237 R. K. Gunasekaran, J. Jung, S. W. Yang, J. Yun, Y. Yun, D. Vidyasagar, W. C. Choi, C.-L. Lee, J. H. Noh, D. H. Kim and S. Lee, *InfoMat*, 2023, **5**(4), e12393.
238 J. Qin, Z. Che, Y. Kang, C. Liu, D. Wu, H. Yang, X. Hu and Y. Zhan, *InfoMat*, 2024, **6**, e12522.
239 Y. Li, X. Guan, Y. Meng, J. Chen, J. Lin, X. Chen, C. Liu, Y. Zhao, Q. Zhang, C. Tian, J. Lu and Z. Wei, *InfoMat*, 2024, **6**(5), e12537.
240 P. Wu, J. H. Heo and F. Zhang, *Nano Res. Energy*, 2024, **3**, e9120093.

 This journal is © The Royal Society of Chemistry 2025